

Experimental Study: Investigating Effect of Injection on Yield Surface, Stress Path Coefficients,
and Associated Hysteresis in Unconsolidated Sands

By
Sabyasachi Prakash

A Dissertation submitted to the Department of Petroleum Engineering,

Cullen College of Engineering

in partial fulfillment of the requirements for the degree of

Doctor of Philosophy

In Petroleum Engineering

Chair of Committee: Dr. George K. Wong

Co-Chair of Committee: Dr. Michael T. Myers

Committee Member: Dr. Lori A. Hathon

Committee Member: Dr. Mohamed Y. Soliman

Committee Member: Dr. Duane Mikulencak

University of Houston

May 2021

©Copyright 2021, Sabyasachi Prakash

DEDICATION

This dissertation is dedicated to my father Gopal Chandra Sahoo, mother Dr. Pusalata Sahoo, brother Divya Jyoti Prakash and sister-in-law Nandita Sahoo, and my wife Ankita Sahu.

ACKNOWLEDGEMENTS

I would like to thank my advisor Dr. George K. Wong and my co-advisor Dr. Michael T. Myers for their relentless efforts to guide me through the dissertation. I would like to acknowledge Shell Oil Company for their financial support of this research work. I would like to thank my colleagues for their support in performing experiments.

ABSTRACT

Injection geomechanics is an integral part of sub-surface work. Material behavior is stress magnitude and stress path dependent. Many researchers have studied effects of depletion on rock mechanical behavior and corresponding changes in in-situ stresses. Most literature regarding study of injection effects in unconsolidated sands is primarily focused on Canadian Oil sands where the effective stress magnitudes are different than in deep-water Gulf of Mexico.

This thesis investigates the effects of depletion and injection on changing the minimum in-situ stress magnitude, yield behavior, and associated hysteresis in unconsolidated sands. A novel sample preparation technique is presented to make consistent and representative samples of the target reservoir in deep-water. The variation of minimum in-situ stresses with pore pressure is quantified using horizontal stress path coefficients. Far field reservoir boundary conditions are simulated through uniaxial strain boundary condition and with constant vertical stress. Results show material is altered during initial depletion and is associated with large plastic strains and hysteresis energy. Under repeat injection and depletion, material is elastic with minimal hysteresis energy.

Yield behavior of geo-materials under unloading stress path direction (injection) has not been studied in unconsolidated sands with high effective stresses. This thesis focuses on understanding the dependence of yield surfaces on stress path directions and stress magnitudes. Three different stress path directions were studied to determine individual yield surfaces. Results show yield surfaces for loading and unloading paths were different and parallel within the range of stress magnitudes studied. A global minimum yield surface model is proposed to predict the location of the minimum yield surface and its stress path. Using this model, the upper and lower bounds of yield surfaces can be determined with two tests. A yield function is generated to predict yield stresses with an initial stress condition and a stress path direction.

Table of Contents

DEDICATION.....	iii
ACKNOWLEDGEMENTS.....	iv
ABSTRACT.....	v
LIST OF TABLES.....	viii
LIST OF FIGURES.....	ix
1. INTRODUCTION.....	1
1.1 In-Situ Stress Estimation	1
1.2 Rock Mechanical Behavior Prediction	6
2. SAMPLE MATERIALS, PREPARATION AND EQUIPMENT	11
2.1 Analogue Material	11
2.2 Sand Pack Samples.....	14
2.2.1 Review of Sand Pack Preparation Techniques.....	14
2.2.2 Sample Preparation Procedure.....	15
2.3 Experimental Setup.....	16
2.3.1 Axial, Confining and Pore Pressure Setup.....	16
2.3.2 Strain Gauges and Calibration.....	17
2.4 Representative Analogue.....	21
3. STRESS PATH COEFFICIENTS.....	27
3.1 Test Procedure.....	29
3.2 Data Analysis and Results	33
3.2.1 Test 1 – Depletion Followed by Injection.....	34
3.2.2 Test 2 – Injection Followed by Depletion.....	39
3.2.3 Test 3 – Increasing Amplitude Depletion – Injection Cycles.....	45
3.3 Modelling and Discussions.....	53
3.4 Conclusions	59
4. YIELD SURFACE AND STRESS PATH DIRECTIONS.....	61
4.1 Test Procedure.....	64
4.1.1 Loading-Based Yield Behavior.....	64
4.1.2 Unloading-Based Yield Behavior	67
4.2 Data Analysis.....	77
4.2.1 Loading-Based Yield Behavior.....	77
4.2.2 Unloading Based Tests.....	82

4.3	Discussions and Results	89
4.4	Conclusions and Future Work.....	96
5.	COMBINED CONCLUSIONS AND FUTURE WORK	98
	REFERENCES.....	100
6.	APPENDIX 1 – MODIFIED CAM CLAY (MCC) MODEL.....	115
7.	APPENDIX II – MCC MODEL FITS	121

LIST OF TABLES

Table 3-1 Shows the initial conditions at the start of the pore pressure uniaxial strain tests for three samples under study. All samples start with similar values of mean effective stress and shear stress. The mean stress p' is defined in Equation 3.6, and shear stress q is axial stress minus confining stress.	29
Table 3-2 Horizontal stress path coefficients calculated from depletion and injection cycles for Test 1. The stress path coefficient for Depletion 1 ramp is smaller than subsequent load-unload ramps.	36
Table 3-3 Shows the amount of internal energy density change in each load-unload cycle for test 1 – PSP 213. The hysteresis energy dissipated in 1 st cycle is about six times larger than the 2 nd cycle.	39
Table 3-4 Horizontal stress path coefficients calculated from injection and depletion cycles for test 2 are presented. The stress path coefficient on last depletion ramp is markedly different than other ramps.	42
Table 3-5 Shows the amount of internal energy density change in each unload-load cycle for test 2 – PSP 214. Hysteresis energy is calculated as the difference of the change in internal energy density on load and unload cycle. No significant hysteresis is observed in both cycles.	44
Table 3-6 Shows the stress path coefficient values for the repeat stress path depletion and injection ramps as well as the new incremental stress path ramps. During new incremental depletion ramps the depletion coefficient is smaller whereas injection coefficient is similar.	50
Table 3-7 Show the calculation of hysteresis energy per unit pore pressure for PSP 215. The hysteresis energy is marginally increasing with each successive load-unload ramp.	53
Table 3-8 Shows the cam clay parameters used to fit the experimental data for the triaxial stress path and the uniaxial strain paths.	55
Table 4-1 A summary table of initial stress states for all constant axial stress unloading tests are shown.....	70
Table 4-2 Shows the initial stress states for samples where a constant shear stress test performed.	74
Table 4-3 shows the calculated yield stresses for different stress path angles, the expected yield stress based on triaxial yield surface and difference between the two yield points.	95
Table 7-1 shows the MCC Model parameter fits for PSP 214 on initial conditions, 1st injection, 1st depletion and last depletion ramps.....	121

LIST OF FIGURES

Figure 2-1 Shows the particle size distribution of the analogue material with a D50 of 229 microns and a U _c of 1.84.	12
Figure 2-2 Shows the particle size distribution of the sieved analogue material. The sieved material selected for this work has D50 of 203 microns and U _c of 1.44.	13
Figure 2-3 Shows a 2D thin section image of sieved analogue material in a grain mount under transmitted light. The material is predominantly quartz with very few heavy minerals present.	13
Figure 2-4 A schematic diagram of the sample setup in the stress cell. Average of the two measurements from LVDTs is used as axial strain. Average of the two measurements from cantilever bridge is used as radial strain.....	16
Figure 2-5 The calibrated values of the radial bridge using calibrated micrometers. Maximum measurement that can be made is 50 milli-inches (mils) and least count is 0.01 mils.	18
Figure 2-6 The calibrated values of both LVDTs using calibration micrometer. Maximum measurement that can be made is 400 mils. And least count is 0.02 mils.....	19
Figure 2-7 The stress-strain plot of stiffness test with Tungsten billet. The true Young's Modulus for Tungsten is 60 million psi. The calculated Young's Modulus is 58.9 million psi with an error of 1.8 %. The pressure corrections for the strain gauges are calibrated with Tungsten.	20
Figure 2-8 The stress-strain plot of stiffness test with Aluminum billet. The true Young's Modulus for Aluminum is 10 million psi. The calculated Young's Modulus is 10.94 million psi with an error of 9.4%. The pressure corrections for the strain gauges are verified with Aluminum.	20
Figure 2-9 Shows the pre-consolidation process to make representative analogue. The Confining stress is increased at 500 psi amplitude to reach peak confining stress during the initial load-unload ramps. The test is terminated when response is elastic.	24
Figure 2-10 shows a plot of percent recoverable axial strain at the end of each load-unload stage during consolidation experiment. The experiment is terminated when percent recoverable strain is consistently above 95%.	25
Figure 2-11 A plot of Axial Strain vs Mean Stress comparing hysteresis on the first maximum magnitude load-unload stage and the last maximum amplitude load-unload stage. Associated Hysteresis for first cycle is high compared to last cycle where the load and unload paths overlap each other.	25
Figure 3-1 Shows the Uniaxial strain boundary condition defined by Riazi et al., ASTM 2016. The axial stress is constant, pore pressure is the operating parameter and the confining pressure changes to keep the radial strain constant. The sample is deforming axially and with radial strain constant.	28

Figure 3-2 Shows the stress path followed to reach the initial stress conditions. First, the pore pressure is raised first followed by the confining stress, and the axial stress..... 30

Figure 3-3 Shows the stress path taken to reach initial test conditions in a mean effective stress – shear stress space. The pore pressure is ramped up first followed by confining stress and then axial stress to ensure maximum distance from the estimated yield surface. 30

Figure 3-4 Application of pore pressure, axial stress and radial stress as a function of time. The axial stress is constant under the uniaxial strain boundary conditions. Test 1 constitutes depletion followed by injection. Multiple load-unload ramps have been performed. 31

Figure 3-5 Application of pore pressure, axial stress and radial stress as a function of time. The axial stress is constant under the uniaxial strain boundary conditions. The sample is depleted to new pore pressure levels at last depletion. 32

Figure 3-6 Application of pore pressure, axial stress and radial stress as a function of time. Test 3 constitutes depletion followed by injection with varying amplitudes. At the last injection, the boundary stresses change from uniaxial strain to isostatic conditions. 33

Figure 3-7 Shows pore pressure depletion and injection ramps for PSP 213. Three pore pressure depletion and two pore pressure injection ramps have been performed in test 1. Test 1 constitutes depletion followed by injection. 34

Figure 3-8 shows the initial depletion and injection ramps in a confining stress – pore pressure plot. The slope of the curve represents the horizontal stress path coefficient. The calculated depletion coefficient and injection coefficient for test 1 are shown. 35

Figure 3-9 shows the plot of repeat depletion and injection ramps for test 1 - PSP 213. As can be seen, all ramps overlap each other with identical values of depletion and injection coefficients. 36

Figure 3-10 Shows volume strain behavior of the sample under changing mean effective stress during depletion and injection stress paths for test 1. The first load-unload ramp (1a-1c) has large amount of irrecoverable strains compared to subsequent ramps. 38

Figure 3-11 Shows the hysteresis in the first pore pressure depletion - injection cycle of PSP 213. Due to large amount of irrecoverable strain, the hysteresis energy dissipated during this cycle is high. 38

Figure 3-12 Shows the hysteresis in the second depletion - injection cycle of test 1 - PSP 213. Due to small amount of irrecoverable strain, the hysteresis energy dissipated during this cycle is low. 39

Figure 3-13 Shows pore pressure injection and depletion ramps for PSP 214. Three pore pressure depletion and two pore pressure injection ramps have been performed on PSP 214. Test 2

constitutes injection followed by depletion. The last depletion ramp takes sample to new depletion levels..... 40

Figure 3-14 shows a plot of calculated depletion coefficient and injection coefficient for test 2 – PSP 214. The two initial depletion and injection stages are shown. Both the ramps overlay each other and the stress path coefficient value during injection and depletion are the similar..... 41

Figure 3-15 shows the plot of repeat depletion and injection ramps for test 2 - PSP 214. For ramp 2, depletion ramp and injection ramp overlap each other. However, depletion to new pore pressure levels (2e - 2f) has a smaller depletion coefficient. 42

Figure 3-16 Shows the volume strain behavior of the sample under changing mean effective stress during depletion and injection stress paths for test 2. The last depletion ramp (2e - 2f) has larger amount of strain compared to other ramps..... 43

Figure 3-17 Shows the hysteresis in the 1st pore pressure injection - depletion cycle of test 2 – PSP 214. Both load-unload ramps overlay each other with minimal hysteresis energy in the 1st cycle. 43

Figure 3-18 Shows the hysteresis in the 2nd injection - depletion cycle of test 2 - PSP 214. Both load-unload ramps overlay each other with minimal hysteresis energy in the 2nd cycle..... 44

Figure 3-19 A comparison of change in mean effective stress vs change in volume strain plot of 1st depletion ramp of PSP 213 and last depletion ramp of PSP 214. Both ramps have similar amount of change in internal energy density which is evident from the overlapping stress- strain curves. 45

Figure 3-20 Application of pore pressure, axial stress and radial stress as a function of time. Test 3 constitutes depletion followed by injection with varying amplitudes to show impact of changing depletion and injection levels..... 46

Figure 3-21 shows a plot of calculated depletion coefficient and injection coefficient for test 3 – PSP 215. The initial depletion coefficient is small. The incremental injection stress path coefficient is same as the repeat injection coefficient. 47

Figure 3-22 A summary plot of repeat stress paths of depletion for PSP 215. The beginning and end of the ramps are labeled. All the repeat ramps have similar slopes with mean value of 0.73. 48

Figure 3-23 A summary plot of repeat stress paths of injection for PSP 215. The beginning and end of the ramps are labeled. All the repeat ramps have similar slopes with mean value of 0.73. 48

Figure 3-24 Shows a summary plot of new depletion stress paths for PSP 215. The beginning and end of each ramp are labeled. The depletion coefficient from new depletion stress paths is lower than repeat depletion stress paths..... 49

Figure 3-25 Shows a summary plot of new injection stress paths for PSP 215. The beginning and end of each ramp are labeled. The injection coefficient from new injection stress paths is similar to the repeat injection stress paths except for the injection 4 stress path..... 50

Figure 3-26 Shows a summary volume strain plot of PSP 215 under changing mean effective stress during depletion and injection stress paths. The beginning and end points of stress ramps are labeled. 51

Figure 3-27 Shows the load-unload cycle for calculation of hysteresis energy. The figures show a cumulative load-unload cycle consisting of both repeat depletion and new depletion ramps. ... 52

Figure 3-28 Shows the calibrated MCC model for triaxial stress path ramp of PSP 213. The yield surface is shown in blue; the critical state line is shown in green and the triaxial stress path is shown in red. 54

Figure 3-29 Shows the simulated strain data and experimental strain data plotted together. There is a good match between the two data sets indicating a good model fit..... 55

Figure 3-30 Shows the MCC model fits for the 1st Depletion (A), 1st Injection (B) and 2nd Depletion stress path. A simulated yield surface with its critical state line and the stress path taken by the sample and with experimental axial strain data recorded from the lab measurements are plotted. 57

Figure 3-31 Shows a schematic of the matrix and grains. During initial depletion, sample compacts in axial direction and irrecoverable strains occur with dissipation of energy. On initial injection, the sample response is elastic with no irrecoverable strain and associated dissipation of energy. 59

Figure 4-1 Shows the loading stress path and unloading stress paths used in this study. The loading stress paths are in $-90^\circ < \theta < 90^\circ$ and unloading stress paths are in $90^\circ \leq \theta \leq 270^\circ$ 62

Figure 4-2 Previous work on strength properties measurement on unconsolidated sands were done by researchers focused on the Alberta oil sands which have low effective stresses (< 250 psi). Current work focuses on higher stress magnitudes (> 2000 psi)..... 63

Figure 4-3 Shows the initial test conditions and load vs time plot single-stage triaxial test with a confining stress of 4350 psi. 65

Figure 4-4 Shows the stress path followed by the single stage triaxial test in a mean effective stress - shear stress plane with the initial stress point and the yield stress point. 65

Figure 4-5 Shows the application of confining stress and shear stress in the multi-stage triaxial test. 67

Figure 4-6 Shows the stress path followed by each stage in the multi-stage triaxial test in a mean effective stress - shear stress space..... 67

Figure 4-7 Shows the different stress paths for loading and unloading. During injection, mean effective stress increases with either decreasing or constant or increasing shear stress. The most representative stress path for actual reservoir conditions is the increasing shear stress path. ... 69

Figure 4-8 Shows the load vs time plot for PSP 212. This test is performed at the constant axial stress value of 9300 psi with an initial confining stress of 4350 psi. 71

Figure 4-9 Shows the load vs time plot for PSP 209. This test is performed at the constant axial stress value of 8400 psi with an initial confining stress of 4350 psi. 71

Figure 4-10 Shows the load vs time plot for PSP 210. This test is performed at the constant axial stress value of 7350 psi with an initial confining stress of 4350 psi. 72

Figure 4-11 Shows the load vs time plot for PSP 211. This test is performed at the constant axial stress value of 6360 psi with an initial confining stress of 4350 psi. 72

Figure 4-12 Shows a combined plot of stress path for constant axial stress tests. 73

Figure 4-13 Shows the load vs time plot for PSP 207. This test is performed at the constant shear stress value of 4950 psi. 75

Figure 4-14 Shows the load vs time plot for PSP 205. This test is performed at the constant shear stress value of 4050 psi. 75

Figure 4-15 Shows the load vs time plot for PSP 208. This test is performed at the constant shear stress value of 3000 psi. 76

Figure 4-16 Shows a combined plot of stress path for constant axial stress tests. 76

Figure 4-17 Shows the stress vs strain plot for the multi-stage triaxial test. Four different confining stress stages - 1500 psi, 2000 psi, 2500 psi, and 3000 psi were performed. 78

Figure 4-18 Shows the tangent strain ratio vs shear stress for all stages of the multi-stage triaxial test. The loading stage is unloaded when point of positive dilatancy (tangent strain ratio of 0.5) is reached. 78

Figure 4-19 Loading-based yield surface calculated from yield points of the Multi-stage triaxial test. 79

Figure 4-20 Shows the stress-strain plot of the single stage triaxial test. The test was concluded when the axial strain sensor was at limit. 80

Figure 4-21 Shows a plot of tangent strain ratio vs shear stress for the single stage triaxial test. This plot is used to pick the yield point i.e., the shear stress value when the tangent strain ratio reaches 0.5. 80

Figure 4-22 Shows a combined plot of tangent strain ratio and shear stress. Yield stress points from each stage of the multi-stage triaxial test and the single stage triaxial test are used to map the yield surface..... 81

Figure 4-23 The yield point from single stage triaxial test (SST) plotted on the multi-stage triaxial test (MST) yield surface shows perfect match. This observation validates the use of multi-stage triaxial test from determining loading-based yield surface..... 81

Figure 4-24 The combined plot of four constant axial stress tests showing the evolution of axial strain with increase in shear stress..... 82

Figure 4-25 Shows the combined plot of four constant axial stress tests showing the evolution of volume strain with decrease in mean effective stress. 83

Figure 4-26 Shows the combined plot of tangent strain ratio vs mean effective stress for all tests in the set of constant axial stress tests. As can be seen, all the curves touch the point of positive dilatancy..... 85

Figure 4-27 Shows the yield points of the constant axial stress unloading tests in the mean effective stress - shear stress plane. The slope of the yield surface is 1.07, similar to the triaxial loading yield surface but the yield constant is different. 86

Figure 4-28 The combined plot of three constant shear stress unloading tests showing the evolution of axial strain as we progress through the tests. The shear stress maintains a constant value as it is a boundary condition for this set of tests. 87

Figure 4-29 Shows the combined plot of three constant shear stress unloading tests showing the evolution of volume strain with decrease in mean effective stress..... 88

Figure 4-30 Shows the yield points of the constant shear stress unloading tests in the mean effective stress - shear stress plane. The slope of the yield surface is 1.07, similar to the triaxial loading yield surface but the coefficient is different..... 89

Figure 4-31 Shows the summary plot of the three yield surfaces obtained from experiments. All yield surfaces have similar slope with different yield constants..... 90

Figure 4-32 Shows the sample yielding behavior on different stress paths. The constant axial stress unloading test has the lowest yield surface while the triaxial loading stress path has the highest yield surface in this data set. 91

Figure 4-33 Shows the yield constant obtained from the yield surface plotted against the slope of the stress path angle..... 92

Figure 4-34 Shows the yield points calculated from the yield function along different stress path angles. The triaxial yield surface predicted yield points significantly overestimate those predicted from the yield function in the unloading phase by maximum of 37%. 96

Figure 6-1 A graphical representation of MCC model with its yield surface, critical state line and maximum consolidation stress in a mean stress - shear stress plot..... 117

Figure 6-2 A graphical representation of compaction and swelling curve. The slopes λ and κ are calculated from these curves..... 119

Figure 7-1 Shows the calibrated MCC model for triaxial stress path ramp of PSP 214. The yield surface is shown in blue; the critical state line is shown in green and the triaxial stress path is shown in red. 121

Figure 7-2 Shows the simulated strain data and experimental strain data plotted together. There is a good match between the two data sets indicating a good model fit..... 122

Figure 7-3 Shows the MCC model fits for the 1st injection (A), 1st depletion (B) and last depletion stress path for PSP 214. A simulated yield surface with its critical state line and the stress path taken by the sample and with experimental axial strain data recorded from the lab measurements are plotted. 123

1. INTRODUCTION

Injection geomechanics is an integral part of a lot of subsurface operations such as nuclear waste disposal, carbon sequestration and storage, secondary and tertiary oil and gas recovery, geothermal energy, and wastewater disposal among others. Any physical interaction with the sub-surface requires a conduit. This conduit is a well bore in most cases. Integrity of the wellbore and sub-surface during injection is imperative to successful containment of fluids (such as carbon dioxide, wastewater and nuclear waste).

The mechanical behavior of the target sub-surface during injection can be accurately predicted if

- In-situ stress variations in the sub-surface and,
- Rock mechanical behavior of the sub-surface

can be modelled. These two parameters are key parameters in any geo-mechanical modeling of sub-surface. Geo-mechanical models are used in all stages throughout the life of a reservoir for modelling various processes such as borehole stability (Predein et al., 2015), completion (Zillur et al., 2003) and fracture designs (Guerra et al., 2012), depletion induced compaction (Younessi et al., 2018), secondary recovery (Liu et al., 2021) and tertiary recovery processes (Cai et al., 2020) among others.

1.1 In-Situ Stress Estimation

Estimation of in-situ stresses is usually performed in the field with logs and frac tests. Vertical stresses are can be estimated with high degree of confidence from overburden using density logs (Eaton, 1972). Horizontal stresses are not straight forward to quantify in the field. Horizontal stress magnitudes and directions are estimated in the field from borehole image logs (Nian et al., 2016), caliper logs (Han et al., 2018), density logs (Jimenez et al., 2015) and di-pole

sonic logs (Sinha et al., 2015). Another technique used in the field to measure horizontal stress is fracture tests such as leaf-off tests (Gjonnes et al., 1998), mini-frac tests (Bree et al., 1989; Shlyapobersky et al., 1988), formation integrity tests (Breckels et al., 1982) and diagnostic fracture injection tests (Mostafavi et al., 2020) among others. Above techniques estimate in-situ stresses at the time of measurement. Thus, they are a snapshot of stress field in time when the measurements were made. Typically, very few field tests are authorized and completed, often in different wells or different sections at different time. To predict in-situ stress changes during injection, laboratory-based measurements in conjunction with field measurements are necessary. Hettema et al. (2000) presented a technique to predict horizontal stresses from changes in pore pressures using stress path coefficients.

Reservoir stress path coefficients have been defined as follows

$$\gamma_h = \frac{\Delta\sigma_h}{\Delta p_p} \quad (1.1)$$

and

$$\gamma_v = \frac{\Delta\sigma_v}{\Delta p_p} \quad (1.2)$$

where γ_h and γ_v are called horizontal stress path coefficient and arching coefficient, respectively. $\Delta\sigma_h$, $\Delta\sigma_v$, and Δp_p are the changing in-situ total horizontal stress, vertical stress, and changing pore pressure respectively.

For producing reservoirs with depletion, the horizontal stress path coefficient is referred to as the depletion coefficient and for reservoirs with injection, it is called injection coefficient. When the reservoir is laterally infinite, i.e., with a very low aspect ratio of reservoir thickness over reservoir drainage radius, the total change in vertical stress σ_v is assumed to be negligible. Hence,

the arching coefficient is zero, and the boundary condition followed by the reservoir is uniaxial strain (Holt et al., 2016).

Significance of this horizontal stress path was traditionally associated with prediction of reservoir compaction and activation of nearby faults in near critical state (Zoback et al., 2002; Chan et al., 2004). Drilling new wells in a depleted brown-field reservoir has a higher risk of wellbore breakouts and accidental fracturing of the reservoir. The upper bound of mud weight window is related to value of minimum horizontal stress (with some safety margin) (Lavrov, 2016; Davison et al., 2016). For a permeable depleted zone, depletion is associated with increased risk of mud losses during in-fill drilling operations. If the stress path coefficient during injection is not the same as depletion, the incremental horizontal stress during injection will not be enough to restore it to pre-depletion levels. Therefore, accurate determination of both depletion and injection coefficients is essential to mitigating injectivity problems during secondary recovery. A couple of field case studies are provided to understand the complexity of measuring these values in the field.

Santarelli et al. (1998) reported a field case study of a poorly consolidated sandstone reservoir in North Sea. They deduced that reservoir stress path on depletion and injection are different. They studied the central part and heavily faulted southern part of the reservoir. The minimum horizontal stress was inferred from fracturation pressures. They found the depletion coefficient in the central part was higher than that of the heavily faulted southern part and the minimum horizontal stress after injection was not the same as post-depletion levels. They concluded that the total minimum stress in the field is dependent on maximum depletion and not the present level of pore pressure. The depletion coefficient was reported to be non-zero whereas the injection coefficient was zero for the central part. There is irreversibility upon reloading, and

this can be explained by an elasto-plastic behavior. At large scale, the reservoir behavior is thought to be of a rigid plastic material that does not deform upon unloading.

Davison et al. (2016) presented two case studies to study the changes in in-situ stresses and stress path coefficients during depletion and injection. The total minimum horizontal stress was inferred from evaluation of Equivalent Circulating Density (ECD) values and LOT/FIT tests during drilling. The reservoir pressure at depletion and injection was predicted from lost circulation of drilling mud events. In the first study, they found that injection coefficient was about 0.25 and the depletion coefficient was about 0.43. This case study used drilling data (ECD and PWD) to estimate total minimum horizontal stress in complex radial faulting reservoir enhancing reservoir compartmentalization which might not be the representative total minimum horizontal stress value. In the second study in South China Sea, they studied one well completed with a multi-cased and perforated completion. They estimated total minimum horizontal stress from Step rate tests by extrapolating the slope to zero injection rate. The depletion coefficient was about 0.90 but the injection coefficients were different for different perforation intervals. For one perforation interval with unconsolidated sands, the injection coefficient was reported to be zero due to possible shear failure. For the other interval without shear failure, it was 0.32. They summarized the two studies saying depletion coefficient and injection coefficients are different and dependent on the maximum depletion value and rock properties.

Total minimum horizontal stress and pore pressure values presented here have been inferred from variety of sources and represent stress changes closer to the wellbore. There is considerable uncertainty in projecting these values to far-field stress state. The interpretation of these data is subject to inherent assumptions and obtaining coherent representative data to estimate the stress path values is often very difficult and expensive. The field case studies presented above reinforce the value of doing laboratory measurements.

Most of the other research work in the laboratory is focused on depletion (Addis, 1997; Skomedal et al., 2002) and its effects on borehole stability (Aadnoy, 1990), permeability (Rhett et al., 1992, Bouteuca et al., 2000) and compaction (Brignoli et al., 2004; Schutjens et al., 2008). Some publications focus on permeability variation during injection (Yale et al., 2010; Wang et al., 2015; Soreide et al., 2014; Louis et al., 2018).

Many researchers have published experimental work on evaluation of stress path coefficients. Holt et al. (2016) performed a set of laboratory experiments to simulate depletion followed by injection on soft ($\phi = 30\%$, $E = 145$ Kpsi, $\alpha = 0.98$) and stiff ($\phi = 20\%$, $E = 4.3$ Mpsi, $\alpha = 0.67$) sandstones. Soft sandstones were reported to have lower depletion coefficient value (~ 0.47) compared to injection coefficient (~ 0.57) and stiff sandstones had higher depletion coefficient (~ 0.40) compared to the injection coefficient (~ 0.29). They concluded that stress path coefficients depend on the stiffness of the material and stress path direction (loading or unloading).

Rafieepour et al. (2017) reported an experimental study to characterize the effect of depletion and subsequent injection on Castlegate ($\phi = 26\%$, $E = 1.6$ Mpsi, $\alpha = 0.68$) sandstone for different boundary conditions of the test samples. They found that depletion coefficient was higher than the injection coefficient in all cases. The sample behavior was similar to the stiff sandstone behavior observed by Holt et al. (2016). They concluded that the stress path coefficient values for depletion and injection are higher for boundary conditions that restrict expansion of the test sample in any direction (such as uniaxial strain or plane strain boundary conditions).

There is a need for study of effects of injection on in-situ stress variations in unconsolidated sands. The current research focused on determining the stress path coefficients during depletion and injection in the far-field stress conditions representative of deep-water unconsolidated sands reservoir in the Gulf of Mexico. Holt et al., (2016) and Rafieepour et al.,

(2017) had a stiffer material with some cohesion whereas the material in this research is unconsolidated sands with zero cohesion. A true horizontal stress path coefficient based on changes in pore pressure are presented in this work while Holt et al. (2016) performed effective stress measurements.

The presented work aims to investigate the effect of pore pressure injection on stress path coefficients in unconsolidated sands, presence of hysteresis (if any) during multiple depletion – injection cycles and explain the observed behavior with a physical mechanism.

1.2 Rock Mechanical Behavior Prediction

The other half of the puzzle is prediction of yield behavior of rocks under injection or unloading. Rocks are granular materials with pore spaces occupied by fluids (water, oil or gas). The total stresses applied to the rocks are supported by the rock framework and the fluid present in pore spaces. The rock framework supports the effective total stresses (effective stress = total stress – pore fluid pressure). Therefore, in order to predict mechanical properties of the rock in in-situ conditions, we need to take into account, the total stresses applied, the fluid pressure inside the pore spaces and the strength of the rock framework itself (Jaeger et al., 2007). To isolate the mechanical response of the rock, we will henceforth, use effective stress in this sub-section, to discount for the fluid pressure supporting the fraction of total stresses.

The mechanical response of rocks is stress path and stress magnitude dependent. In addition, the inherent mechanical properties (strength, stiffness, cohesion etc.) play a vital role (Lambe, 1967). The presented research is focused on investigating the effects of injection of unconsolidated sands under different stress path directions and stress magnitudes. The stress path direction in the mean effective stress (p) – shear stress (q) space is the relative change in effective mean stress and shear stress. It is represented as a curve in p - q space (Lade et al., 1976).

The stress path directions during depletion and injection are different. When a well is in production mode, the reservoir pressure is reducing. Consequently, the mean effective stress supported by the rock matrix is increasing. In other words, the rock matrix is being 'loaded' during production. On the other hand, when a well is under injection, the reservoir pressure is increasing. Therefore, the mean effective stress supported by the rock matrix is reducing. Hence, the rock matrix is being 'unloaded'. The role of shear stress or differential stress is significant to determine the response of rock matrix during depletion and injection. Although the shear stress is not affected by pore pressure, with change in mean effective stress, the corresponding change in magnitude of shear stress dictates rock deformation behavior (Zoback, 2007).

Unloading based failure characterization has been studied widely in the mining and tunneling industry. Researchers have published work on triaxial unloading tests performed on very stiff igneous or metamorphic samples such as granite and marble etc.

Xie et al. (2004) performed loading and unloading tests on Plagioclase Gneiss and Granite Gneiss samples. Huang et al. (2014) performed axisymmetric unloading and conventional loading triaxial tests on marble samples. Dai et al. (2014) conducted an extensive program of 39 specimens to investigate triaxial unloading mechanical properties of granite. Li e. al. (2017) studied the evolution of energy under loading and unloading triaxial tests in granite samples. Yin et al. (2012) studied the failure characteristics of consolidated sandstone under effect of static and dynamic loading and associated elastic-potential energy. Zhu et al. (2019) compared direct shear tests with constant normal stress and decreasing normal stress on sandstone. Similar research has been published by researchers with granite (Huang et al., 2001; Du et al., 2015), dacite (Wang et al., 2020), marble (Chen et al., 2008), soft rock (Wang et al., 2012), limestones (Gao et al, 2012; He et al., 2010), salt rock for gas storage (Guo et al., 2012), coal bed methane (Zhang, 2017), soft coal (Liu et al., 2017), red sandstone (Du et al., 2015).

They conclude that loading yield stresses are similar to unloading yield stresses i.e., no practical impact of stress path direction of yield stress. The materials used in the above studies are stiffer with high yield stresses than unconsolidated sands. They do not have pore-fluid effects and research aims to understand the effect of excavation on the surrounding rock mass with particular focus on stability.

Many researchers have published similar work on soft soils as well. Barla (2007) studied unloading behavior consolidated clays in predicting stability of tunnels. Zhou (2013) reported results on Guangzhou soft soils for both conventional triaxial shear tests and unloading direct shear tests. Huang et al., (2020) performed unloading tests on soft soils. They conclude that failure stresses are stress path direction dependent. The maximum magnitudes of applied stresses ranged between 15 psi to 250 psi.

In the oil and gas industry, extensive studies have been completed in unconsolidated sand reservoirs to investigate the effects of injection. Researchers have investigated the strength properties of oil sands in unloading stress paths (Hamoud, 2012; Oldakowski, 1994; Touhidi, 1998). Chalaturnyk et al. (1996) studied effects of temperature on strength properties of oil sands. These researchers concluded that the loading and unloading stress path do not impact yielding behavior of oil sands. The research publications mostly focus on Canadian Oil sands which have a very low effective stress (50-250 psi). The major focus of their research was to quantify variation in permeability during injection. They found no difference between loading and unloading yield stresses.

Scarce research is published in the literature to explain the effect of injection on the mechanical yield behavior of unconsolidated sands. The proposed research work aims to understand the effects of injection on unconsolidated sands. The referenced research work for

unloading based tests is performed on geo-technical or mining and tunneling engineering related materials with high values of UCS whereas our reservoir (unconsolidated sands) of interest has practically no UCS value. The unconsolidated sands are characterized by much higher porosity, and higher ductility compared to the materials used in mining and tunneling industry. Our stress magnitudes (~2000 psi) are one order of magnitude higher than the effective stresses experienced by oil sands. Since, there is a stark contrast between the material properties, the proposed research work adds new information and advances the rock mechanics science. To our best knowledge, unloading tests have not been published with unconsolidated sands to compare the failure yield surfaces and develop a constitutive model to correlate loading and unloading yield surfaces with high pressure magnitudes.

The presented work aims to investigate the dependence of stress path magnitude and direction on the yielding behavior of unconsolidated sands under injection and predict yielding behavior under different stress path directions and magnitudes.

In order to accurately predict unconsolidated sand reservoir behavior in the lab, we need a large number of representative samples. Since, deep-water unconsolidated sand cores are limited and highly vulnerable to alteration during coring, a consistent and representative sample preparation procedure to create a reservoir analogue is vital. This technique ensures sample reproducibility and representativeness to the reservoir's mineralogy and geo-mechanical properties. This dissertation is organized in the following way –

- Introduction
- Sample preparation, material and equipment
- Stress path coefficients
 - Test procedure

- Data analysis
 - Results and Discussions Conclusions and future work
- Yield surface and stress path directions
 - Test procedure
 - Data analysis
 - Results and Discussions
 - Conclusions and future work
- Combined conclusions and future work

2. SAMPLE MATERIALS, PREPARATION AND EQUIPMENT

Reservoir of interest for this research work is deep-water unconsolidated sandstone reservoirs. To study an unconsolidated sands reservoir's geo-mechanical properties, we need to have well-preserved sub-surface samples for best results. Since, most of these reservoirs are offshore, reservoir rock access and availability of core-material for experimental studies is very difficult and expensive. In addition, the friable nature of unconsolidated sands makes it difficult for handling of core material during tests. Therefore, there is a need to make synthetic samples that are representative of the geo-mechanical properties and mineralogy of the sub-surface material. The synthetic sand pack preparation technique should produce consistent and repeatable samples representative of the sub-surface material.

2.1 Analogue Material

Since reservoir core-material is not readily available, an analogue material is used. For the analogue to be representative of the sub-surface, it should have comparable –

- Mineralogy
- Texture and angularity
- Grain size distribution
- Porosity
- Mechanical properties and creep at in-situ conditions

to the reservoir of interest. Florida sand has been used as a starting material in this work as it is an analogue material to the Gulf of Mexico reservoirs in terms of mineralogy, texture and angularity.

Figure 2-1 shows the particle size distribution (PSD) of the Florida sand, as received from vendor, with a median grain size (D50) of 229 microns and a uniformity coefficient (Uc) of 1.84.

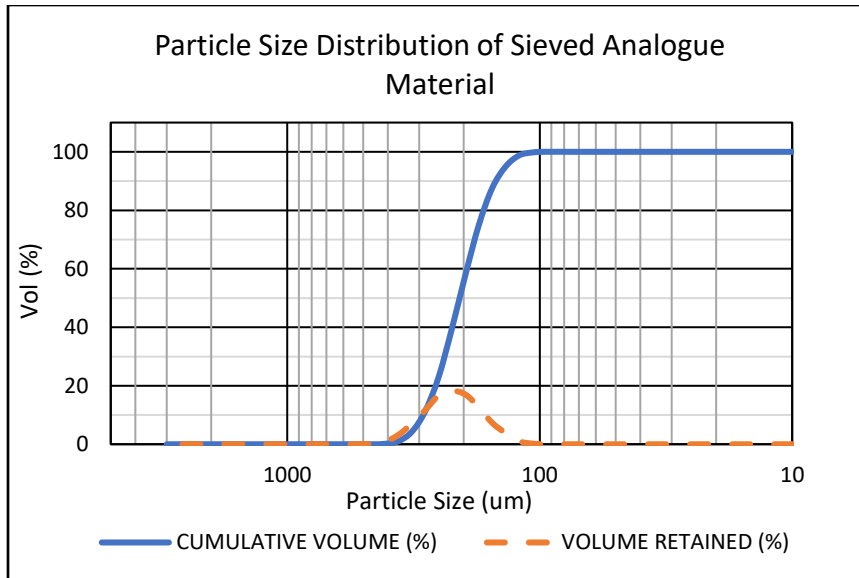


Figure 2-2 Shows the particle size distribution of the sieved analogue material. The sieved material selected for this work has D50 of 203 microns and U_c of 1.44.

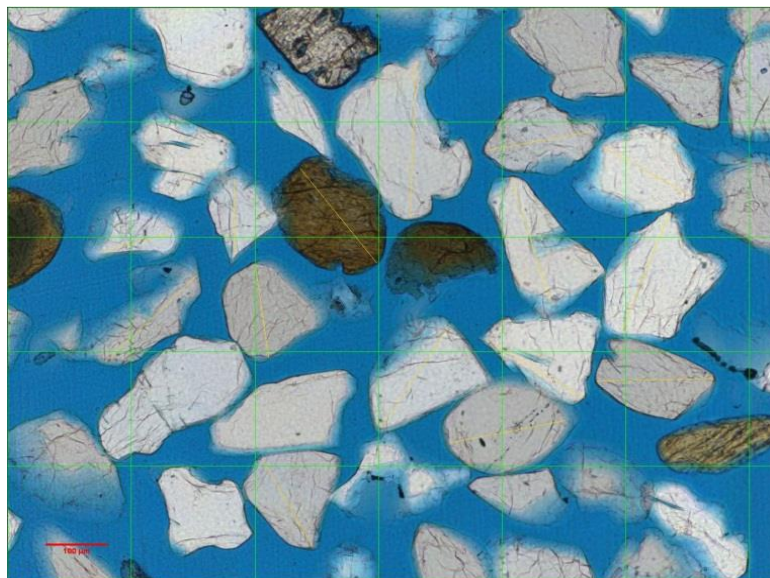


Figure 2-3 Shows a 2D thin section image of sieved analogue material in a grain mount under transmitted light. The material is predominantly quartz with very few heavy minerals present.

A 2D thin section image shows grains on the grain mount in Figure 2-3. The grains are sub-angular with more than 90% quartz. This thesis uses the sieved Florida sand as it contains mineralogy, grain size distribution, texture and angularity representative of reservoir materials.

2.2 Sand Pack Samples

After the analogue material is chosen, our next step is to use this sand to make cylindrical samples. The main objective is to identify and establish procedure that delivers homogeneous or uniform porosity sample consistently. In this section we will first review different sand pack preparation techniques available in the literature. Then, we will discuss the sand pack technique or procedure used.

2.2.1 Review of Sand Pack Preparation Techniques

There are different sand pack preparation techniques developed and presented in the literature for different types of experiments. Sand pack preparation techniques can be broadly categorized into dry and wet techniques. Many researchers have compared both techniques in terms of reproducibility and uniformity (Polikar et al., 1988; Touhidi, 1998; Wang et al., 2015). They concluded that selection of sample preparation technique depends on the grain size distribution of the sands and the type of tests to be performed. Sand with a non-uniform grain size distribution would produce layering in the pack under wet preparation techniques due to differential settling time for different grain sizes (Polikar et al., 1988; Kuerbis, 1988). A dry pack is preferable when clays are part of the pack to avoid swelling nature in addition to differential settling time. For permeability measurements as well as secondary recovery efficiency measurements wet packs are preferred to ensure 100% fluid saturation (Hamoud, 2012; Abdallah, 2014).

A Dry sand pack preparation method is followed in this work. It has evolved over the years. Many researchers used tapping of the core holder (Ivory, 1987; Hamoud, 2012; Abdallah, 2014; Wang et al., 2015) and vibrating table (Polikar et al., 1988; Oldakowski, 1994; Arya, 2018) to increase packing efficiency. The following section provides a detailed procedure followed for preparation of dry sand-packed samples.

2.2.2 Sample Preparation Procedure

A dry sand pack preparation procedure by Arya (2018) is used in this work. A 1/6" thick Kapton sleeve with 1-inch diameter and 3-inch length is cut from a longer Kapton sleeve. It is sealed at one end with a porous Alundum frit with sealing tape wrapped around it. The sand grains are pluviated into the Kapton sleeve while the sleeve is shaking on a vibrating table. After pluviating sand to a height of about 2.5 inches, the top of the sand pack is sealed using another porous Alundum frit with sealing tape. This dry pack produces a sand pack of porosity of about 37 percent. The dry sand pack is placed in a beaker of water to imbibe water and fill all the pores through capillary action. The sand pack is then submerged slowly in liquid nitrogen from bottom to top to freeze water in the pores. Any remaining air gaps will be saturated due to the expansion of water during the slow bottom to top freezing process. The Kapton sleeve is peeled, and the frozen sample is cut to dimensions of about 2-inch length. If the sample was not fully saturated, it would fall apart after peeling, as the cohesion force to hold the sample intact is provided by ice. The sample dimensions are measured three times at three different places, and the mean values of length and diameter are recorded. The sample is kept in a liquid nitrogen bath until it is ready to be mounted into the loading test cell.

The sand pack procedure outlined delivers test sample with representative reservoir materials and uniform porosity. To bring the sand pack to comparable reservoir porosity and mechanical properties, a sample consolidation step is required. This involves loading the sample and uses a triaxial cell. The following section details the triaxial equipment used in this research work.

2.3 Experimental Setup

A triaxial load cell is used for consolidation experiment. The experiment setup has two major components

- Axial, confining and pore pressure setup and
- Strain gauges.

2.3.1 Axial, Confining and Pore Pressure Setup

Figure 2-4 shows the experimental schematic setup. The axial load on the sample is provided by a 2" bore piston from the top. It is servo controlled and can be loaded at different rates such as constant axial strain rate, constant radial strain rate, constant axial stress rate etc. The radial or confining stress is applied using hydraulic oil (Multitherm IG-4). A servo-controlled pump is used to vary the confining stress. All operations are carried out in MR Compaction software designed by Metarock Laboratories. Two Heise DXD pore pressure transducers are outside the cell. The pore pumps are connected through the transducers and have a displacement volume of 50 cc. The pore lines are connected through the end caps to the sample.

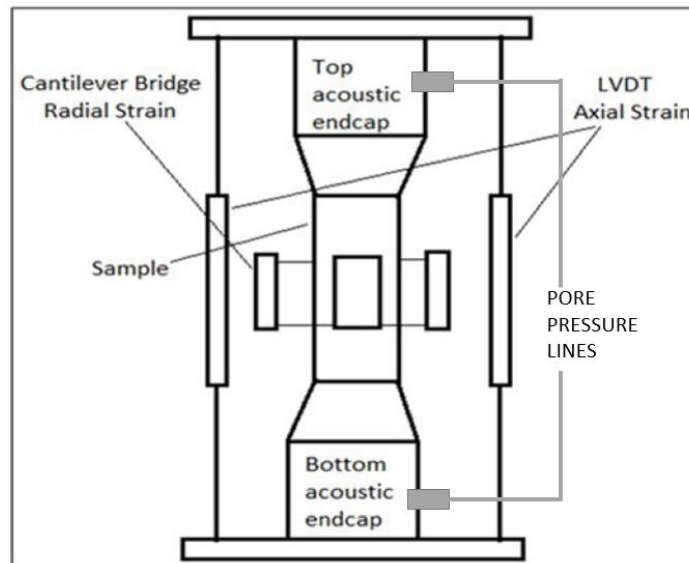


Figure 2-4 A schematic diagram of the sample setup in the stress cell. Average of the two measurements from LVDTs is used as axial strain. Average of the two measurements from cantilever bridge is used as radial strain.

2.3.2 Strain Gauges and Calibration

Axial strain is measured by two Linear variable differential transducers (LVDTs) mounted on the endcaps (Figure 2-4). Average of both LVDTs is the recorded axial strain. A four-arm cantilever bridge is used to measure radial strain at two different points. Average of the two measurements is the recorded radial strain. Volumetric strain is a calculated parameter. It is calculated as the sum of axial strain and twice the radial strain. An internal load cell sits at the bottom of the pressure vessel. The sample with the endcaps sits on this load cell. All strain gauges are calibrated using micrometers. The calibration test is shown in Figure 2-5 and Figure 2-6. They are adjusted for pressure corrections by conducting a stiffness test using Tungsten billet and then verified using aluminum billet (Figure 2-7 and Figure 2-8). Therefore, the end-cap corrections as well as corrections for pressure responses are considered before testing a sample.

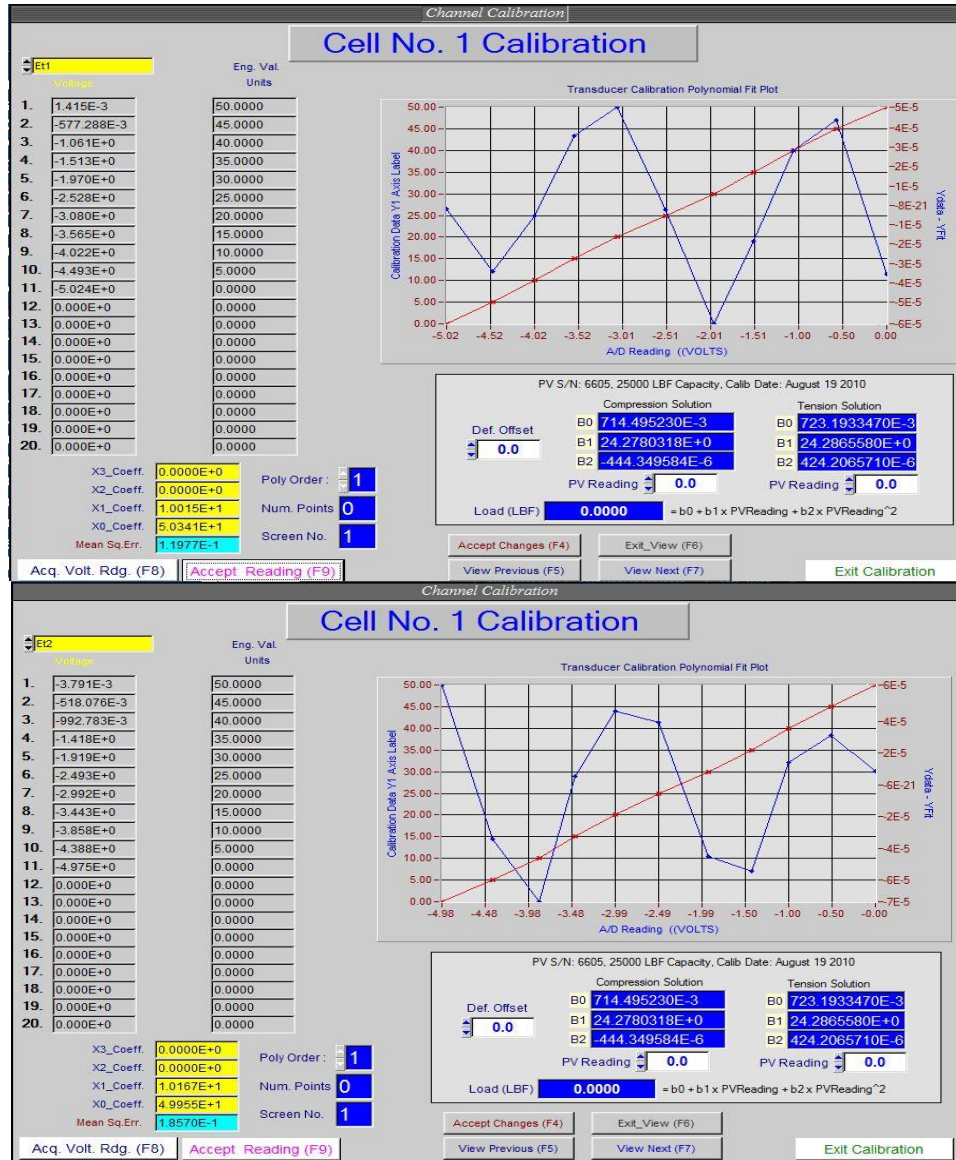


Figure 2-5 The calibrated values of the radial bridge using calibrated micrometers. Maximum measurement that can be made is 50 milli-inches (mils) and least count is 0.01 mils.

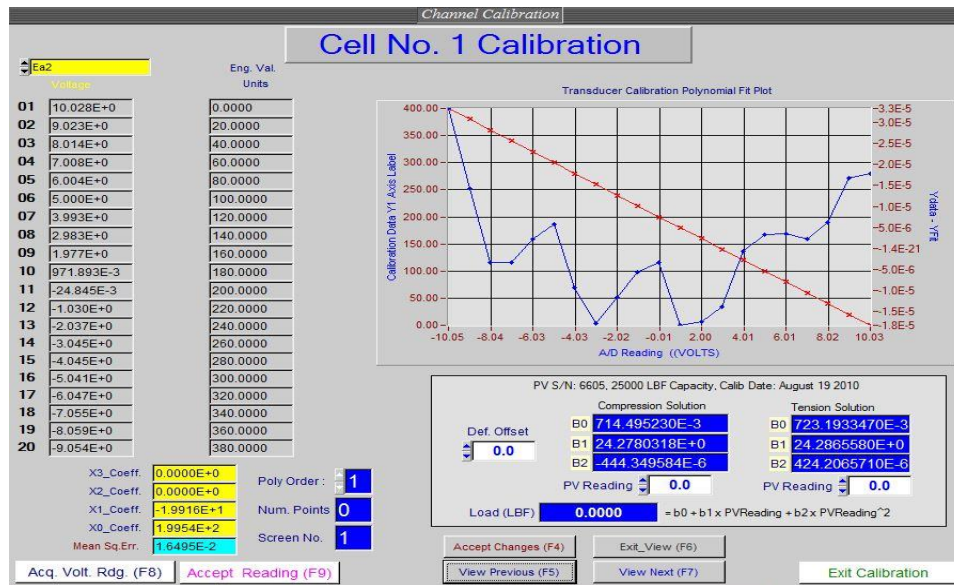
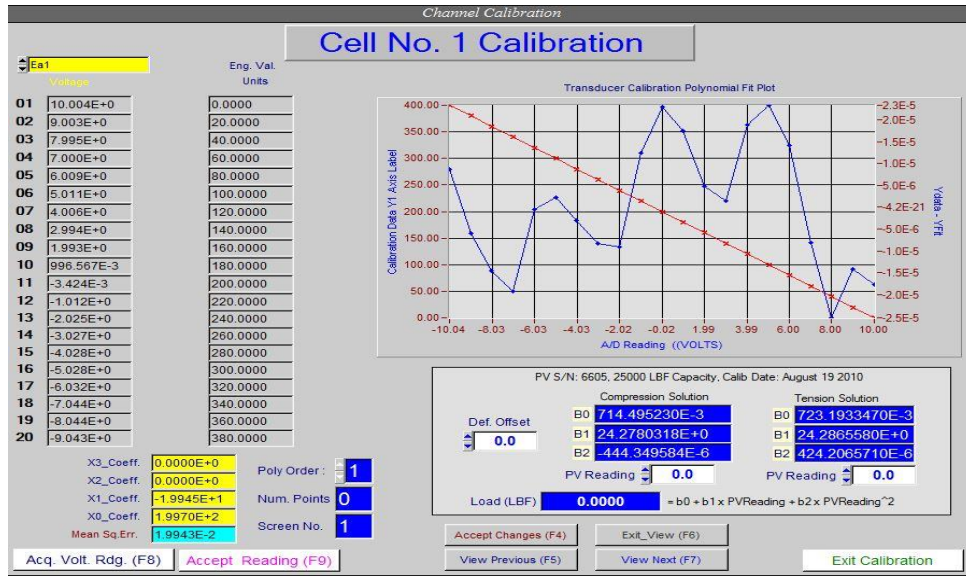


Figure 2-6 The calibrated values of both LVDTs using calibration micrometer. Maximum measurement that can be made is 400 mils. And least count is 0.02 mils.

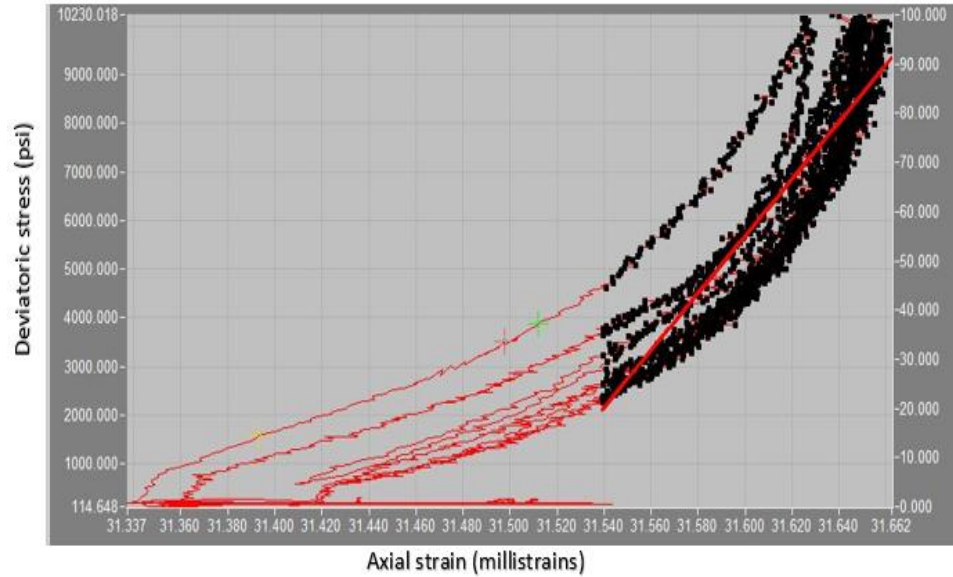


Figure 2-7 The stress-strain plot of stiffness test with Tungsten billet. The true Young's Modulus for Tungsten is 60 million psi. The calculated Young's Modulus is 58.9 million psi with an error of 1.8 %. The pressure corrections for the strain gauges are calibrated with Tungsten.

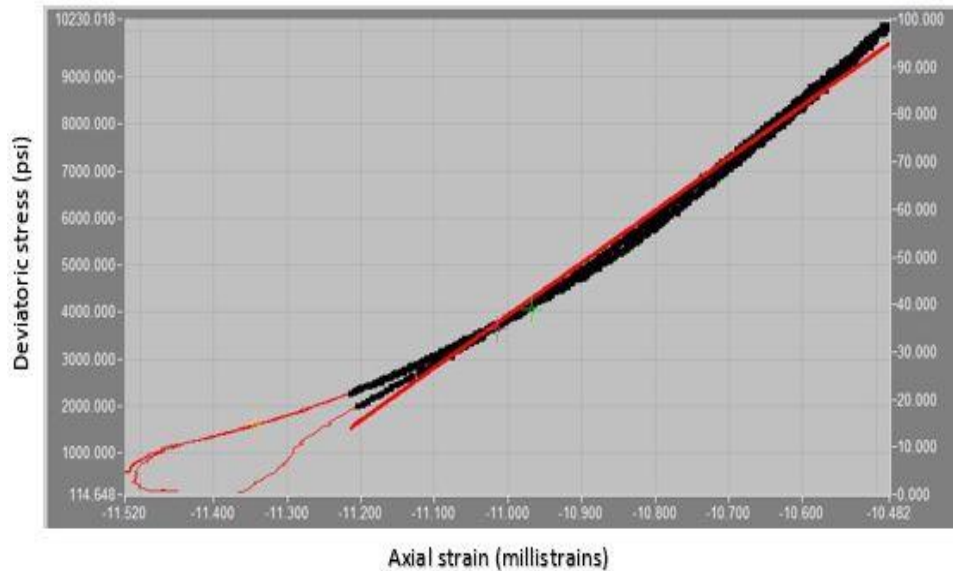


Figure 2-8 The stress-strain plot of stiffness test with Aluminum billet. The true Young's Modulus for Aluminum is 10 million psi. The calculated Young's Modulus is 10.94 million psi with an error of 9.4%. The pressure corrections for the strain gauges are verified with Aluminum.

After the triaxial cell is properly calibrated and tested to account for pressure effects, the sand pack is ready to be mounted in the cell for further testing.

2.4 Representative Analogue

In the previous sections, we determined the sand source for making an analogue for reservoir in terms of mineralogy, texture and angularity, and then sieved further to match the grain size distribution. We then used this sand to prepare or pack a consistent and uniform porosity test sample using a dry sand pack technique discussed by Arya (2018). To bring the sample material to comparable reservoir porosity and mechanical properties, we need to load and consolidate the test sample.

There are different sample consolidation techniques available in the literature. Oldakowski (1994) introduced two cycles of isotropic consolidation after dry sand pack is prepared to improve packing to a higher density and close to in-situ porosity values. The porosity values after consolidation improved by about 3 porosity units (40% to 37%). Arya et. al. (2018) compared two methods of sand pack consolidation. After making the dry pack, the sample was compacted in a triaxial cell. Two methods of compaction were studied – a single stress step and hold test, and a stress cycling technique. The single stress step and hold test was performed by applying a pre-defined peak hydrostatic or isostatic stress to the sample for about 24 hours while measuring the axial and radial strains. The stress cycling technique involved applying several load-unload stress cycles of the peak hydrostatic stress until the sample deformations were purely elastic (no significant plastic strains were observed). Arya (2018) concluded that the sample compacts two times more during stress cycling (volume strain of 2.95%) compared to using a single stress step and hold test (volume strain of 1.48%).

This stress cycling technique helps bring the test sample porosity closer or comparable to reservoir conditions. However, the analogue test sample should also be representative in terms of mechanical properties at in-situ conditions. The burial process for sediments in the subsurface takes millions of years where they are creep relaxed. Little to no grain breakage is typically

observed during the burial process. Since, we are trying to mimic reservoir rock, we would like to ensure that our samples are creep relaxed at the in-situ conditions with minimal amount of hysteresis during the sample preparation process (Bjorlykke, 2010). By selecting the peak stress level in the isostatic consolidation process to be similar to the mean-effective stresses of the target reservoir, we ensure the sample to be representative of the mechanical behavior of the target reservoir. During the isostatic consolidation process, the sample grain size characteristic also needs to mimic the burial process. The high initial load in the first stress cycle - zero to peak hydrostatic stress (Arya, 2018), is speculated to produce higher grain breakage since the sand grains did not have sufficient time to relax and reorient during this step.

The current work addresses the issue of potential grain breakage during sample consolidation process. Instead of applying the peak load in the first load-unload cycle, a gradual increasing hydrostatic load to the peak stress with each load-unload cycle is introduced. Each unload step provides time for the sample to relax and grains to reorient on the way to the peak stress value.

The above-mentioned consolidation procedure is followed for all samples presented in this work. The test procedure for the consolidation process is as follows:

1. The 2" by 1" sample is mounted in the triaxial cell while the sample is frozen. Sample is continuously sprayed with liquid nitrogen during the mounting process to keep it frozen.
2. The pressure vessel is closed, and a confining pressure of 500 psi is applied through the confining fluid pump.
3. A deviatoric load of 200 psi is applied and pore-lines are opened to atmospheric pressure.

The sample is left at this initial condition overnight for it to thaw and stabilize.

4. After the sample has thawed, the consolidation process is initiated. The hydrostatic load is increased to 1000 psi at 1 psi per sec loading rate.
5. It is then unloaded to 500 psi at the same rate.
6. The next few steps include these reload-unload ramps by increasing maximum magnitude of confining stress by 500 psi i.e., the peak values of confining pressure at the start of unload are 1500 psi, 2000 psi, 2500 psi, 3000 psi, 3500 psi and 4000 psi. The maximum magnitude of hydrostatic load, chosen in this study, is 4000 psi to simulate the reservoir conditions.
7. The unload-reload cycles are continued with the maximum magnitude of 4000 psi for several cycles. Figure 2-9 shows the load-unload cycle of confining stress. On the secondary vertical axis, the recorded axial strain is plotted.
8. The reload-unload process is stopped when the axial recoverable strain is more than 95% of the total strain consistently. The recoverable strain is the amount of strain that the sample recovers after the sample is unloaded back to the initial confining stress. It is calculated as the difference of the total strain at the peak value of confining stress and the residual strain at the end of unloading.

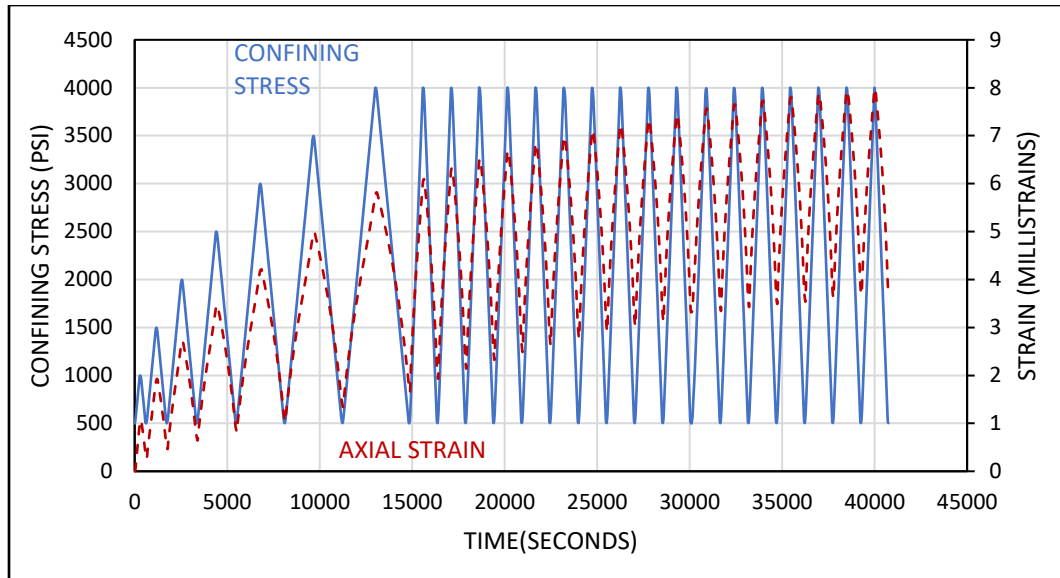


Figure 2-9 Shows the pre-consolidation process to make representative analogue. The Confining stress is increased at 500 psi amplitude to reach peak confining stress during the initial load-unload ramps. The test is terminated when response is elastic.

Figure 2-10 shows a plot of the percent of recoverable axial strain at the end of each load unload ramp. In the last few unload steps, the sample recovers more than 95% of total axial strain it had undergone during previous loading step. By performing multiple reload-unload ramps, we have significantly reduced plastic strains (less than 5% of total axial strain is not recovered) and associated hysteresis (Figure 2-11). The nearly elastic load-unload stage confirms that the sample is now creep relaxed.

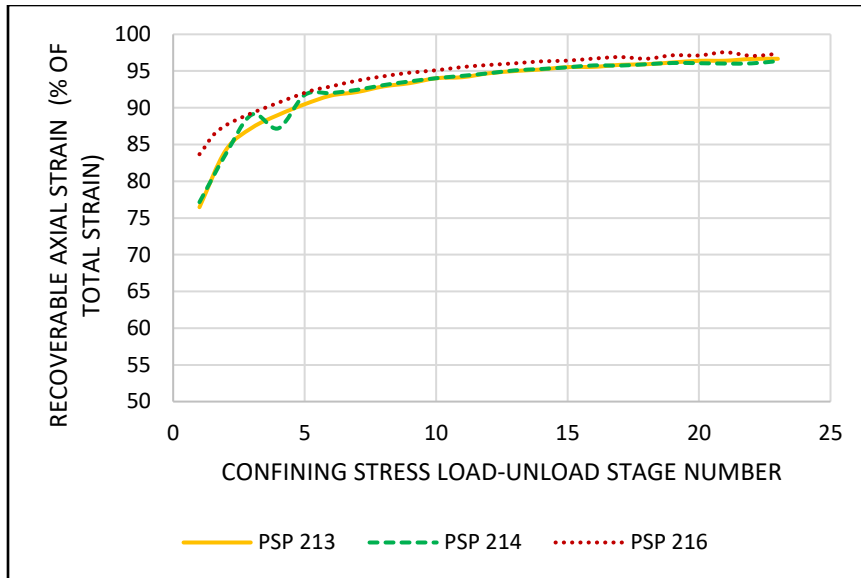


Figure 2-10 shows a plot of percent recoverable axial strain at the end of each load-unload stage during consolidation experiment. The experiment is terminated when percent recoverable strain is consistently above 95%.

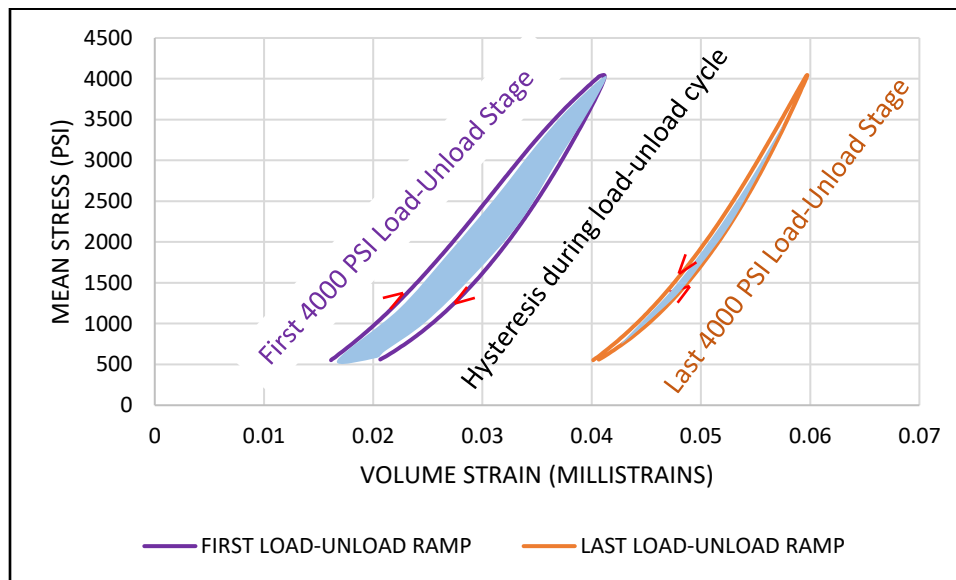


Figure 2-11 A plot of Axial Strain vs Mean Stress comparing hysteresis on the first maximum magnitude load-unload stage and the last maximum amplitude load-unload stage. Associated Hysteresis for first cycle is high compared to last cycle where the load and unload paths overlap each other.

This chapter described our requirements and procedures to produce synthetic sand pack test samples to be used in our study. The requirements are to deliver consistent and uniform samples that represent mechanical deformation responses of reservoir sands. We identified and sieved the Florida sand to be our reservoir analogue material based on comparable mineralogy,

grain size distribution, texture, and angularity. We used this sand to prepare our test samples with a dry sand-pack technique to ensure delivery of consistent and uniform porosity samples. Finally, to bring the test samples to in-situ conditions with comparable porosity, minimum grain breakages and creep relaxed, we introduced a new cyclic load-unload consolidation test procedure. This consists of increasing the hydrostatic load gradually to the pre-defined reservoir mean effective stress during the load-unload cycles. With test samples at the desired reservoir mean effective stress level, we are now ready to investigate the effects of injection on stress path coefficients, yield surfaces, and the associated hysteresis.

3. STRESS PATH COEFFICIENTS

This chapter is focused on investigating the effects of injection on variation of minimum in-situ stresses in the samples prepared in chapter 2. Variation of minimum in-situ stress with change in pore pressure is quantified by reservoir stress path coefficients.

Reservoir stress path coefficients have been defined as follows

$$\gamma_h = \frac{\Delta\sigma_h}{\Delta p_p} \quad (3.1)$$

and

$$\gamma_v = \frac{\Delta\sigma_v}{\Delta p_p}, \quad (3.2)$$

where γ_h and γ_v are called horizontal stress path coefficient and arching coefficient, respectively. $\Delta\sigma_h$, $\Delta\sigma_v$, and Δp_p are the changing in-situ total horizontal stress, vertical stress, and changing pore pressure, respectively. Holt et al., (2016) used effective stress concept to calculate horizontal stress path coefficients using –

$$\gamma_h = \alpha \left(1 - \frac{\Delta\sigma_r}{\Delta\sigma_z} \right), \quad (3.3)$$

where γ_h is the horizontal stress path coefficient, α is the Biot's coefficient, $\Delta\sigma_r$ is the radial or confining stress change, $\Delta\sigma_z$ is the axial stress change. Poro-elasticity assumptions have been made by Holt et al., (2016) to convert equation 3.1 to equation 3.3. In this research work, pore pressure depletion and injection tests with uniaxial strain boundary conditions are made to calculate the stress path coefficients from definition of horizontal stress path coefficients.

The boundary conditions for far field reservoir compaction and depletion process is best represented by a uniaxial – strain stress path (Figure 3-1). Since, most reservoirs are laterally extensive compared to reservoir thickness, the subsurface boundary conditions dictate that the

vertical strain during depletion is of orders of magnitude higher than the strain in horizontal directions (Riazi et al., ASTM 2016). This is equivalent to a reservoir with negligible stress arching support or with a constant vertical stress such that there are no vertical stress changes caused by pore pressure changes.

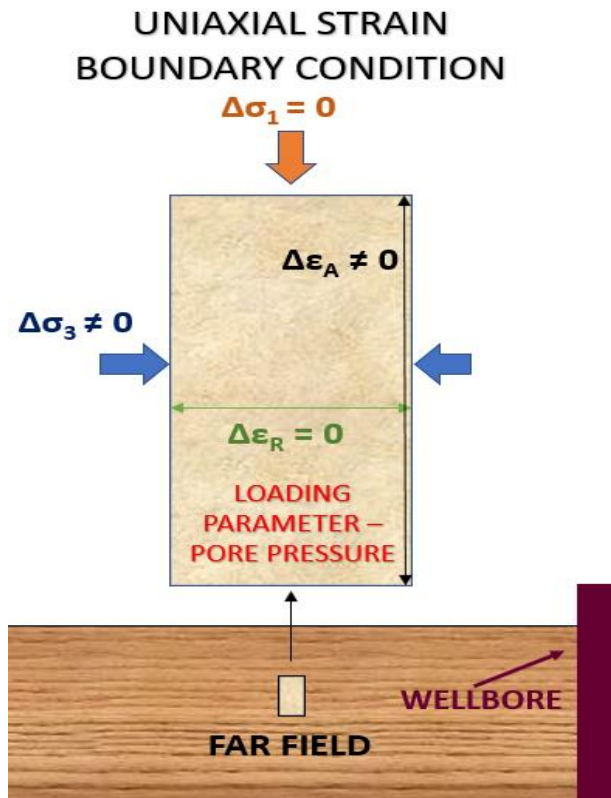


Figure 3-1 Shows the Uniaxial strain boundary condition defined by Riazi et al., ASTM 2016. The axial stress is constant, pore pressure is the operating parameter and the confining pressure changes to keep the radial strain constant. The sample is deforming axially and with radial strain constant.

In our laboratory studies of horizontal stress path coefficients, our test samples are subjected to the Uniaxial strain boundary condition (Figure 3-1). The axial stress is kept constant ($\Delta\sigma_v = 0$), the pore pressure (Δp_p) is the operating parameter, and the confining stress ($\Delta\sigma_h$) is the measuring parameter. With change in pore pressure, the confining pressure changes to keep the radial strain constant, thus, satisfying the Uniaxial strain boundary condition (Riazi et al., ASTM 2016). In the following sections we will describe the loading procedure for all samples in this chapter.

3.1 Test Procedure

In Chapter 2, we presented our approach in preparing and consolidating the test sample to the representative reservoir conditions. Following the consolidation process and after resetting sample dimensions to the value at the end of the consolidation step, the sample is ready to be loaded to the initial stress conditions of our study.

A total of three stress path coefficient tests have been performed. Table 3-1 shows the initial conditions of each test.

Table 3-1 Shows the initial conditions at the start of the pore pressure uniaxial strain tests for three samples under study. All samples start with similar values of mean effective stress and shear stress. The mean stress p' is defined in Equation 3.6, and shear stress q is axial stress minus confining stress.

SAMPLE	AXIAL STRESS (PSI)	PORE PRESSURE (PSI)	CONFINING STRESS (PSI)	MEAN EFFECTIVE STRESS, p' (PSI)	SHEAR STRESS, q (PSI)
PSP 213	7400	3000	5300	3000	2100
PSP 214	7400	3250	5300	2750	1850
PSP 215	7600	3000	5500	3200	2100

Although the magnitudes of stresses at initial test stress conditions (p' and q) for the samples are different, the stress path followed by each sample to reach the initial test stress conditions is the same. Figure 3-2 shows the stress path followed by the samples to reach initial test stress conditions. The first part of the stress path is ramping up the pore pressure while keeping the effective horizontal stress and the effective vertical stress constant. This step increases the total stresses while the keeping the effective stresses constant. The second part of the stress path involves increasing the confining stress while keeping the shear stress and pore pressure constant. This part is like an isostatic stress path. The last part is increasing the axial stress to reach the initial test conditions. This part is like a triaxial loading path. The ramping of

individual stresses is done in this order to minimize grain breakage and remain as far away from expected yield surface as possible (Figure 3-3).

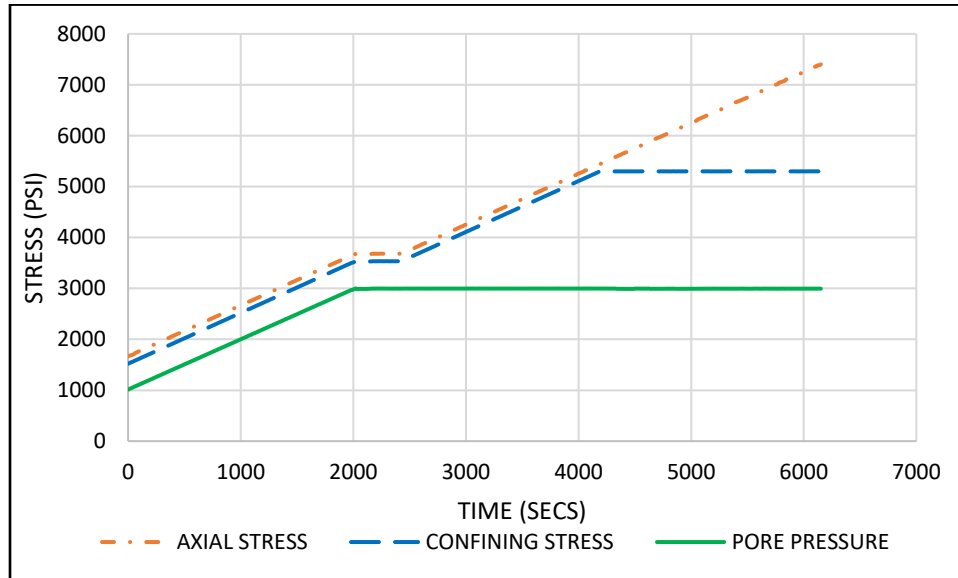


Figure 3-2 Shows the stress path followed to reach the initial stress conditions. First, the pore pressure is raised first followed by the confining stress, and the axial stress.

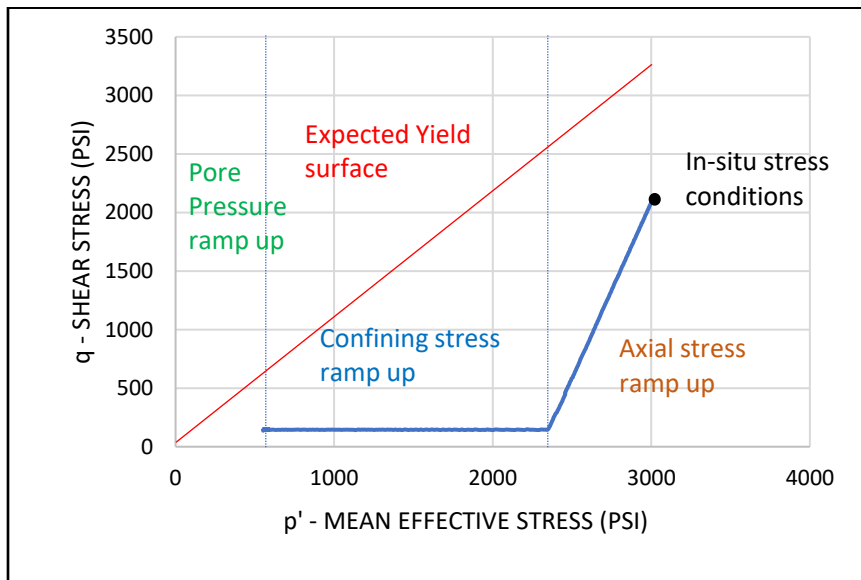


Figure 3-3 Shows the stress path taken to reach initial test conditions in a mean effective stress – shear stress space. The pore pressure is ramped up first followed by confining stress and then axial stress to ensure maximum distance from the estimated yield surface.

After reaching the initial test conditions, each sample is designed to undergo a different stress loading process. These tests are designed to study the effects of changing pore pressure

magnitude and direction (depletion and injection) cycle on the calculated stress path coefficients and hysteresis effects on repeat ramps.

For the first test of sample PSP 213, Figure 3-4 depicts the stress path used. This starts with a depletion or loading path by reducing the pore pressure from 3000 psi to 1000 psi. The confining stress also reduces to keep the radial strain constant. At the end of depletion, the sample is subjected to injection or unloading by increasing the pore pressure back to the same magnitude of 3000 psi. The confining stress reacts to changes in pore pressure and increases to a value higher than the initial value. Depletion-injection repeat ramps were conducted to study hysteresis effects in this stress path. The end points of depletion and injection during the repeat ramps were of the same magnitude as the first depletion - injection ramp.

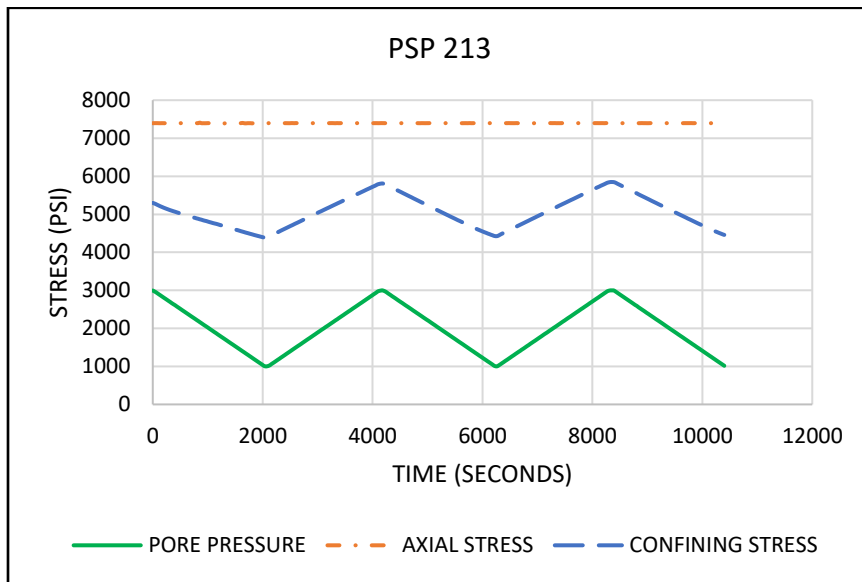


Figure 3-4 Application of pore pressure, axial stress and radial stress as a function of time. The axial stress is constant under the uniaxial strain boundary conditions. Test 1 constitutes depletion followed by injection. Multiple load-unload ramps have been performed.

For the second test of sample PSP 214, Figure 3-5 shows the stress path cycle is reversed. The sample starts with injection by increasing the pore pressure from about 3250 psi to 4500 psi. The response of the confining stress increases to keep the radial strain constant. After this first

injection, the pore pressure was then reduced or depleted to 3000 psi. One more injection and depletion cycle with same pore pressure magnitude was performed to study hysteresis effect in this stress path. The sample was then subjected to an additional depletion step to a final pressure of 1000 psi. This is an additional 2000 psi depletion not previously experienced by this sample.

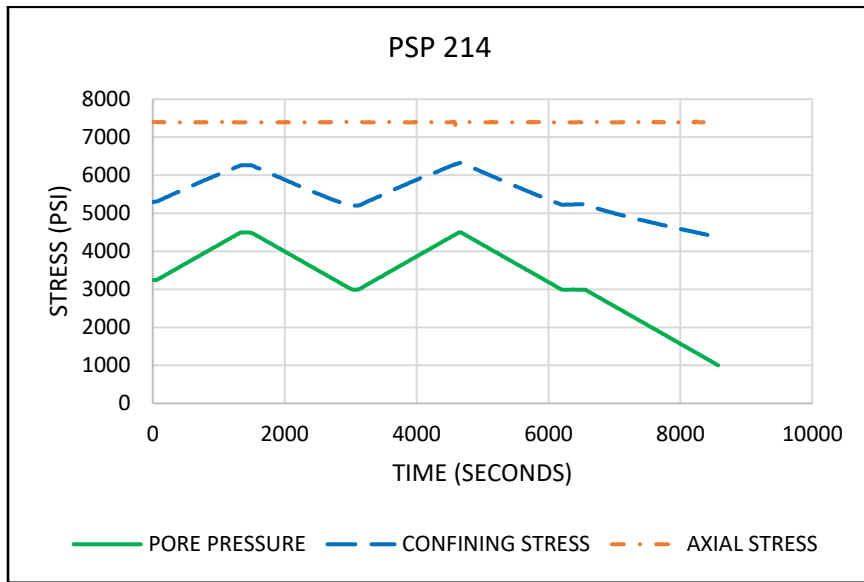


Figure 3-5 Application of pore pressure, axial stress and radial stress as a function of time. The axial stress is constant under the uniaxial strain boundary conditions. The sample is depleted to new pore pressure levels at last depletion.

For the third test of sample PSP 215, Figure 3-6 shows the magnitudes of the pore pressure depletion and injection were increased by 500 psi on each load and unload cycle. The objective is to compare the depletion and injection coefficient on repeat stress magnitudes that the sample had experienced before, and on new stress magnitudes that the sample had not experienced before. A total of five pore pressure depletion and four pore pressure injection ramps were performed in this test.

At the end of last injection ramp, the peak confining stress is close to the axial stress. Therefore, the boundary condition changes from uniaxial strain to isostatic. The consequence of the change in boundary condition will be addressed in section 3.2.3.

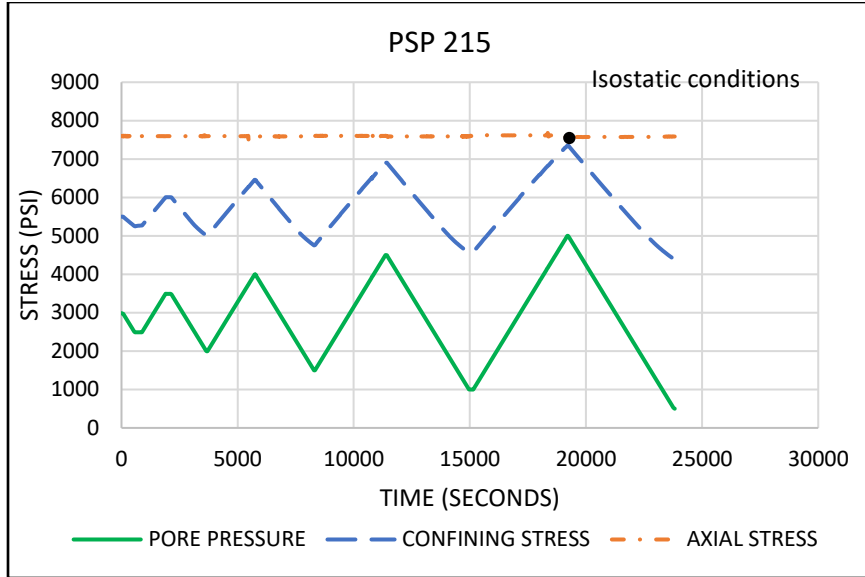


Figure 3-6 Application of pore pressure, axial stress and radial stress as a function of time. Test 3 constitutes depletion followed by injection with varying amplitudes. At the last injection, the boundary stresses change from uniaxial strain to isostatic conditions.

The changes in confining stress and pore pressure were recorded to be used in the calculation of the horizontal stress path coefficients (see Equation 3.3).

In this section we detailed the loading procedure to initial test conditions and described the three stress path coefficient measurement tests with respect to their loading procedure. In the next section, we will provide a detailed analysis of the data.

3.2 Data Analysis and Results

This section covers the data analysis of the three stress path coefficient measurement tests. The stress path coefficients are calculated as

$$\gamma_h = \frac{\Delta\sigma_c}{\Delta p_p}, \quad (3.4)$$

where γ_h is the stress path coefficient, $\Delta\sigma_c$ is the change in confining stress, and Δp_p is the change in pore pressure.

The stress path coefficient is equivalent to the slope of confining stress vs pore pressure.

Data analysis is presented sequentially starting with Test 1 – PSP 213, then Test 2 – PSP 214 and Test 3 – PSP 215. The initial point for each stress path ramp is labeled.

3.2.1 Test 1 – Depletion Followed by Injection

Figure 3-7 shows the variation in pore pressure with time as multiple depletion and injection ramps are performed. The end points of each ramp are labeled to help the data interpretation and explanation.

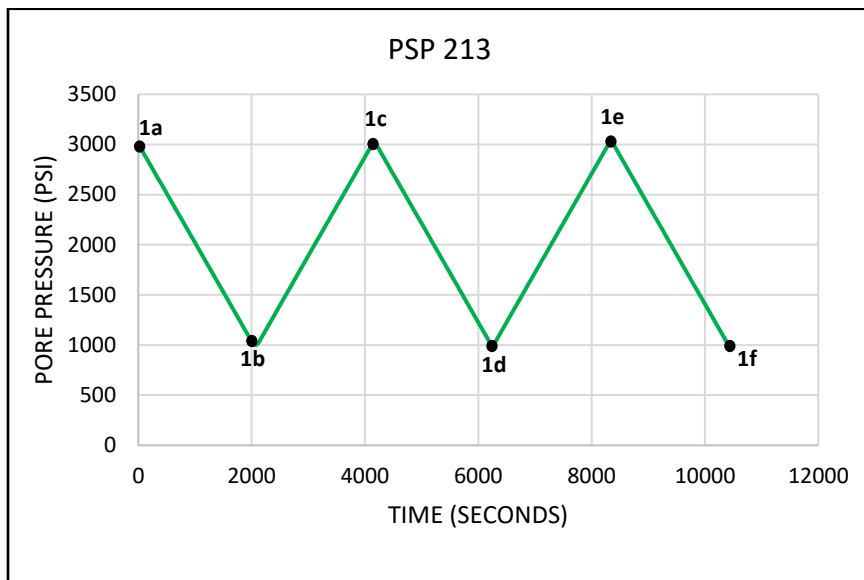


Figure 3-7 Shows pore pressure depletion and injection ramps for PSP 213. Three pore pressure depletion and two pore pressure injection ramps have been performed in test 1. Test 1 constitutes depletion followed by injection.

Figure 3-8 shows a plot of confining stress vs pore pressure for the first depletion (1a to 1b) and injection (1b to 1c) cycle. The slope or the horizontal stress path coefficient of the depletion ramp of 0.44 is lower than that of injection ramp of 0.70. On the first load-unload cycle,

the depletion and injection stress path coefficients are found to be different. The stress path coefficient of depletion is in fact lower than the injection coefficient.

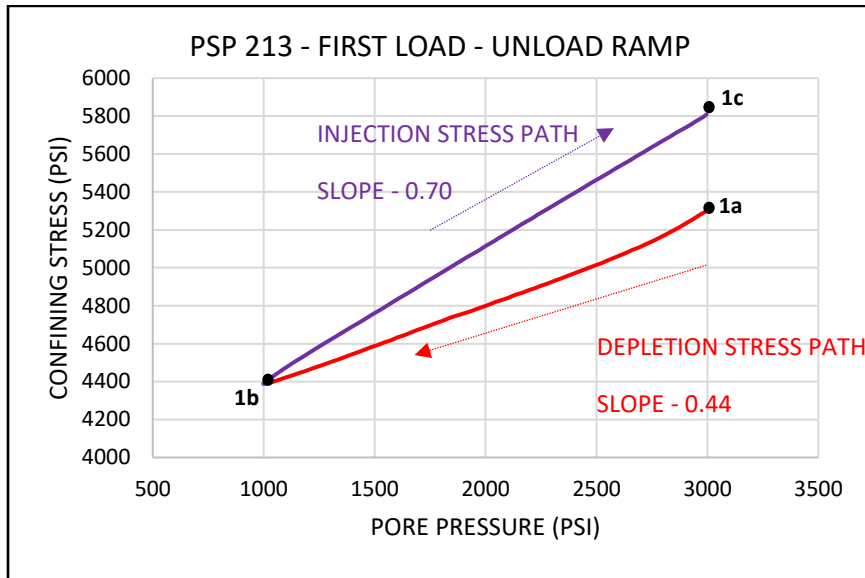


Figure 3-8 shows the initial depletion and injection ramps in a confining stress – pore pressure plot. The slope of the curve represents the horizontal stress path coefficient. The calculated depletion coefficient and injection coefficient for test 1 are shown.

Figure 3-9 shows the confining stress vs pore pressure plot of all remaining cycles (1c to 1f). The stress paths overlay each other. The depletion and injection coefficient values are equal (within error bars) to each other and to the coefficient value for the first injection stress path (1b to 1c). The depletion and injection coefficient values for all ramps are shown in Table 3-2. It is concluded from Table 3-2 that only the first depletion coefficient (path from 1a to 1b) is different than calculated coefficients from all subsequent load-unload ramps. For repeat stress paths after the first depletion ramp, the horizontal stress path coefficient remains the same for both depletion and injection ramps.

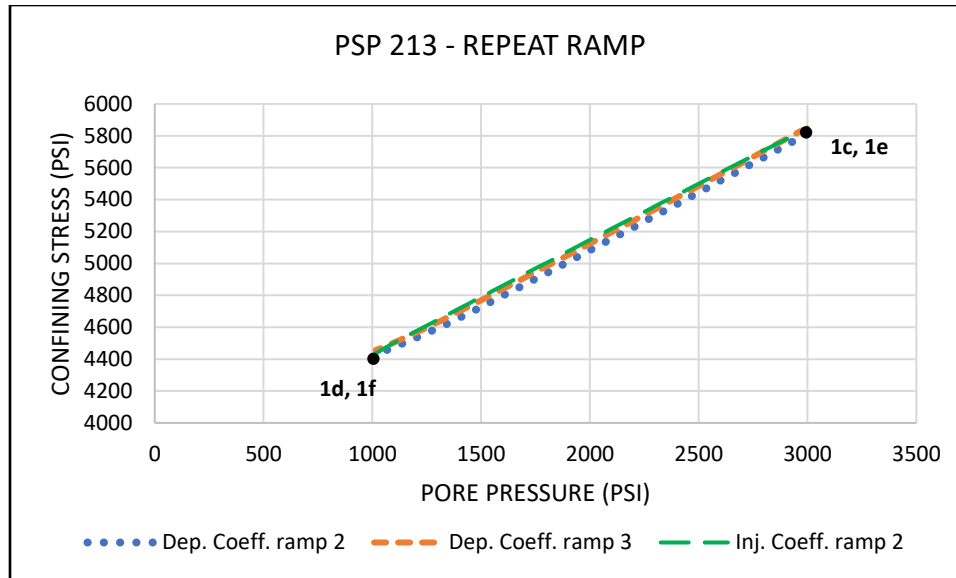


Figure 3-9 shows the plot of repeat depletion and injection ramps for test 1 - PSP 213. As can be seen, all ramps overlap each other with identical values of depletion and injection coefficients.

Table 3-2 Horizontal stress path coefficients calculated from depletion and injection cycles for Test 1. The stress path coefficient for Depletion 1 ramp is smaller than subsequent load-unload ramps.

STRESS PATH	CHANGE IN PORE PRESSURE (PSI)	CHANGE IN CONFINING STRESS (PSI)	STRESS PATH COEFFICIENT
DEPLETION 1 (1a – 1b)	-1996	-910	0.44
INJECTION 1 (1b-1c)	1997	1419	0.71
DEPLETION 2 (1c-1d)	-1996	-1384	0.70
INJECTION 2 (1d-1e)	1998	1424	0.71
DEPLETION 3 (1e-1f)	-1983	-1391	0.71

The response of the rock under unloading might be different than under loading. If the loading and unloading stress paths are different for the same magnitude of stress change, the observed effect is known as hysteresis (Fjaer et al., 2008). The amount of hysteresis can be calculated from the difference of the internal energy density (internal energy per unit volume) between sample under loading and unloading stress path. The internal energy density is obtained

by integrating the area under the strain-strain curve for a given stress path (Guo et. al., 2018). The internal energy is expressed as

$$\Delta U_i = \int_{\varepsilon_i}^{\varepsilon_f} \sigma d\varepsilon , \quad (3.5)$$

where ΔU_i is the change in internal energy density, ε_i is the initial volume strain, ε_f is the final volume strain, σ is the mean effective stress, and, $d\varepsilon$ is the instantaneous change in volume strain.

We used the mean effective stress (first effective stress invariant) and the volume strain (first strain invariant) to calculate the internal energy density and quantify the hysteresis. We used first stress and strain invariants to avoid directional dependence on the calculation of hysteresis energy. In our cylindrical test sample, the mean effective stress (p') is calculated from the axial stress (σ_a) and confining (σ_c) stress, and pore pressure (p_p) using the following equation

$$p' = \left(\frac{\sigma_a + 2\sigma_c}{3} \right) - p_p . \quad (3.6)$$

Figure 3-10 shows the volume strain response of the sample with respect to changing mean effective stress during depletion and injection stress paths. The end points of each stage can be inferred from the attached labels.

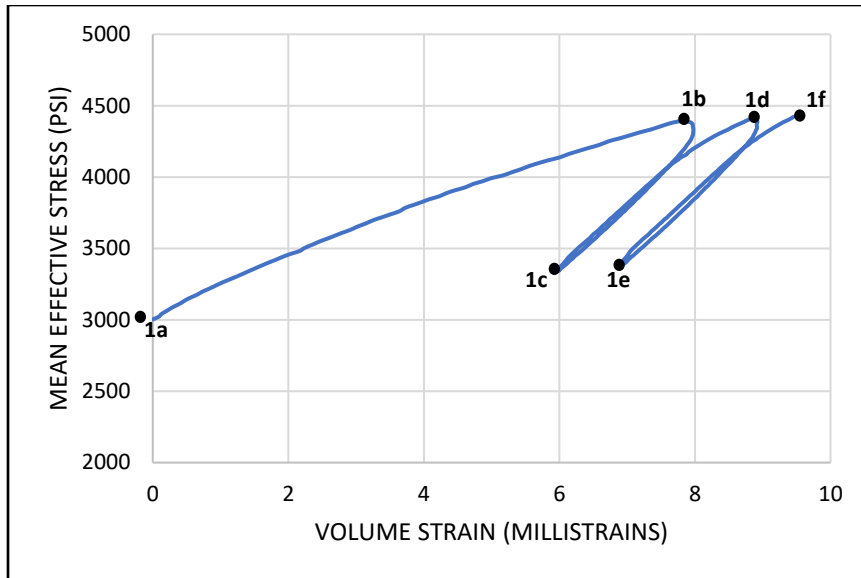


Figure 3-10 Shows volume strain behavior of the sample under changing mean effective stress during depletion and injection stress paths for test 1. The first load-unload ramp (1a-1c) has large amount of irrecoverable strains compared to subsequent ramps.

To compare each load-unload cycle against each other, we have initialized the mean effective stress and volume at the start of each load-unload cycle. Figure 3-11 and Figure 3-12 show the hysteresis loop of the load-unload cycle with change in mean effective stress versus volume strain for 1st and 2nd cycles respectively.

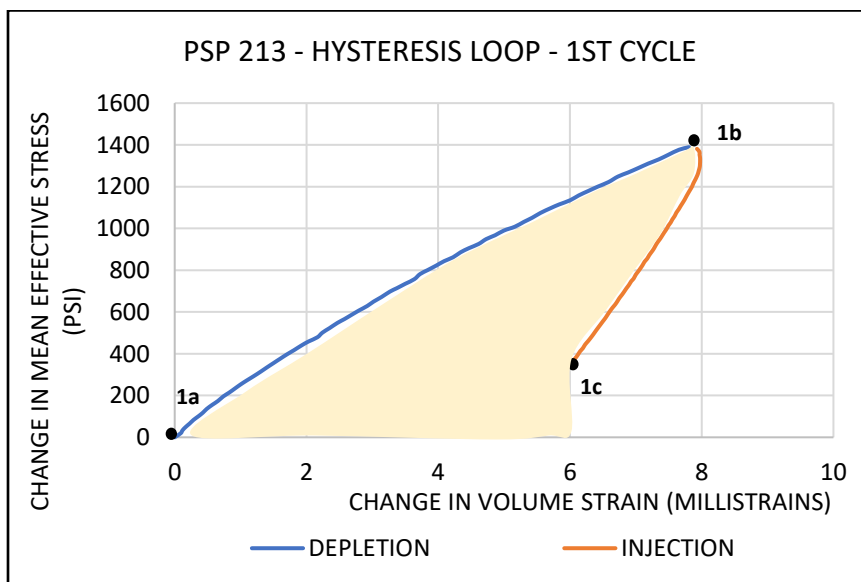


Figure 3-11 Shows the hysteresis in the first pore pressure depletion - injection cycle of PSP 213. Due to large amount of irrecoverable strain, the hysteresis energy dissipated during this cycle is high.

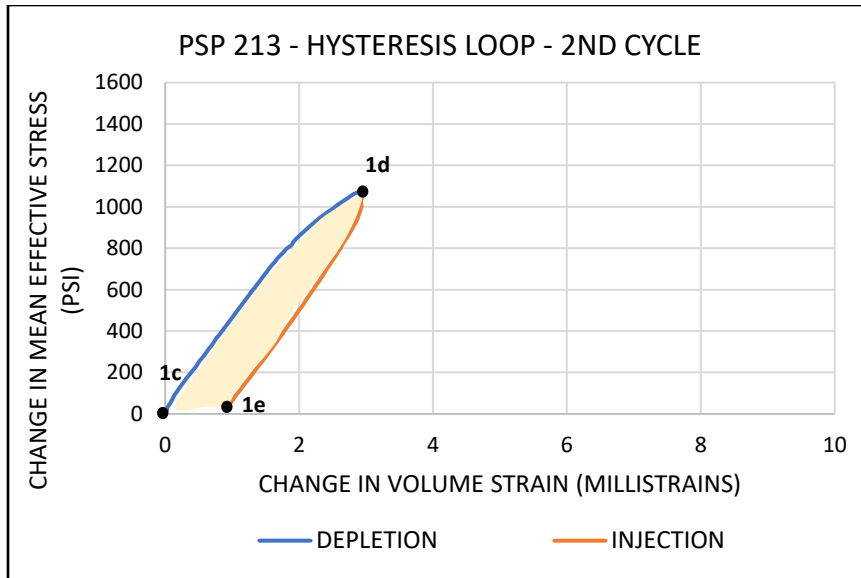


Figure 3-12 Shows the hysteresis in the second depletion - injection cycle of test 1 - PSP 213. Due to small amount of irrecoverable strain, the hysteresis energy dissipated during this cycle is low.

The calculated change in internal energy density normalized to the change in pore pressure of both load-unload cycles is presented in Table 3-3. As can be observed, the amount of hysteresis in the 1st cycle is more than 5 times larger than on the second cycle for same amount of pore pressure change. This highlights the imposed pressure change in the first depletion-injection or loading-unloading cycle was largely dissipated or not recovered. The implication and correlation of larger hysteresis with smaller stress path coefficient will be discussed in Section 3.3.

Table 3-3 Shows the amount of internal energy density change in each load-unload cycle for test 1 – PSP 213. The hysteresis energy dissipated in 1st cycle is about six times larger than the 2nd cycle.

Cycle	Ramp	Change in Internal energy Density (in. – lbf/in ³) per unit pore pressure ($\times 10^{-3}$)	Hysteresis Energy (in. – lbf/in ³) ($\times 10^{-3}$)
1	Depletion (1a-1b)	3.0	2.3
	Injection (1b-1c)	0.7	
2	Depletion (1d-1e)	0.9	0.4
	Injection (1e-1f)	0.5	

3.2.2 Test 2 – Injection Followed by Depletion

Starting with a load ramp cycle with depletion, Test 1 showed the first depletion stress path coefficient is lowest. The coefficients from subsequent injection and depletion ramps

remained constant when the depletion and injection pressure magnitude stay the same. In Test 2 – PSP 214, we want to assess the impact of starting the load ramp cycle with injection or unloading. We also want to determine how an additional depletion ramp with a lower pore pressure than prior ramp cycles have experienced would impact the stress path coefficient.

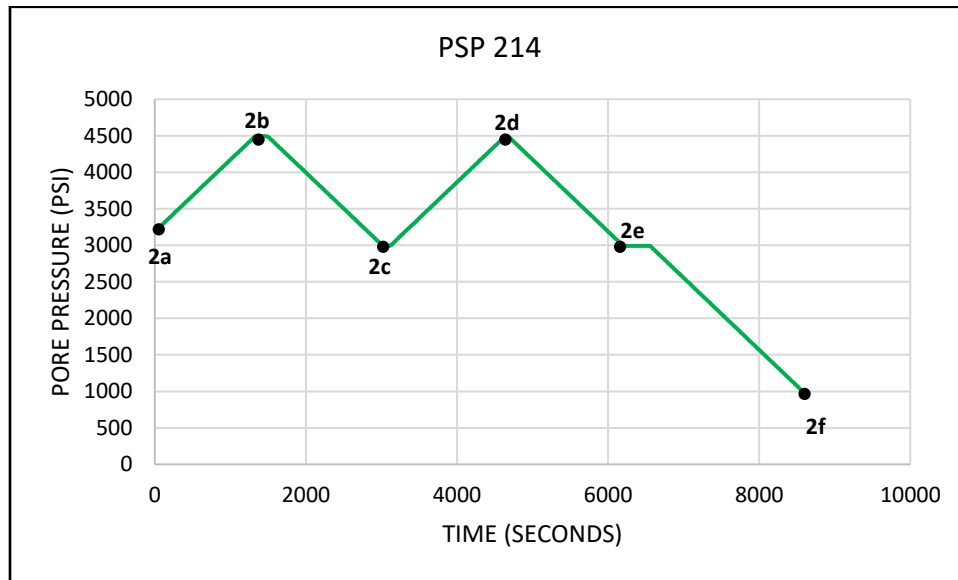


Figure 3-13 Shows pore pressure injection and depletion ramps for PSP 214. Three pore pressure depletion and two pore pressure injection ramps have been performed on PSP 214. Test 2 constitutes injection followed by depletion. The last depletion ramp takes sample to new depletion levels.

Figure 3-14 shows the confining stress versus pore pressure plot for the first injection – depletion cycle (2a-2c). The injection ramp (2b-2b) and depletion ramp (2b-2c) overlap each other. The slope of the injection and depletion ramp is 0.76 and 0.73, respectively. For this stress path, starting with injection and following with depletion, on the first unload-load cycle, the two stress path coefficients are found to be same. This observation is different than the first load-unload cycle of Test 1 – PSP 213. Therefore, these results highlight the starting stress path

direction has a significant effect on the values of stress path coefficients for similar changes in pore pressure magnitudes.

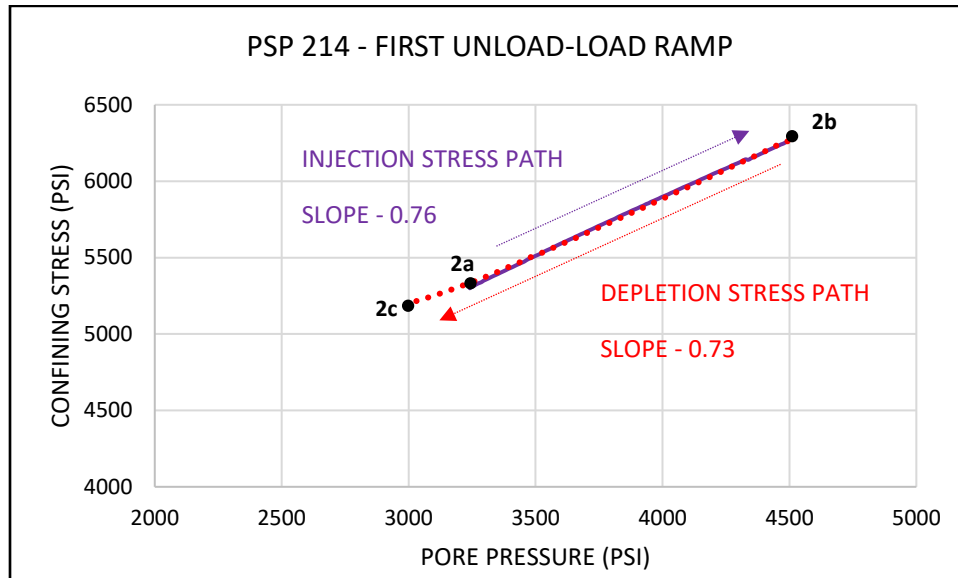


Figure 3-14 shows a plot of calculated depletion coefficient and injection coefficient for test 2 – PSP 214. The two initial depletion and injection stages are shown. Both the ramps overlay each other and the stress path coefficient value during injection and depletion are the similar.

Figure 3-15 shows the plot of remaining ramp cycles. For the second injection and depletion cycle (2c-2e), where the maximum and minimum pore pressure are the same as the first cycle, Ramps (2c-2d) and (2d-2e) overlay each other and with injection and depletion coefficient value of 0.75 and 0.74, respectively. These are comparable with values for the first cycle.

However, on the last depletion ramp (2e-2f) with pore pressure to 1000 psi and lower than previously experienced pressure value, the depletion stress path does not have the same slope as all previous ramps. The last depletion ramp (2e-2f) has a lower slope of 0.42. Coincidentally, this depletion coefficient value is similar to the first depletion ramp in test 1 (Figure

3-8). The depletion and injection coefficient values for all ramps for test 2 are summarized in Table 3-4.

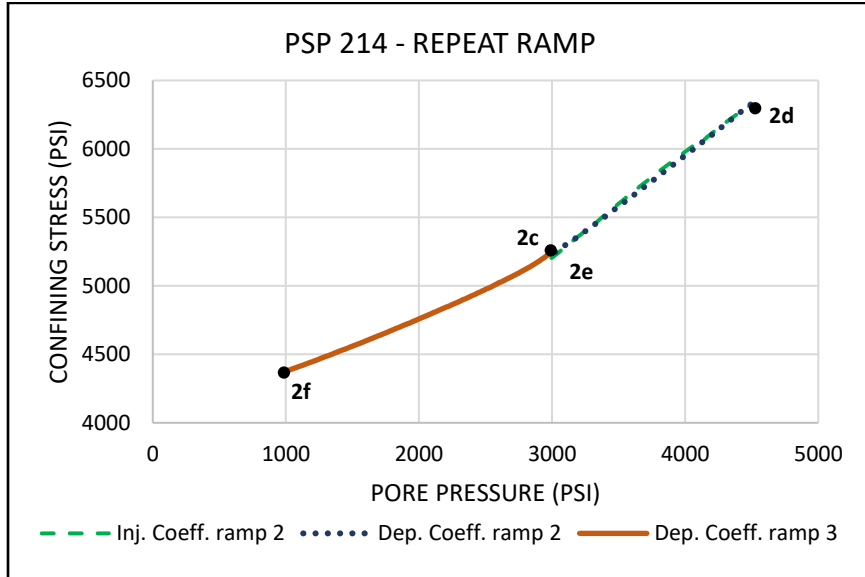


Figure 3-15 shows the plot of repeat depletion and injection ramps for test 2 - PSP 214. For ramp 2, depletion ramp and injection ramp overlap each other. However, depletion to new pore pressure levels (2e - 2f) has a smaller depletion coefficient.

Table 3-4 Horizontal stress path coefficients calculated from injection and depletion cycles for test 2 are presented. The stress path coefficient on last depletion ramp is markedly different than other ramps.

STRESS PATH	CHANGE IN PORE PRESSURE (PSI)	CHANGE IN RADIAL STRESS (PSI)	STRESS PATH COEFFICIENT
INJECTION 1 (2a-2b)	1253	963	0.76
DEPLETION 1 (2b-2c)	-1501	1066	0.73
INJECTION 2 (2c-2d)	1501	1126	0.75
DEPLETION 2 (2d-2e)	-1502	-1089	0.74
DEPLETION 3 (2e-2f)	-2001	-856	0.42

Figure 3-16 shows the volume strain response of the sample with respect to changing mean effective stress during injection and depletion stress paths. The different stress paths can be inferred from the attached labels.

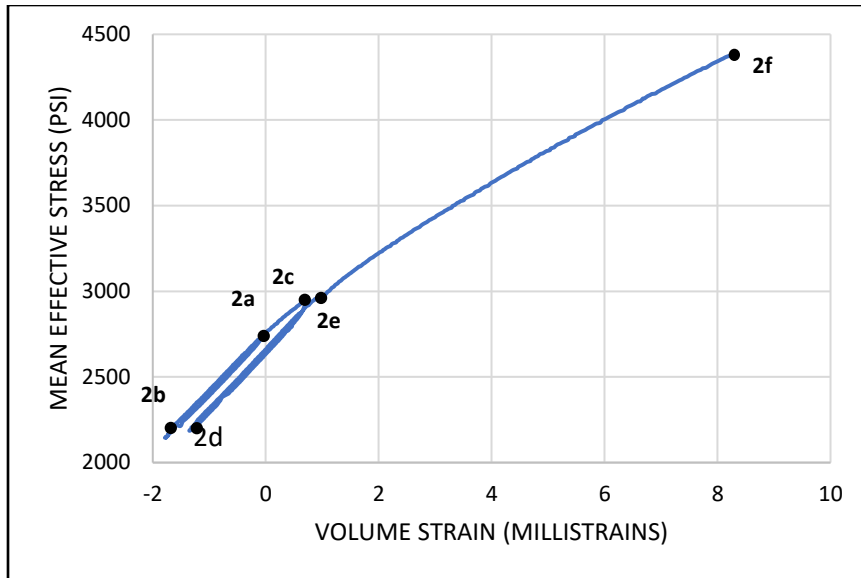


Figure 3-16 Shows the volume strain behavior of the sample under changing mean effective stress during depletion and injection stress paths for test 2. The last depletion ramp (2e - 2f) has larger amount of strain compared to other ramps.

Similar to test 1, Figure 3-17 and Figure 3-18 show the hysteresis loop of the unload-load cycle with change in mean effective stress versus volume strain. Both cycles show no significant hysteresis since the curves almost overlay each other and the loop is closed.

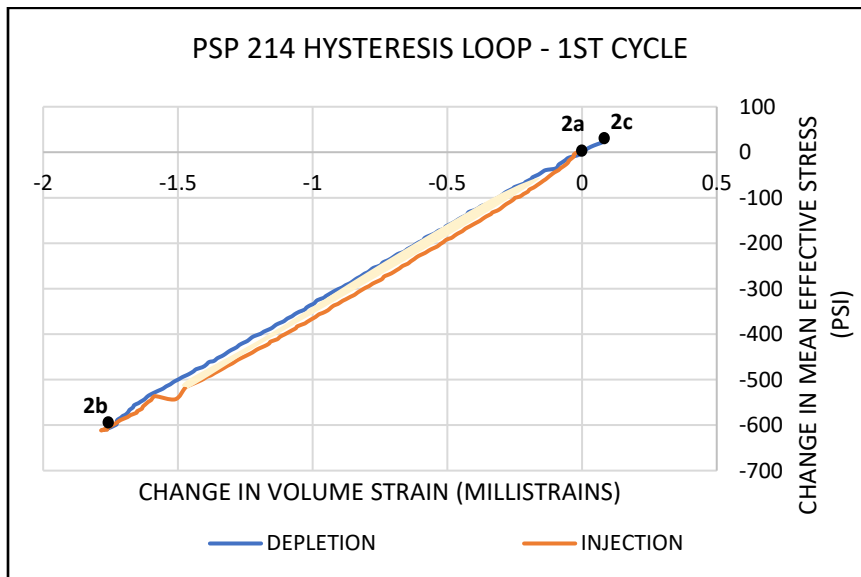


Figure 3-17 Shows the hysteresis in the 1st pore pressure injection - depletion cycle of test 2 – PSP 214. Both load-unload ramps overlay each other with minimal hysteresis energy in the 1st cycle.

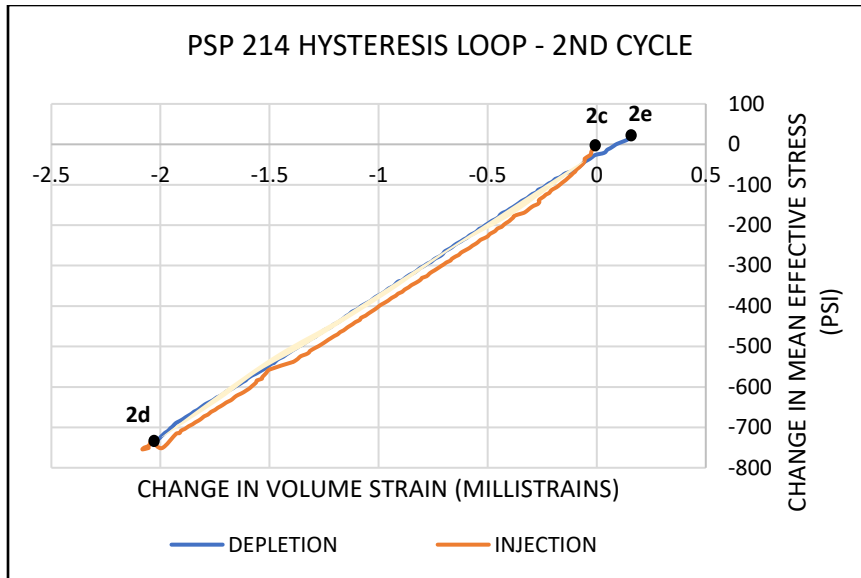


Figure 3-18 Shows the hysteresis in the 2nd injection - depletion cycle of test 2 - PSP 214. Both load-unload ramps overlay each other with minimal hysteresis energy in the 2nd cycle.

The calculated change in internal energy density normalized to the change in pore pressure of both unload-load cycles is presented in Table 3-5. As can be observed, the amount of hysteresis in both cycles of test 2 – PSP 214 are an order of magnitude lower than test 1 – PSP 213. Therefore, no significant amount of hysteresis is observed during the unload-load cycles of test 2 – PSP 214.

Table 3-5 Shows the amount of internal energy density change in each unload-load cycle for test 2 – PSP 214. Hysteresis energy is calculated as the difference of the change in internal energy density on load and unload cycle. No significant hysteresis is observed in both cycles.

Cycle	Ramp	Change in Internal energy Density (in. – lbf/in ³) per unit per pressure (x10 ⁻³)	Hysteresis Energy (in. – lbf/in ³) (x10 ⁻³)
1	Injection (2a-2b)	0.4	0.1
	Depletion (2b-2c)	0.3	
2	Injection (2c-2d)	0.4	0.0
	Depletion (2d-2e)	0.4	

However, the value of change in internal energy density for the last depletion ramp is 2.7×10^{-3} (in. – lbf/in²) which is order of magnitude higher than the other ramps. This value of change in internal energy density for a last depletion (new depletion level not experienced by the

sample) is comparable to change in internal energy value of 3.0×10^{-3} (in. – lbf/in²) that of the first depletion cycle (new depletion level not experienced by the sample) of test 1 – PSP 213. A comparison of change in mean effective stress versus change in volume strain plots is shown in Figure 3-19.

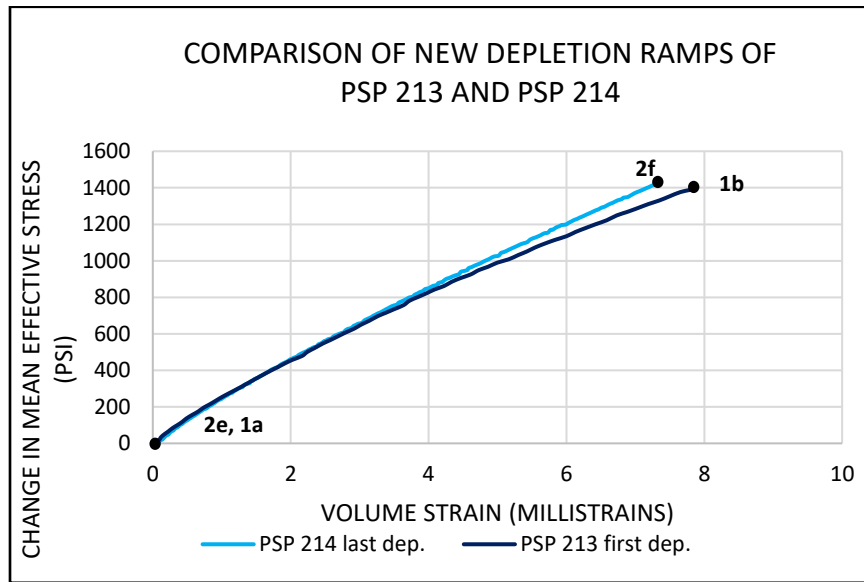


Figure 3-19 A comparison of change in mean effective stress vs change in volume strain plot of 1st depletion ramp of PSP 213 and last depletion ramp of PSP 214. Both ramps have similar amount of change in internal energy density which is evident from the overlapping stress- strain curves.

3.2.3 Test 3 – Increasing Amplitude Depletion – Injection Cycles

The stress path of test 3 – PSP 215 is similar to the above tests. We have added increasing amplitude of 500 psi to the load-unload ramps to understand the effects of multiple depletion and injection cycles. We will compare the repeat stress path ramps and the new (increased amplitude) stress path ramps to understand the material behavior.

The stress path of test 3 – PSP 215 (Figure 3-20) starts with depletion ramp (500 psi of depletion) from point 3a to 3b. This is the initial depletion ramp. From 3b, an injection stress path of repeat stress amplitude is followed from 3b to 3c. At 3c, a new injection stress path (500 psi of additional injection) is followed until 3d. We begin reducing pore pressure again on repeat depletion ramp (from 3d to 3e) and then additional new depletion of 500 psi (from 3e to 3f).

In summary, the test can be separated into two types of ramps:

- Repeat ramps of either depletion or injection –
 - 3b-3c, 3d-3e, 3f-3g, 3h-3i, 3j-3k, 3l-3m, 3n-3o, and 3p-3q.
- New ramps (increasing amplitude of 500 psi) of either depletion or injection –
 - 3a-3b, 3c-3d, 3e-3f, 3g-3h, 3i-3j, 3k-3l, 3m-3n, 3o-3p, and 3q-3r.

The orange dashed lines show the separation of repeat ramps and new ramps on both depletion and injection stress paths. We present the data in the form of these two types of ramps to compare the material response under new stress paths and repeat stress paths.

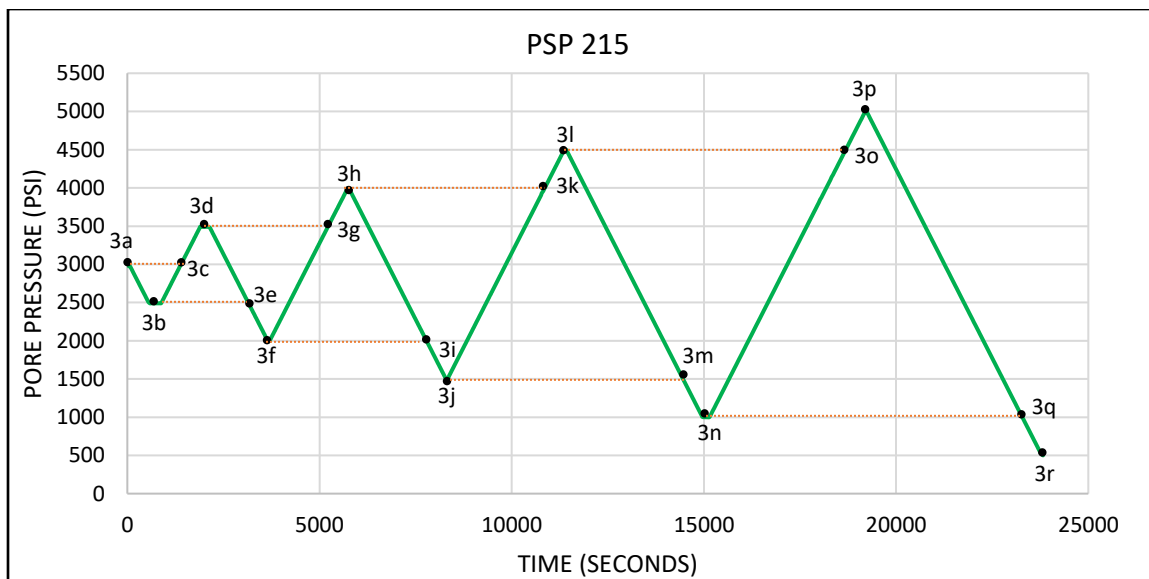


Figure 3-20 Application of pore pressure, axial stress and radial stress as a function of time. Test 3 constitutes depletion followed by injection with varying amplitudes to show impact of changing depletion and injection levels.

Figure 3-21 shows a plot of the first injection – depletion cycle for test 2 – PSP 215. The depletion coefficient (0.51) is lower than the injection coefficient (0.73) similar to the 1st depletion injection cycle for test 1. The injection coefficient value on the new stress path is also same as the

injection coefficient value at the repeat stress path. We infer from this observation that for new injection stress paths, the injection coefficient does not change.

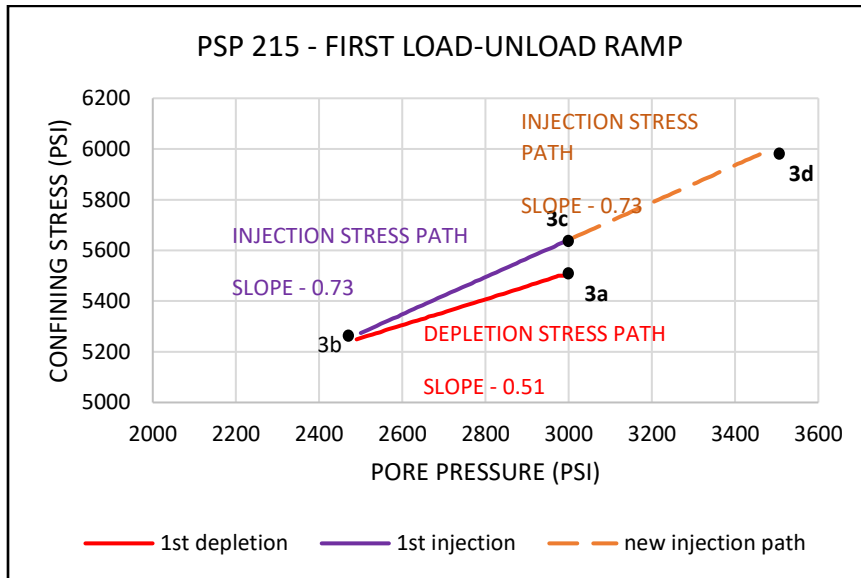


Figure 3-21 shows a plot of calculated depletion coefficient and injection coefficient for test 3 – PSP 215. The initial depletion coefficient is small. The incremental injection stress path coefficient is same as the repeat injection coefficient.

To simplify data representation, we have separated the depletion and injection ramps into two cases – one for repeat stress paths and the other for new incremental stress paths.

For repeat depletion stress paths, the summary plot of repeat depletion stress paths is shown in Figure 3-22. The slope of depletion stress paths i.e., the depletion coefficient values are reported in Table 3-6. For all repeat ramps, the depletion coefficient values are similar and have a mean value of 0.73. For the injection stress paths, the summary plot is shown in Figure 3-23. Table 3-6 reports injection coefficient values for all repeat ramps. The injection coefficient values for all repeat ramps also have a mean value of 0.73 which is similar to the mean depletion coefficient value.

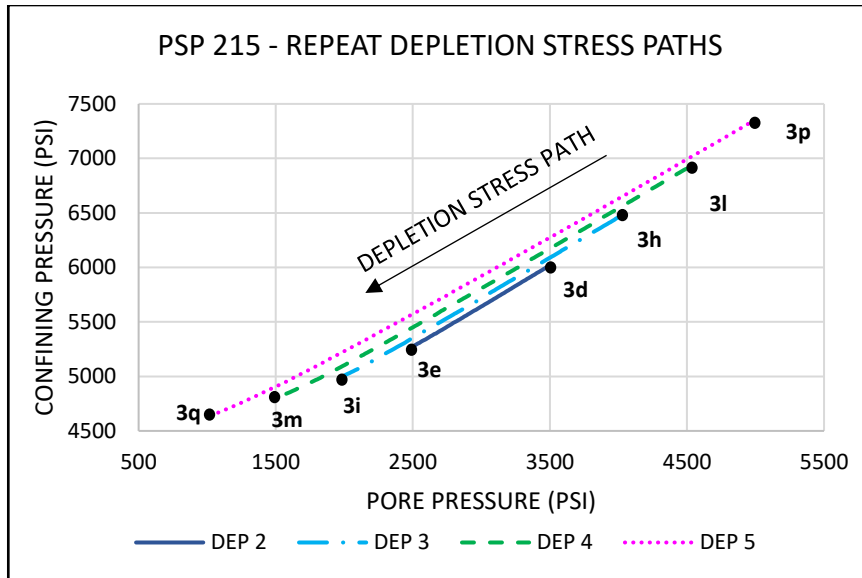


Figure 3-22 A summary plot of repeat stress paths of depletion for PSP 215. The beginning and end of the ramps are labeled. All the repeat ramps have similar slopes with mean value of 0.73.

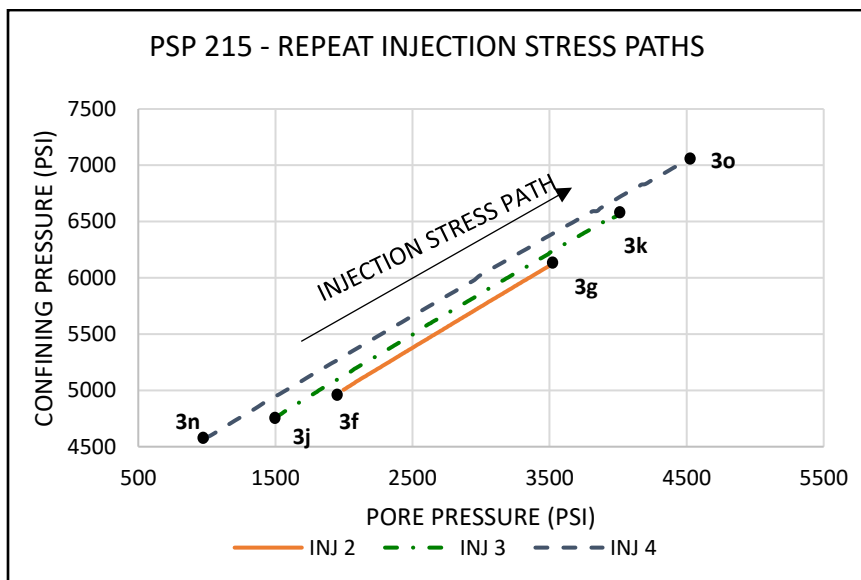


Figure 3-23 A summary plot of repeat stress paths of injection for PSP 215. The beginning and end of the ramps are labeled. All the repeat ramps have similar slopes with mean value of 0.73.

For new depletion stress paths, a summary plot is shown in Figure 3-24. Table 3-6 summarizes the depletion coefficient values for new depletion stress paths with a mean value of 0.5. This is lower than the mean value of 0.73 for the repeat depletion stress paths. For new injection stress paths, a summary plot is shown in Figure 3-25. Table 3-6 summarizes the injection coefficient values for new injection stress paths with a mean value of 0.7. with the exception of

the 4th new injection stress path (4o-4p). In this 4th new injection stress path, the confining stress value approaches the axial stress values towards the end of the ramp (Figure 3-6). Therefore, the sample is approaching an isostatic stress conditions (i.e., axial stress, and confining stresses are the same) during the pore pressure injection with uniaxial strain conditions. Since, the boundary conditions for last injection ramp is different compared to the other new injection ramps, the injection coefficient is expected to be different. The inferences from above summary plots complement the inferences obtained from Figure 3-8 and Figure 3-15.

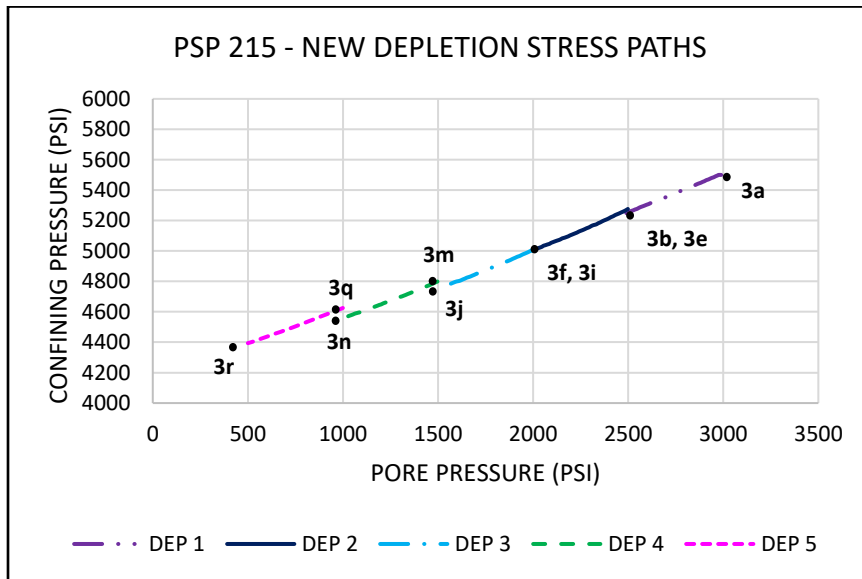


Figure 3-24 Shows a summary plot of new depletion stress paths for PSP 215. The beginning and end of each ramp are labeled. The depletion coefficient from new depletion stress paths is lower than repeat depletion stress paths.

Table 3-6 **Error! Reference source not found.** summarizes the depletion coefficient and injection coefficient values for the new incremental stress path ramps and repeat stress path ramps in both loading (depletion) and unloading directions (injection). Inferences from this test reinforce the results from test 1 and 2. During repeat stress paths of either depletion or injection, the stress path coefficients are equal to 0.73 ± 0.02 (within error bars). For new injection stress path, the injection coefficients are also equal to the repeat ramp stress path coefficients (within error bars) except for 4th injection stress path. The boundary conditions for last injection ramp are

isostatic (Figure 3-6). Therefore, the injection coefficient is different compared to other injection ramps. When the sample undergoes new incremental depletion to a pore pressure level it has not experienced before, the depletion coefficient falls to a range of 0.48 ± 0.05 .

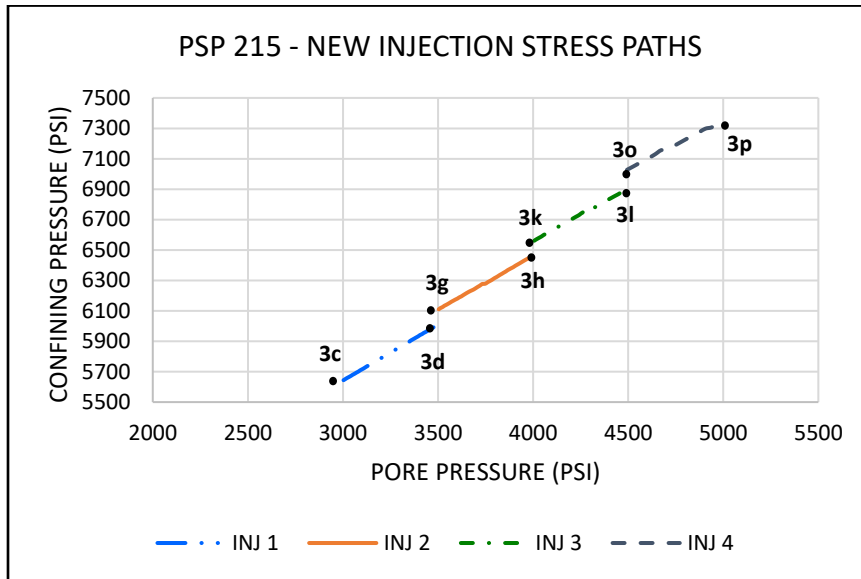


Figure 3-25 Shows a summary plot of new injection stress paths for PSP 215. The beginning and end of each ramp are labeled. The injection coefficient from new injection stress paths is similar to the repeat injection stress paths except for the injection 4 stress path.

Table 3-6 Shows the stress path coefficient values for the repeat stress path depletion and injection ramps as well as the new incremental stress path ramps. During new incremental depletion ramps the depletion coefficient is smaller whereas injection coefficient is similar.

RAMP	STRESS PATH REPEAT RAMP COEFFICIENT	STRESS PATH NEW RAMP COEFFICIENT
DEPLETION 1	----	0.51
INJECTION 1	0.73	0.73
DEPLETION 2	0.75	0.53
INJECTION 2	0.73	0.70
DEPLETION 3	0.73	0.51
INJECTION 3	0.72	0.68
DEPLETION 4	0.71	0.48
INJECTION 4	0.71	0.63
DEPLETION 5	0.70	0.47

Figure 3-26 shows the volume strain response of the sample with respect to changing mean effective stress during injection and depletion stress paths. The different stress paths can

be inferred from the attached labels. As can be seen, for each new depletion stress path ramp, an associated value of plastic strain is observed upon unload via injection (some residual volume strain is seen at the end of injection cycles). The repeat depletion and injection ramps almost overlay each other.

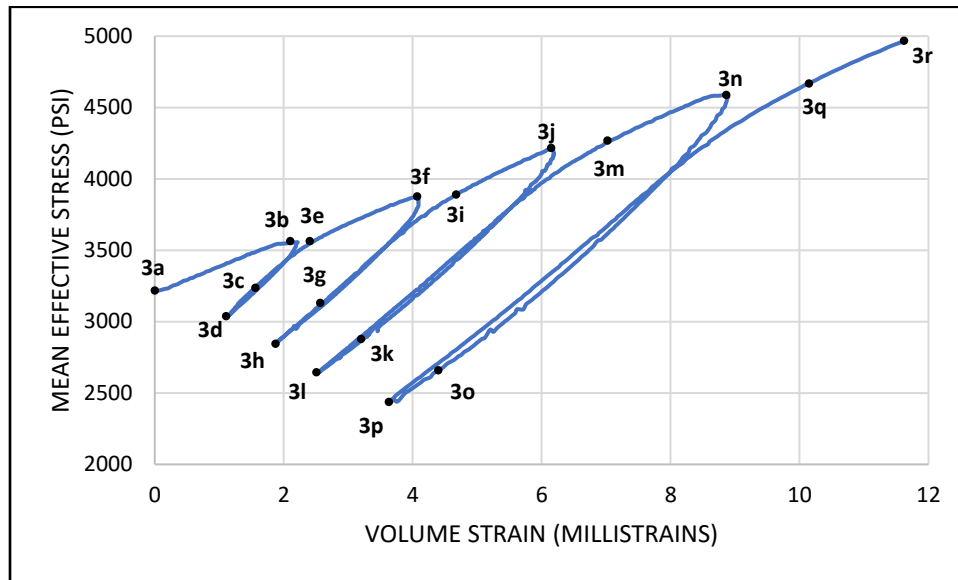


Figure 3-26 Shows a summary volume strain plot of PSP 215 under changing mean effective stress during depletion and injection stress paths. The beginning and end points of stress ramps are labeled.

To calculate hysteresis for each new load-unload ramp (Figure 3-27), we have initialized the value of mean effective stress and volume strain at the start of each depletion ramp and closed the load-unload cycle at the end of repeat injection stress path. This method ensures a close load-unload hysteresis loop and we compare the accumulation of hysteresis when the initial pore pressure value (at the start of new depletion) is the same as the final pore pressure value (at the end of repeat injection).

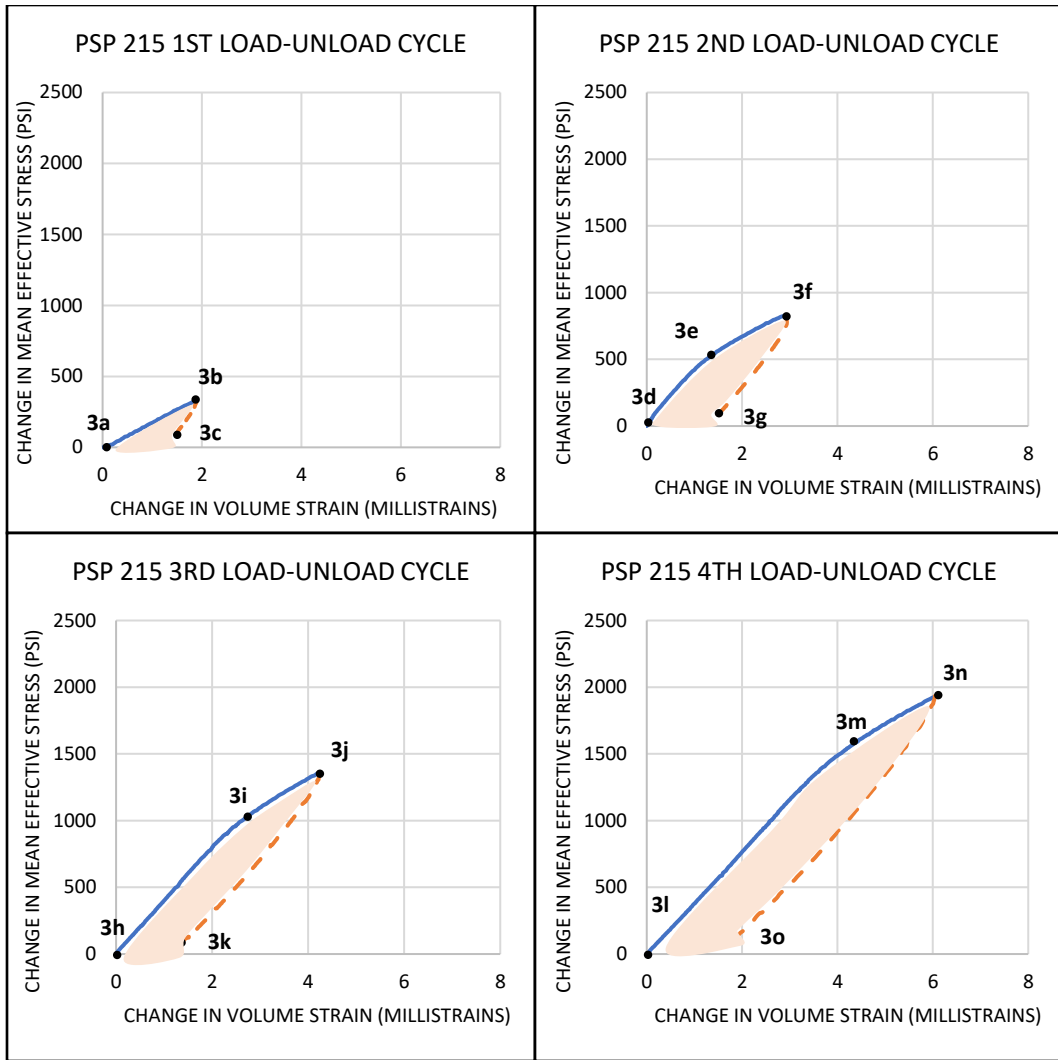


Figure 3-27 Shows the load-unload cycle for calculation of hysteresis energy. The figures show a cumulative load-unload cycle consisting of both repeat depletion and new depletion ramps.

The Hysteresis energy per unit pore pressure is calculated using the same procedure used for PSP 213 and PSP 214. An increasing trend in values of hysteresis energy per unit pore pressure is seen with successive load-unload cycle (Table 3-7). In the next section, we will discuss MCC modelling and movement of yield surface for explaining the behavior of lower depletion coefficient value for new depletion stress paths.

Table 3-7 Show the calculation of hysteresis energy per unit pore pressure for PSP 215. The hysteresis energy is marginally increasing with each successive load-unload ramp.

Cycle	Ramp	Change in Internal energy Density (in. – lbf/in ³) per unit pore pressure (x10 ⁻³)	Hysteresis Energy (in. – lbf/in ³) (x10 ⁻³)
1	Depletion	0.6	0.4
	Injection	0.2	
2	Depletion	0.9	0.6
	Injection	0.3	
3	Depletion	1.3	0.6
	Injection	0.7	
4	Depletion	1.8	0.7
	Injection	1.1	

3.3 Modelling and Discussions

In the previous section, we talked about the three pore pressure tests and discussed their results. The major inferences are:

1. During the first depletion stress path to low pore pressure levels not experienced by the sample, the depletion stress path coefficient is low, $\sim 0.5 \pm 0.1$.
2. During reload depletion stress path to pore pressure levels experienced by the sample previously, the depletion stress path coefficient is high, $\sim 0.7 \pm 0.05$.
3. During the first injection stress path to high pore pressure levels not experienced by the sample, the injection stress path coefficient is high, $\sim 0.7 \pm 0.05$.
4. During reload injection stress path to pore pressure levels experienced by the sample previously, the injection stress path coefficient is high, $\sim 0.7 \pm 0.05$.

We observed that the stress path coefficient is low 0.5 ± 0.1 , only for the case of new incremental depletion levels that the sample has not experienced before. For all other cases, the stress path coefficient is $\sim 0.7 \pm 0.05$ whether it is on depletion stress path or injection stress path. This behavior is explained by following the yield surface during the both depletion and injection stress path.

The Modified Cam Clay (MCC) model (Roscoe et al., 1968) is used as the constitutive material model to fit the experimental data. To recap the loading procedure - is first pre-consolidated isostatically to a mean effective stress of 4050 psi (Figure 2-11); then the sample is loaded to its initial stress condition through an isostatic stress path and then followed with a triaxial stress path (Figure 3-3). A MCC model is fit to this loading triaxial stress path to determine the yield surface or at the start of the pore pressure depletion-injection tests with the uniaxial strain boundary conditions. Figure 3-28 shows the yield surface of the pre-consolidated step by the calibrated MCC model and depicts the triaxial stress path in bringing the sample to its initial stress conditions (point 1a). Table 3-8 summarizes the MCC model parameter values used after matching with strain data of the experiment. Figure 3-29 shows the quality of the match between strain data and MCC model's predictions.

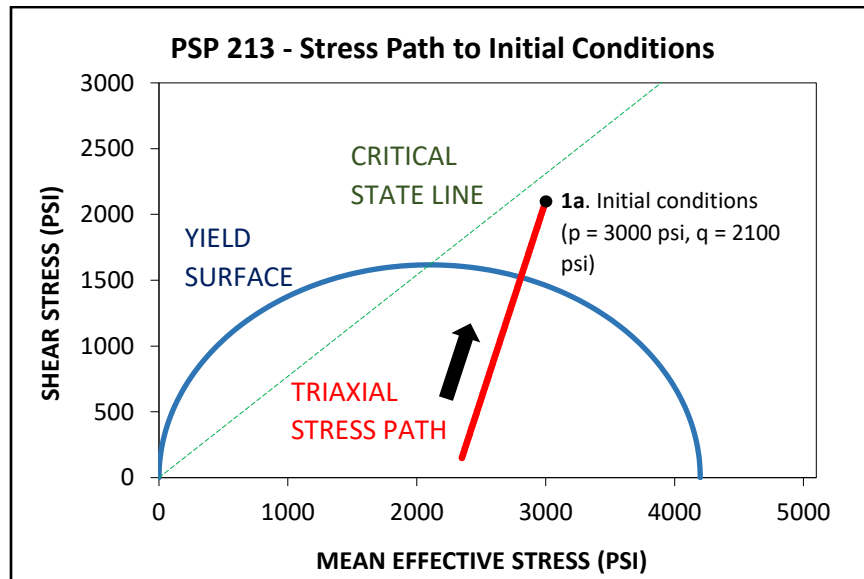


Figure 3-28 Shows the calibrated MCC model for triaxial stress path ramp of PSP 213. The yield surface is shown in blue; the critical state line is shown in green and the triaxial stress path is shown in red.

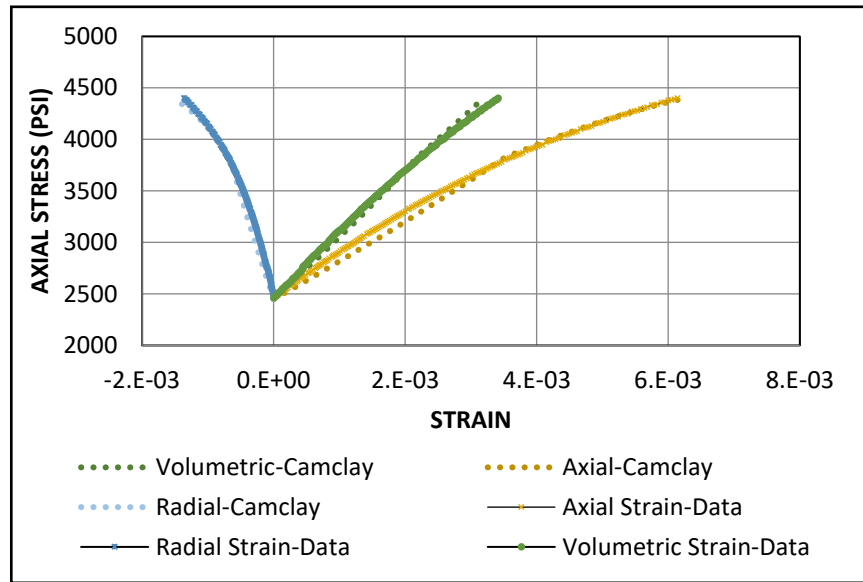


Figure 3-29 Shows the simulated strain data and experimental strain data plotted together. There is a good match between the two data sets indicating a good model fit.

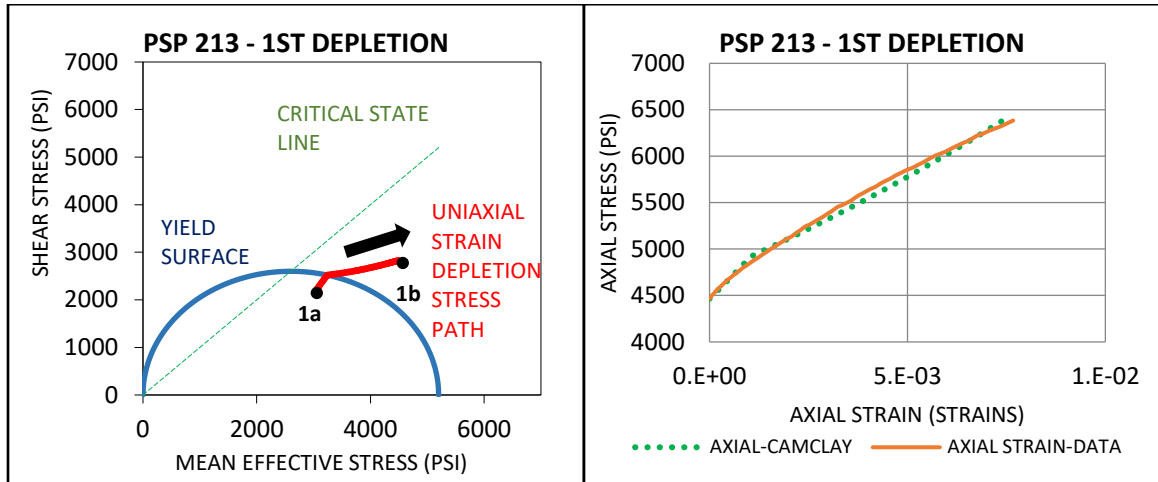
The next phase of modeling involves tracking the yield surface on depletion and injection stress paths. The MCC model parameters are shown in Table 3-8.

Table 3-8 Shows the cam clay parameters used to fit the experimental data for the triaxial stress path and the uniaxial strain paths.

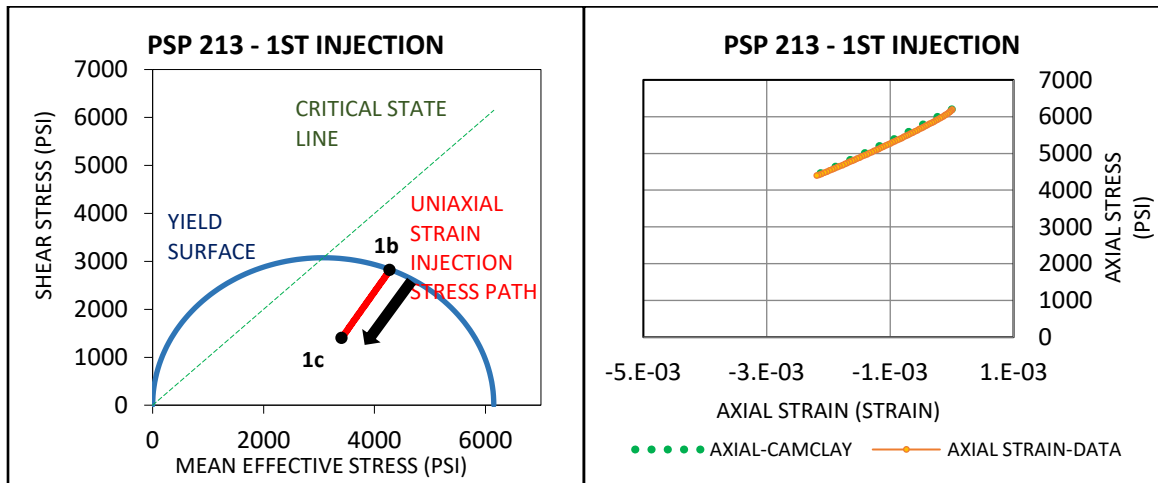
MCC Model Parameters						
Stress path	Lambda	Kappa	M	Pre-consolidation Stress (psi)	Porosity	Poisson's Ratio
Triaxial	0.017	0.016	0.77	4200	0.25	0.19
1 st Depletion	0.028	0.019	1.0	5200	0.21	0.18
1 st Injection	0.028	0.012	1.0	6150	0.19	0.18
2 nd Depletion	0.028	0.019	1.0	6150	0.20	0.18

Figure 3-30 shows the MCC model simulated yield surface for 1st depletion (1a – 1b), 1st injection (1b – 1c) and 2nd depletion (1c – 1d) of Test 1 or PSP 213. Each figure includes the stress paths taken by the sample, the yield surface position at the beginning of the test, and the critical state line shown on the mean effective stress vs shear stress plots on the left. The simulated axial strain data by MCC model and the measured axial strain data vs axial stress are plotted against each other on the right side to illustrate the quality of MCC model predictions. Since the test

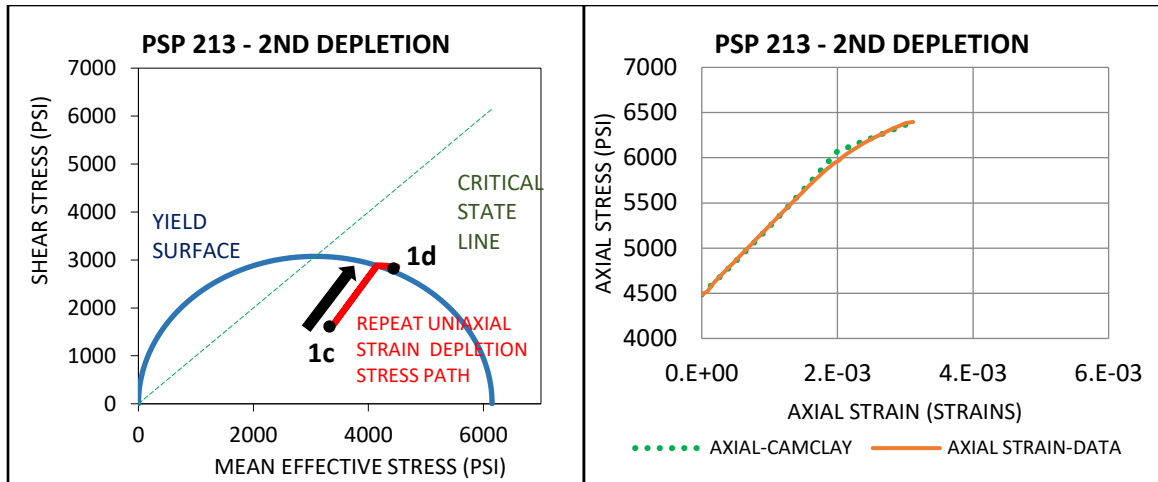
boundary condition is uniaxial strain, the radial strain is constant or change in radial strain is zero. Hence, volume strain is proportional or equal to the axial strain. This is the reason why we use the axial strain to model experimental data.



(A)



(B)



(C)

Figure 3-30 Shows the MCC model fits for the 1st Depletion (A), 1st Injection (B) and 2nd Depletion stress path. A simulated yield surface with its critical state line and the stress path taken by the sample and with experimental axial strain data recorded from the lab measurements are plotted.

The MCC model fit for PSP 214 is presented in appendix II. It shows the last depletion ramp has expanded the yield surface.

At the end of triaxial stress path when the sample has reached initial conditions, it has an initial porosity. The triaxial stress path expands the previous yield surface created during the pre-consolidation and the sample remembers the triaxial stress path and stress magnitude. This effect is referred to as stress memory effect or Kaiser effect (Kaiser, 1953). During new uniaxial strain depletion stress path, the sample has not experienced these stresses magnitudes under uniaxial strain boundary conditions before. Therefore, the sample yields in the new depletion stress path and the yield surface expands accompanied by plastic strains. Therefore, the new depletion coefficient value is low. During repeat depletion or injection stress paths within same pore pressure magnitudes, the sample remembers the stress magnitudes and the stress path. The final stress magnitude and the stress path during repeat depletion or injection is inside the previously expanded yield surface. Therefore, the sample behaves elastically with minimal plastic strain and the observed horizontal stress path coefficient for depletion and injection are high. Whenever the stress path or stress magnitude expand the yield surface, the sample deforms with plastic strains

and the depletion coefficient is low. For all other stress paths and stress magnitudes, the sample behaves elastically, and the horizontal stress path coefficient is high.

The above observation can be explained by following the behavior of the sample during initial depletion compared to repeat depletion/injection.

For each ramp in the uniaxial strain boundary conditions, we observe the sample response in the axial direction and the radial direction separately. In the axial direction, the sample can change dimensions under the uniaxial strain boundary conditions. The energy dissipated during this process is represented as:

$$dU = q * d\varepsilon_a, \quad (3.7)$$

where dU is the dissipated or hysteresis energy, q is the shear stress, and $d\varepsilon_a$ is the axial strain. In the radial direction, the boundary conditions dictate that the radial dimensions remain constant. Due to changing shear stress induced by changing pore pressure along the vertical direction, a corresponding horizontal or confining stress reaction is created due to Poisson's deformation effect. This resulted in a change in confining stress to maintain the constant radial strain boundary condition.

During the first or new depletion, the sample has not experienced before the stress path of uniaxial strain or the increased stress magnitudes of mean effective stress and shear stress. The sample compacts (deforms axially) and reduces porosity by reorienting grains and increasing grain contacts. The process generates irrecoverable strains and dissipates high amount of energy in the material (Figure 3-31). Therefore, there is less energy available to deform the sample in the radial direction or have smaller confining stress responses due to change in pore pressure. This helps explain the smaller depletion stress path coefficient measured when the sample experiences a new depletion stress level.

For repeat pore pressure injection - depletion ramps within same pore-pressure intervals, the sample has a stress memory of the 'uniaxial strain' stress path and the previous stress magnitudes of mean effective stress and shear stress due to Kaiser effect. As the sample porosity has already been reduced and the sample is stiffer (Figure 3-31), there is less energy dissipation due to axial deformation and the process is mostly elastic. Test results confirmed the hysteresis measured for such reload-unload ramps were nearly six times smaller than hysteresis for new depletion ramps. With more elastic energy available to axially deform the sample, there is correspondingly more Poisson's induced radial deformation. This induces a higher confining stress to maintain the constant radial strain boundary conditions. Hence, values of depletion coefficient/injection stress path coefficient on repeat ramps is high. When the sample is exposed to higher depletion stresses the first or the new depletion process is repeated.

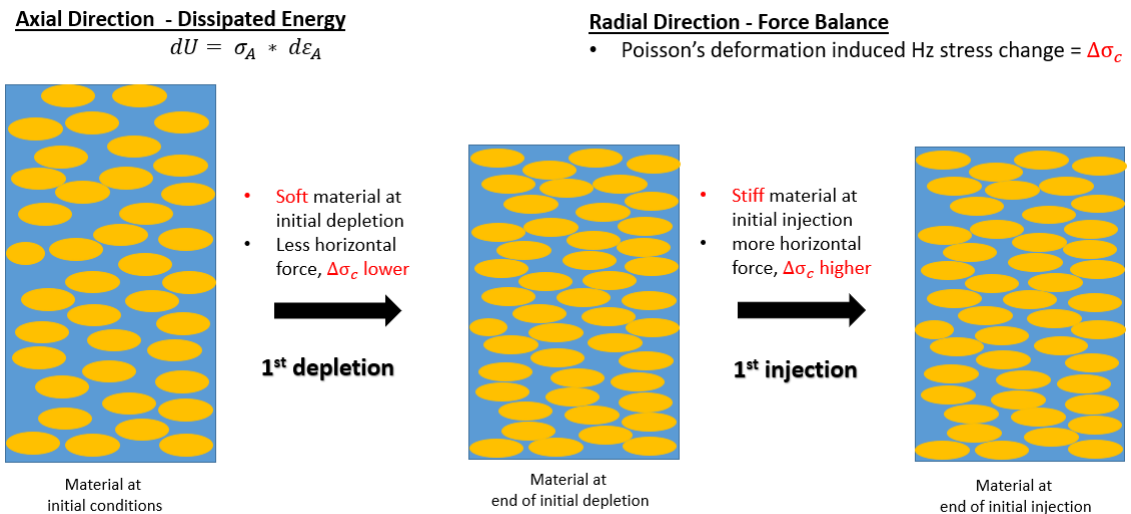


Figure 3-31 Shows a schematic of the matrix and grains. During initial depletion, sample compacts in axial direction and irrecoverable strains occur with dissipation of energy. On initial injection, the sample response is elastic with no irrecoverable strain and associated dissipation of energy.

3.4 Conclusions

The geo-mechanical behavior of unconsolidated sands samples under uniaxial strain boundary conditions were studied to compare the horizontal stress path coefficients under depletion and injection. A consistent sample preparation technique has been described in detail

to prepare uniform and repeatable sand pack specimen. Three pore pressure uniaxial strain tests were conducted to obtain the depletion stress path coefficient and injection stress path coefficients. Hysteresis in loading – unloading stress cycle were studied and quantified. Expansion of MCC yield surface, and the physical mechanism of loss of porosity, grain reorientation and Poisson's deformation induced horizontal force balance were used to explain the low value of initial depletion coefficient compared to the repeat depletion / injection coefficients.

In the next chapter we will discuss the effect of injection and stress path directions on yielding behavior of unconsolidated sands.

4. YIELD SURFACE AND STRESS PATH DIRECTIONS

In the previous section we evaluated stress path coefficient under different loading and unloading conditions to assess the effect of depletion and injection in changing horizontal in-situ stress in unconsolidated sands. In this section, we will address the other half of the problem, that is, to investigate the effects of stress magnitudes and stress path directions on the yielding behavior of unconsolidated sands. The focus is on high mean effective stress ranges representative of depleted reservoir in deep water.

For geo-materials, such as unconsolidated sands, laboratory yield stress results are presented in the mean effective stress (p') and shear stress (q) space (Lade et al., 1976). Equations (4.1) and (4.2) define q and p' in terms of axial stress (σ_1) and radial or confining stress (σ_3) of the experiment.

$$q = (\sigma_1 - \sigma_3) \quad (4.1)$$

and

$$p' = \left(\frac{\sigma_1 + 2\sigma_3}{3} \right) . \quad (4.2)$$

Yield stress responses of unconsolidated sand are known to depend on (a) the stress path taken by the sample to reach at the initial stress point in the p' and q plot, (b) the stress magnitudes or p' and q values of this initial stress point, and (c) the stress path direction to be taken by the sample to reach at the yield stress point (Arya, 2018; Dessouki et al., 2020). The stress path direction traveling from a given stress point to another stress point (e.g., from the initial stress point to the yield stress point) can be defined by the relative change in q with the corresponding change in p' or simply the ratio of Δq over $\Delta p'$. Another option is to use the stress path angle (θ) defined as :

$$\theta = \tan^{-1}\left(\frac{\Delta q}{\Delta p'}\right) . \quad (4.3)$$

In this thesis, loading stress paths are in $-90^\circ < \theta < 90^\circ$ and unloading stress paths are in $90^\circ \leq \theta \leq 270^\circ$. Figure 4-1 depicts the initial stress point, stress paths, and stress path angle used.

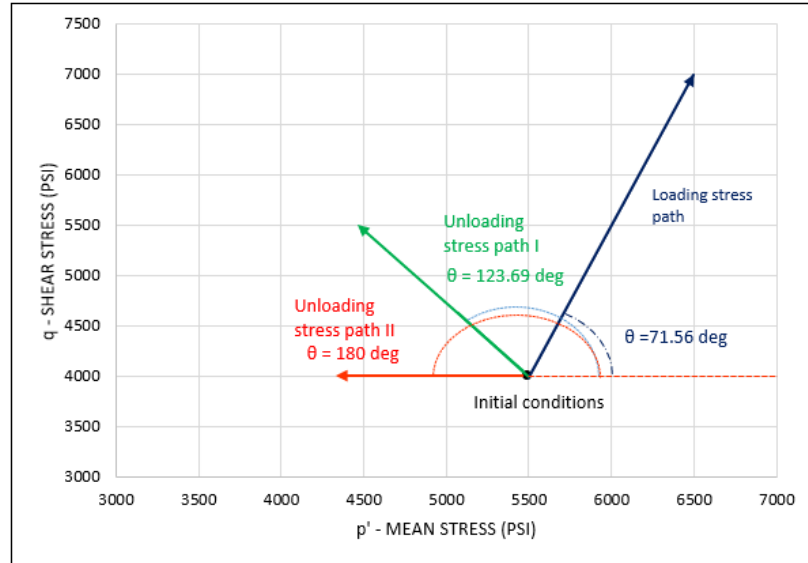


Figure 4-1 Shows the loading stress path and unloading stress paths used in this study. The loading stress paths are in $-90^\circ < \theta < 90^\circ$ and unloading stress paths are in $90^\circ \leq \theta \leq 270^\circ$.

The Introduction Chapter presented previous experimental studies in the areas loading and unloading yield behaviors for different geo-materials. In this chapter, we will present a detailed introduction to stress paths with emphasis on injection or unloading conditions for unconsolidated sands in high mean effective stress ranges. Most of the published works have focused on higher yield stress materials and without pore fluid effect as compared to unconsolidated sands. Previous studies published in unconsolidated sands by Hamoud (2012), Oldakowski (1994) and Touhidi (1998) were in low effective stress regimes of less than 250 psi mean effective stress for applications in the Alberta oil sands. The current research work aims to understand the effects of injection on unconsolidated sands in depleted deep-water reservoir stress conditions. They are of work focuses on much higher effective stress magnitudes in the

range of 2000 to 5000 psi mean effective stress. Figure 4-2 summarizes yield stress and mean effective stress ranges of previous studies and this study.

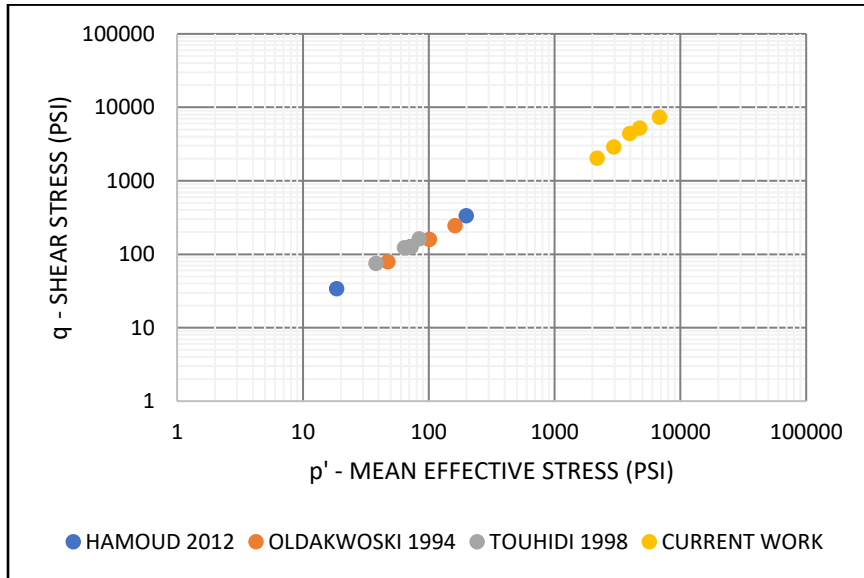


Figure 4-2 Previous work on strength properties measurement on unconsolidated sands were done by researchers focused on the Alberta oil sands which have low effective stresses (< 250 psi). Current work focuses on higher stress magnitudes (> 2000 psi).

This study aims to investigate the dependence of stress path magnitude and direction on the yielding behavior of unconsolidated sands under injection and predict yielding behavior under different stress path directions and magnitudes. Three stress path directions have been tested with each stress path having different initial stress conditions. These stress paths include: one traditional triaxial loading stress path and two unloading stress paths to simulate injection. The stress paths taken to the different initial stress points were the same. The yield surfaces obtained from these three stress paths are analyzed to develop a predictive model.

All test samples were made using the same analogue sand material, dry sand packed method, and pre-consolidated procedure to reservoir conditions as described in Chapter 2. In the following section the test loading procedure will be discussed in detail.

4.1 Test Procedure

After test samples are made and pre-consolidated, we proceed to bring each test sample to its initial stress point. The same stress path is used to bring each test sample to its initial stress point; therefore, possible effects of using different stress paths to different initial stress points are avoided. Once the sample is at its desired initial stress point, we then load or unload the sample with the specified stress path direction to the yield stress condition. We use three different stress path directions. These include: one triaxial loading stress path, and two unloading-based stress paths. The unloading tests consist of a constant axial stress and a constant shear stress.

4.1.1 Loading-Based Yield Behavior

The first stress path presented is the loading triaxial stress path. To determine this triaxial loading yield behavior or yield surface, we used 2 triaxial tests. A Multi-stage triaxial test to determine the loading-based yield surface for different initial mean effective stress point. A Single-stage triaxial test to verify the yield surface obtained from the Multi-stage triaxial test. We start with the simpler Single-stage triaxial test to discuss the initial stress path in arriving to the initial stress point and then the triaxial stress path to the yield stress point.

4.1.1.1 Single-Stage Triaxial Test

The Single-stage triaxial test uses one sample to determine the yield stress point. The stress path to get to the initial stress point is isostatic. From the initial stress point to the yield stress point, the stress path is known as loading “triaxial.” This consists of maintaining the confining stress of the initial stress point constant while increasing the axial stress to yield. Figure 4-3 shows the applied axial and confining stresses and the calculated shear stress versus time for this test. The sample is first loaded isostatically (with equal axial stress and confining pressure) to 4350 psi. After that point the confining stress of 4350 psi is held constant while the axial stress is increased to yield the sample. Figure 4-4 depicts the isostatic stress path to the initial stress point

and then the triaxial stress path from the initial stress point to the yield stress point in p' - q stress space. The isostatic and triaxial stress path are “loading” since they have increasing p' and with $90^\circ < \theta < 90^\circ$ (Figure 4-1).

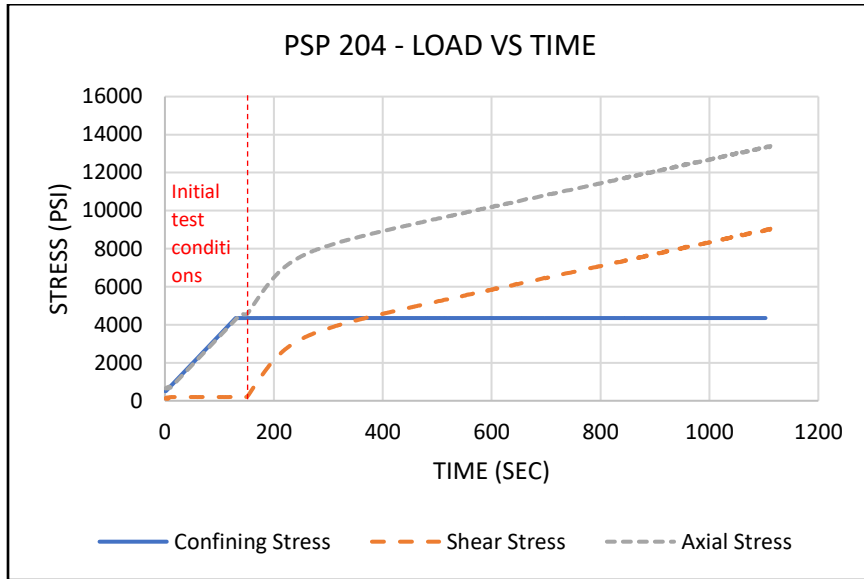


Figure 4-3 Shows the initial test conditions and load vs time plot single-stage triaxial test with a confining stress of 4350 psi.

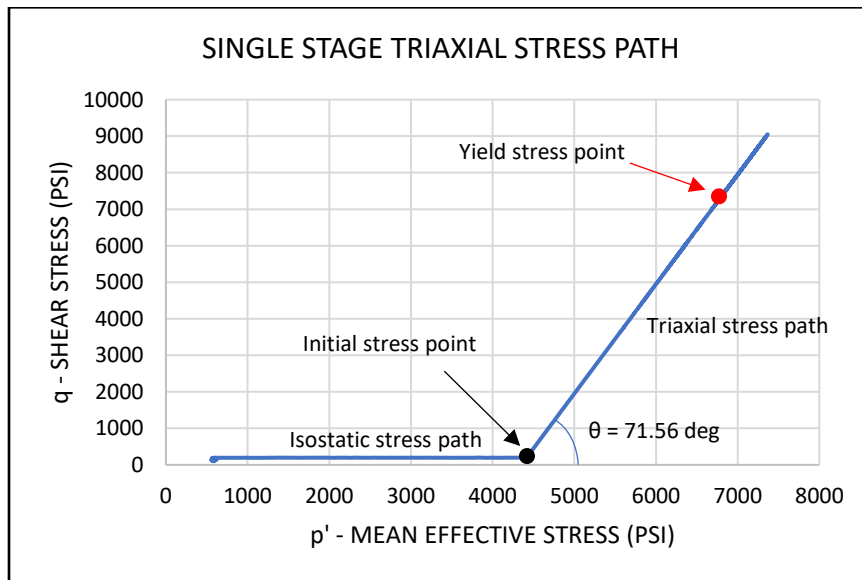


Figure 4-4 Shows the stress path followed by the single stage triaxial test in a mean effective stress - shear stress plane with the initial stress point and the yield stress point.

4.1.1.2 Multi - Stage Triaxial Test

Kovari et al. (1975) introduced the “multiple failure” stage triaxial test. It is also known as the Multi-stage Triaxial test. A key advantage for this test is that it only needs one sample to determine the loading yield surface as a function of different initial stress points. The Single-stage triaxial test uses one sample to determine each yield stress point for a given initial stress point. Therefore, multiple samples are needed to determine a yield surface from multiple initial stress points. Many researchers (Kim et al., 1979; Crawford et al., 1987; Holt et al., 1991; Pagoulatos et al., 2004; Jambunathan, 2008; Taheri et al., 2008; Al-Salman et al., 2015; Bilal et al., 2017; and Dessouki et al., 2020) have validated that the Multi-stage Triaxial Testing procedure is an effective alternative to a series of single stage triaxial tests to determine the loading yield surface.

The Multi-stage triaxial test follows similar stress paths as the Single-stage triaxial test. The test sample starts with an isostatic stress path to the first initial stress point and loads the sample with the triaxial stress path to yield. After that it unloads triaxially back to the first initial stress point, reloads isostatically to the second initial stress point and triaxially loads to the second yield stress point. This process continues and repeats for other initial stress points and their corresponding yield stress points. Figure 4-5 shows the variation of applied loads (confining and axial stresses, and the corresponding calculated shear stress) with time. A total of four “initial” confining stress stages namely – 1500 psi, 2000 psi, 2500 psi, and 3000 psi were performed to get the loading - based triaxial yield surface. Figure 4-6 depicts these initial stress points, their loading stress paths and corresponding yield stress points in the p' - q plot.

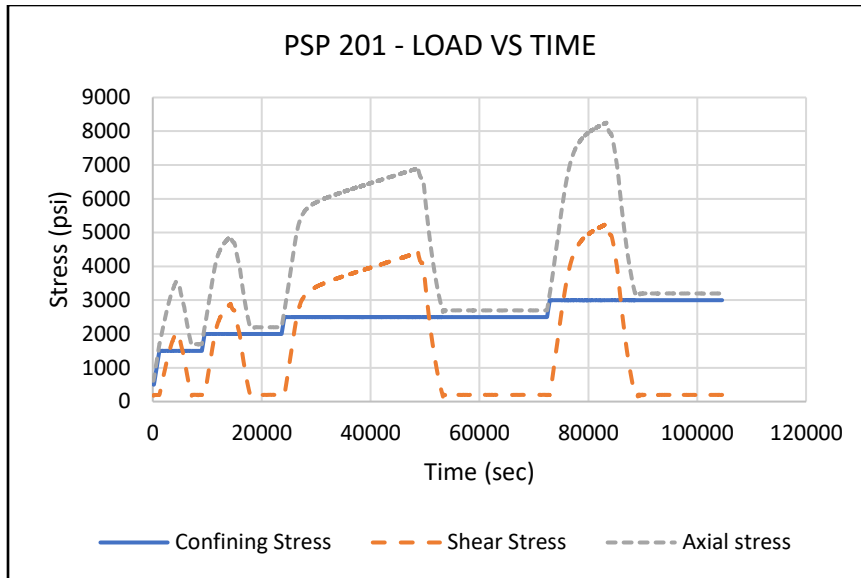


Figure 4-5 Shows the application of confining stress and shear stress in the multi-stage triaxial test.

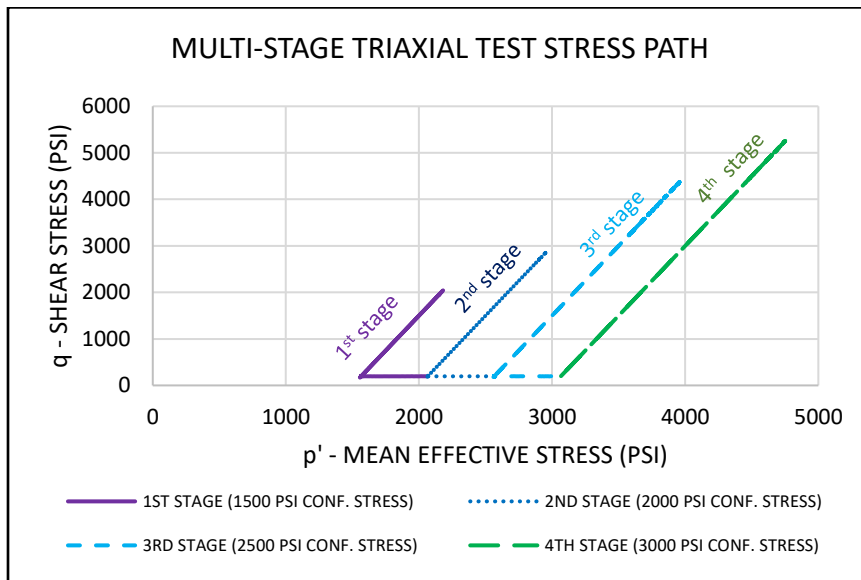


Figure 4-6 Shows the stress path followed by each stage in the multi-stage triaxial test in a mean effective stress - shear stress space.

In this section, we presented the loading procedure and stress path direction for triaxial stress path. In the following section, the unloading-based stress path directions will be covered.

4.1.2 Unloading-Based Yield Behavior

Unloading - based yield behavior also depends on the stress path bringing the sample to its initial stress point, the magnitudes of this initial stress point, and the “unloading” stress path

from this initial stress point to the yield stress point. Stress path directions are called unloading in reference to decreasing nature of the mean effective stress or for stress path angle of $90^\circ \leq \theta \leq 270^\circ$ (see Figure 4-1). In this section, we will describe the two unloading-based stress path directions used to determine unloading-based yield surfaces.

During the injection phase, the pore pressure of the reservoir is increasing and therefore the mean effective stress on the rock matrix is decreasing. The reservoir stress path could either have increasing shear stress, constant shear stress or decreasing shear stress (Figure 4-7). For decreasing shear stress, we are moving away from the estimated yield surface as we unload both in mean effective stress and shear stress directions. Therefore, the material is not expected to yield during this stress path. For the other two cases of increasing shear stress or constant shear stress, we approach the yield surface when we are increasing pore pressure (i.e., reducing p'). Therefore, the material is expected to yield in these cases.

Researchers in mining and tunneling industry have achieved controlled unload tests for two unloading stress paths namely - Constant Axial Stress Unloading Test (CASUT) and Constant Shear Stress Unloading Test (CSSUT). In the first stress path the shear stress increases with decreasing mean effective stress. This stress path is more representative of reservoir conditions. The second stress path has a constant shear stress with decreasing mean effective stress. This stress path brackets the lower limit of unloading tests. Therefore, we use these two unloading stress paths to compare the yield surface for loading and unloading tests.

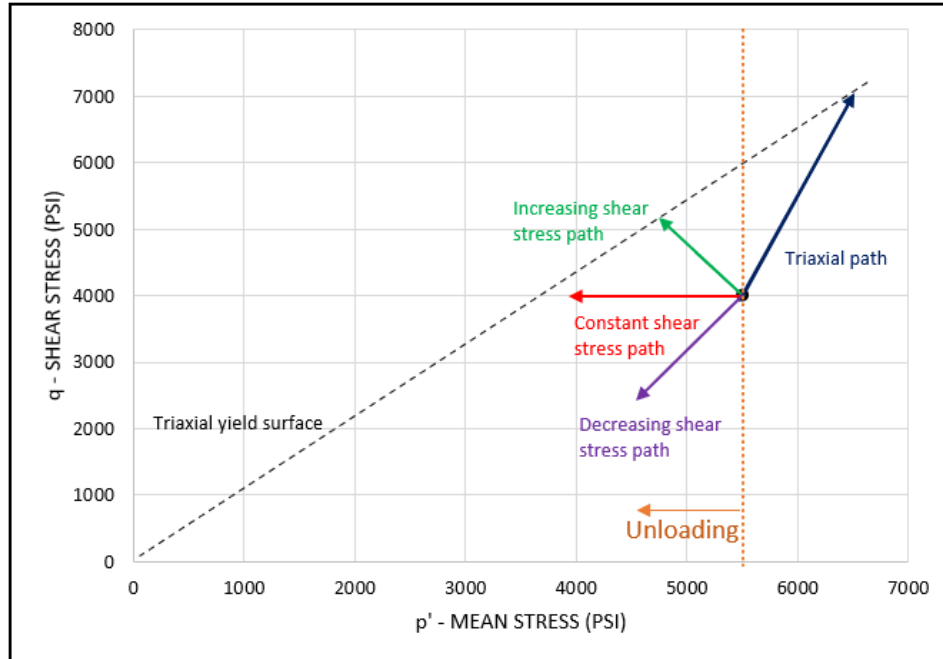


Figure 4-7 Shows the different stress paths for loading and unloading. During injection, mean effective stress increases with either decreasing or constant or increasing shear stress. The most representative stress path for actual reservoir conditions is the increasing shear stress path.

4.1.2.1 Constant Axial Stress Unloading Tests

The first set of unloading-based tests is called the constant axial stress unloading test (CASUT). A total of four such unload tests (Samples PSP 212, PSP 209, PSP 210, PSP 211) is completed to determine the unload yield surface at four different initial stress points. The stress path used to reach these initial stress points follows that of the single-stage triaxial test. This initial stress path consists of:

- Start with isostatic load to the confining stress of 4350 psi.
- Then load with triaxial stress path to the specified initial stress point.

Load versus time plots for samples PSP 212, PSP 209, PSP 210 and PSP 211 are shown in Figure 4-8, Figure 4-9, Figure 4-10, and Figure 4-11, respectively, to show the changes in axial stress and confining stress as we progress through the test. All samples in this section undergo this experimental protocol.

Table 4-1 summarizes the initial stress magnitudes of p' and q for these four initial stress points and their corresponding applied axial (σ_1) and confining (σ_3) stresses. The axial stresses are selected to have a uniform shear stress difference of ~ 1000 psi.

Once the sample has reached the desired initial stress point, the constant axial stress unloading stress path is as follows:

- Unload sample by decreasing the confining stress at a rate of 0.5 psi per second while keeping the axial stress constant.
- Terminate the unloading test when the axial strain gauges reach their measurement limit.
- Load versus time plots for samples PSP 212, PSP 209, PSP 210 and PSP 211 are shown in Figure 4-8, Figure 4-9, Figure 4-10, and Figure 4-11, respectively, to show the changes in axial stress and confining stress as we progress through the test. All samples in this section undergo this experimental protocol.

Table 4-1 A summary table of initial stress states for all constant axial stress unloading tests are shown.

SAMPLE	σ_1	σ_3	Initial p'	Initial q
PSP 212	9300	4350	6000	4950
PSP 209	8400	4350	5700	4050
PSP 210	7350	4350	5350	3000
PSP 211	6360	4350	5020	2010

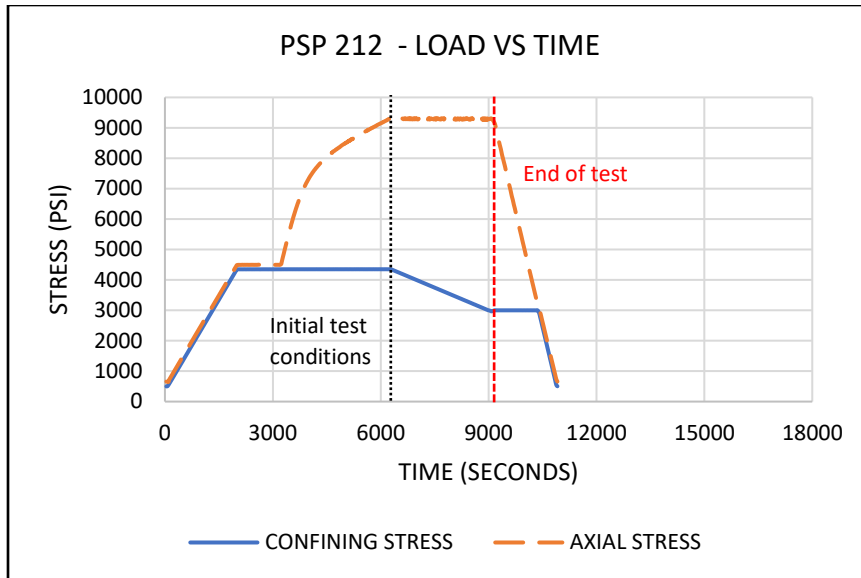


Figure 4-8 Shows the load vs time plot for PSP 212. This test is performed at the constant axial stress value of 9300 psi with an initial confining stress of 4350 psi.

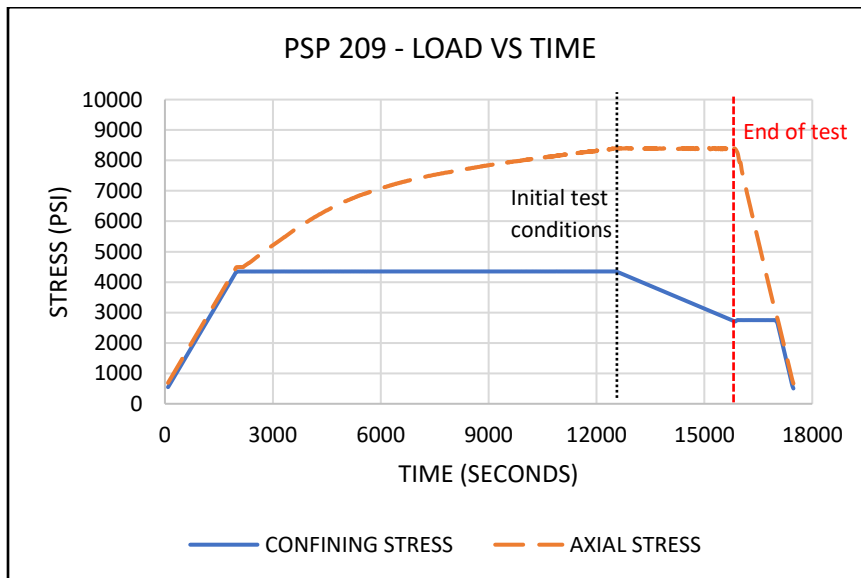


Figure 4-9 Shows the load vs time plot for PSP 209. This test is performed at the constant axial stress value of 8400 psi with an initial confining stress of 4350 psi.

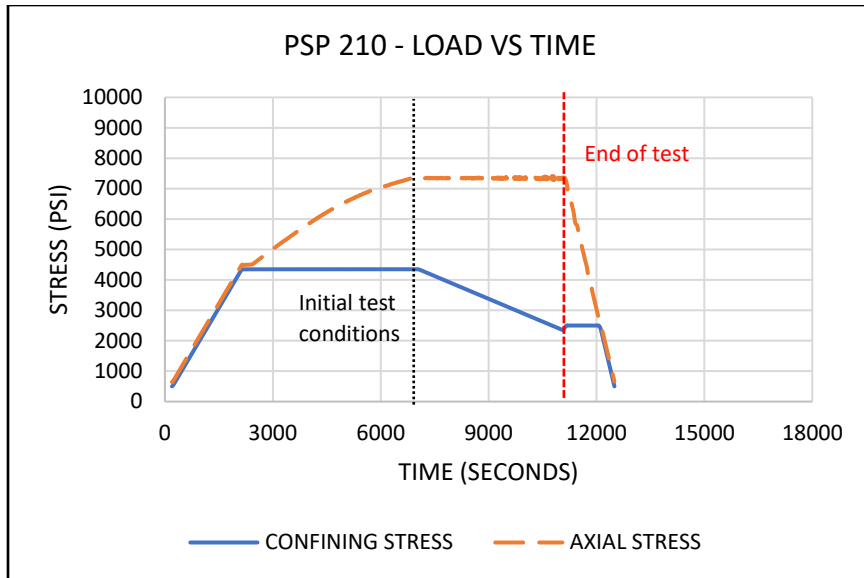


Figure 4-10 Shows the load vs time plot for PSP 210. This test is performed at the constant axial stress value of 7350 psi with an initial confining stress of 4350 psi.

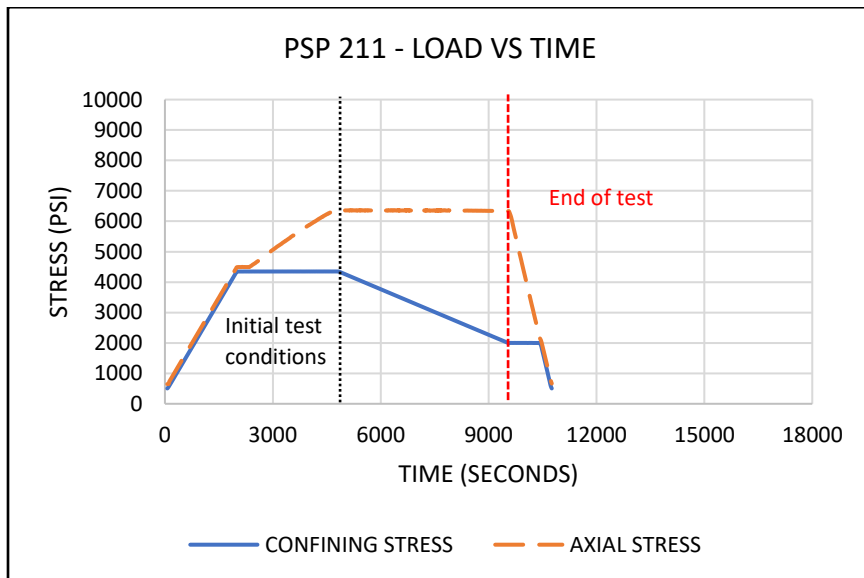


Figure 4-11 Shows the load vs time plot for PSP 211. This test is performed at the constant axial stress value of 6360 psi with an initial confining stress of 4350 psi.

Figure 4-12 shows the combined plot of stress paths for tests in the set of constant axial stress unloading tests. The samples are isostatically loaded to 4350 psi and then triaxially loaded

to their pre-determined initial shear stress values. Then the sample is unloaded in a constant axial stress path as shown in the p' - q space.

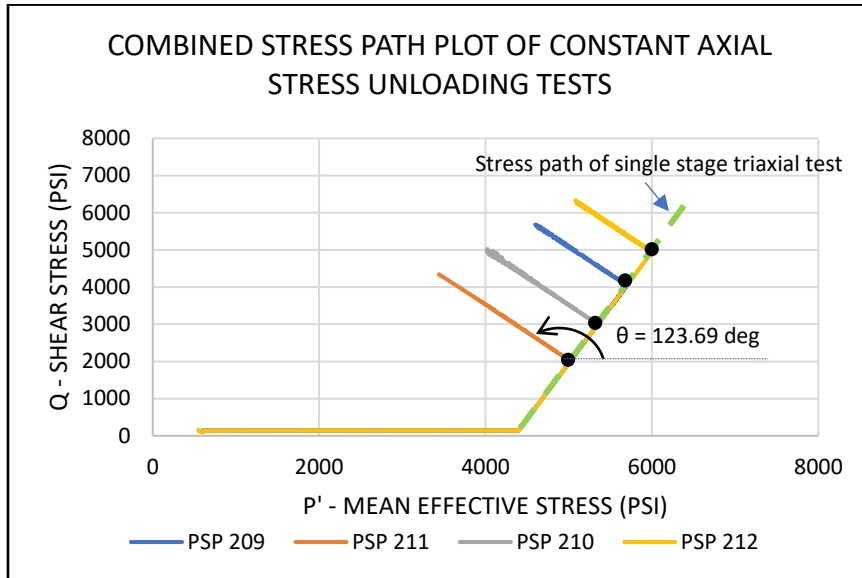


Figure 4-12 Shows a combined plot of stress path for constant axial stress tests.

4.1.2.2 Constant Shear Stress Tests

The second set of unloading based tests is called the constant shear stress unloading tests (CSSUT). A total of three such unload tests (Samples PSP 207, PSP 205, and PSP 208) is completed to determine the unload yield surface at these three different initial stress points. The stress path used to reach these initial stress points also follows that of the single-stage triaxial test. This initial stress path consists of:

- Start with isostatic load to the confining stress of 4350 psi.
- Then load with triaxial stress path to the specified initial stress point.

Load versus time plots for samples PSP 212, PSP 209, PSP 210 and PSP 211 are shown in Figure 4-8, Figure 4-9, Figure 4-10, and Figure 4-11, respectively, to show the changes in axial stress and confining stress as we progress through the test. All samples in this section undergo this experimental protocol.

Table 4-1 summarizes the initial stress magnitudes of p' and q for these three initial stress points and their corresponding applied axial and confining stresses. The initial shear stresses of 4950, 4050, and 3000 psi were chosen to have a uniform shear stress difference of ~ 1000 psi.

Once the sample has reached the desired initial stress point, the constant shear stress unloading stress path is as follows:

- Unload sample by decreasing the confining stress at a rate of 0.5 psi per second while keeping the shear stress constant. This is accomplished by controlling the axial load such that for a given confining stress change the system maintains the shear stress constant.
- Terminate the unloading test when the axial strain gauges reach their measurement limit.

Load versus time plots for samples PSP 207, PSP 205, and PSP 208 are shown in Figure 4-13, Figure 4-14, and Figure 4-15, respectively, to show the changes in axial stress, shear stress and confining stress as we progress through the test.

Table 4-2 Shows the initial stress states for samples where a constant shear stress test performed.

SAMPLE	σ_1	σ_3	Initial p'	Initial q
PSP 207	9300	4350	6000	4950
PSP 205	8400	4350	5700	4050
PSP 208	7350	4350	5350	3000

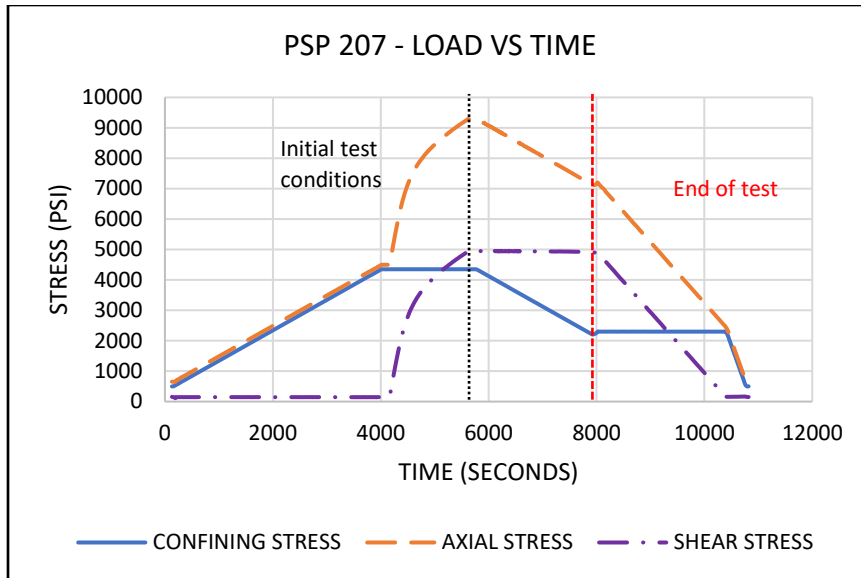


Figure 4-13 Shows the load vs time plot for PSP 207. This test is performed at the constant shear stress value of 4950 psi.

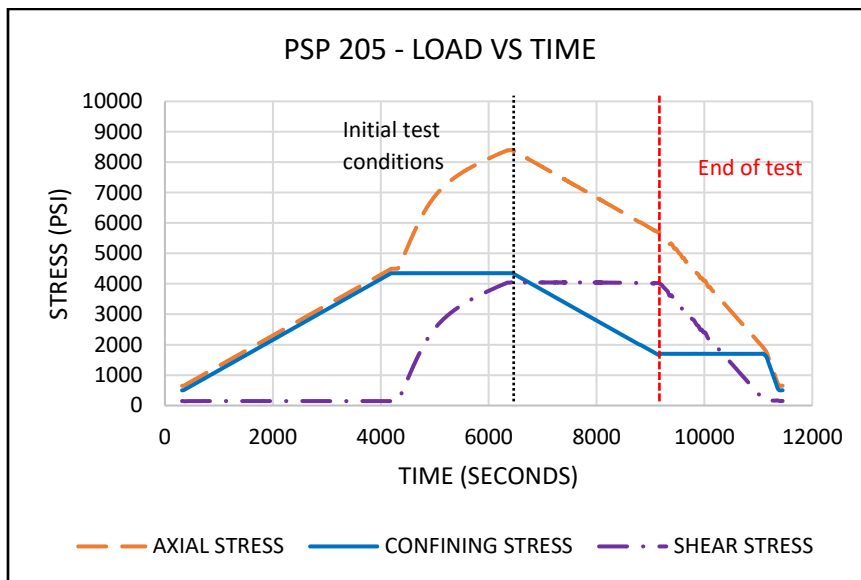


Figure 4-14 Shows the load vs time plot for PSP 205. This test is performed at the constant shear stress value of 4050 psi.

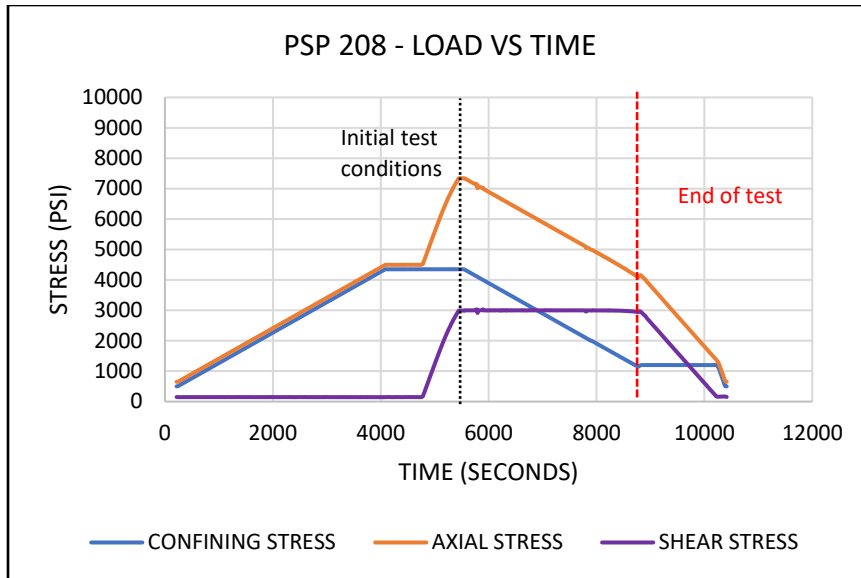


Figure 4-15 Shows the load vs time plot for PSP 208. This test is performed at the constant shear stress value of 3000 psi.

Figure 4-16 shows the combined plot of stress paths for tests in the set of constant shear stress unloading tests. The samples are isostatically loaded to 4350 psi and then triaxially loaded to their pre-determined initial shear stress values. Then the sample is unloaded in a constant shear stress path as shown in the p' - q space.

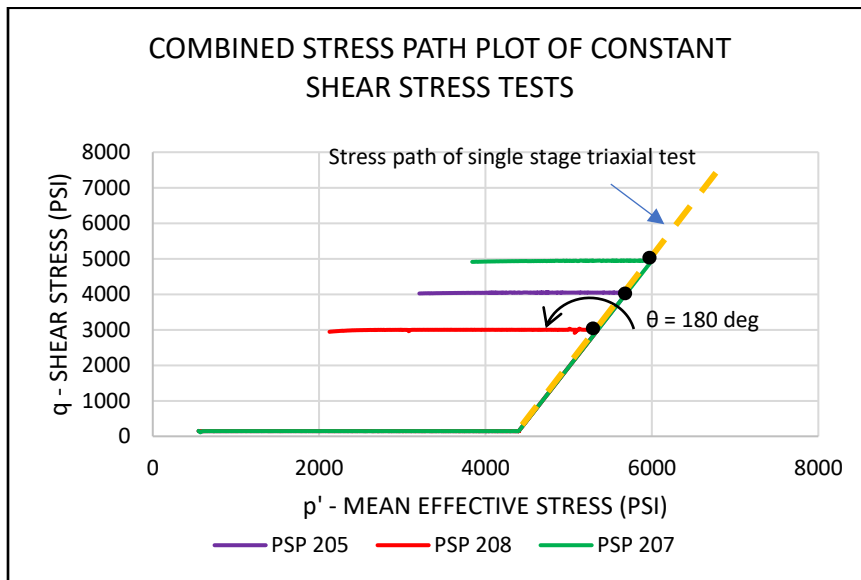


Figure 4-16 Shows a combined plot of stress path for constant axial stress tests.

In this section, we have covered the various tests that have been performed for this research work and their loading procedures. We performed two tests to map the loading based triaxial yield surface and two unloading stress path tests to map two unloading based yield surfaces. In the next section we will perform detailed analysis of the data gathered in the tests.

4.2 Data Analysis

In this section, we will detail the sample response to the stress paths mentioned in the previous section. We will characterize the response of samples into loading-based tests and the unloading-based tests, and then compare both types of yield surfaces.

An important element of this analysis is using a consistent method to select the “yield stress” point. Prakash et al. (2018) established the point of positive dilatancy as a suitable unloading point or yield stress point to map the loading based yield surface in a multi-stage triaxial test. This point corresponds to the ratio of radial strain over axial strain of 0.5 or when the volume strain changes direction from compression to dilation. In this thesis, the point of positive dilatancy is used to determine the yield stress point for loading and when appropriate also for unloading tests. Other yield point selection criteria, such as the maximum curvature of the mean effective stress versus volume strain curve, are also used. The selection of yield or unloading point will be discussed in more details in each loading and unloading stress path tests.

4.2.1 Loading-Based Yield Behavior

As described in section 4.1.1, one multi-stage triaxial test and one single test triaxial test were performed on two samples to map the loading-based triaxial yield surface.

4.2.1.1 Multi-Stage Triaxial Test

Figure 4-17 shows the stress vs axial strain plot of the sample under the four triaxial stages of the multi-stage triaxial test (PSP 201). Individual loading stages were unloaded when the sample reached the point of positive dilatancy (Prakash et al., 2018). Figure 4-18 shows the values

of tangent strain ratio (ratio of change in radial strain to change in axial strain) during each stage. When the sample reaches the point of positive dilatancy, i.e. the tangent strain ratio reaches 0.5, the sample is unloaded or yielded. The value of shear stress at this point of unloading is selected as the yield stress point to map the loading based yield surface.

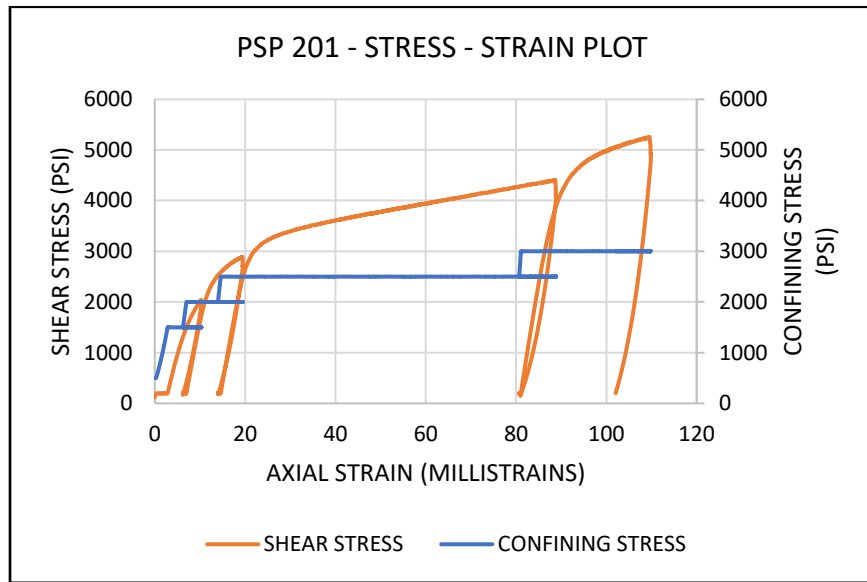


Figure 4-17 Shows the stress vs strain plot for the multi-stage triaxial test. Four different confining stress stages - 1500 psi, 2000 psi, 2500 psi, and 3000 psi were performed.

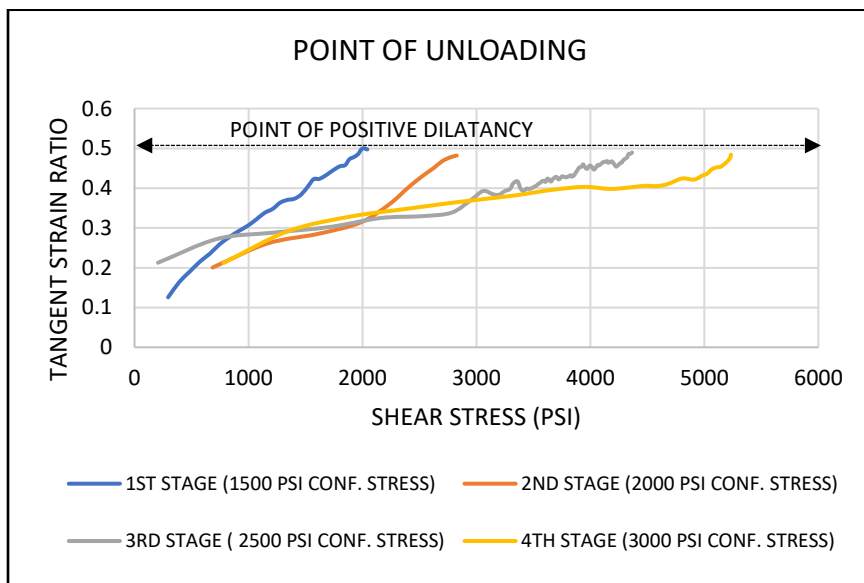


Figure 4-18 Shows the tangent strain ratio vs shear stress for all stages of the multi-stage triaxial test. The loading stage is unloaded when point of positive dilatancy (tangent strain ratio of 0.5) is reached.

On an effective mean stress – shear stress plane, the loading-based yield surface is shown in Figure 4-19. It is approximated to be a straight line passing through the origin with a slope of 1.076.

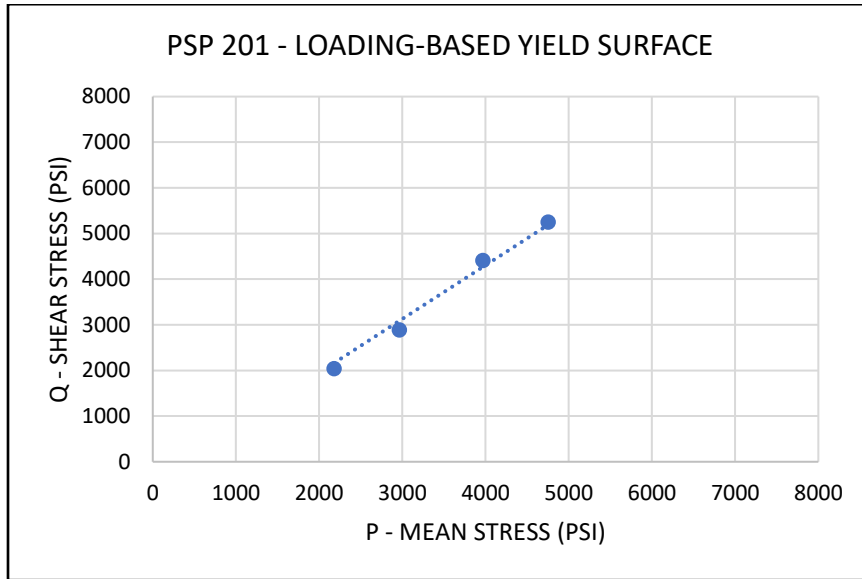


Figure 4-19 Loading-based yield surface calculated from yield points of the Multi-stage triaxial test.

4.2.1.2 Single Stage Triaxial Test

As mentioned in section 4.1.1, a single stage triaxial test (PSP 204) with a confining stress of 4350 psi was performed to validate the multi-stage triaxial test. Figure 4-20 shows the stress-axial strain plot of this single stage triaxial test. The sample was loaded until the strain gauges reached their limit. As can be seen from the plot, a ductile failure with work hardening (Jaeger, 2007) occurs in this test. Figure 4-21 shows the evolution of tangent strain ratio with applied shear stress. The value of yield stress at the point of positive dilatancy is 7400 psi.

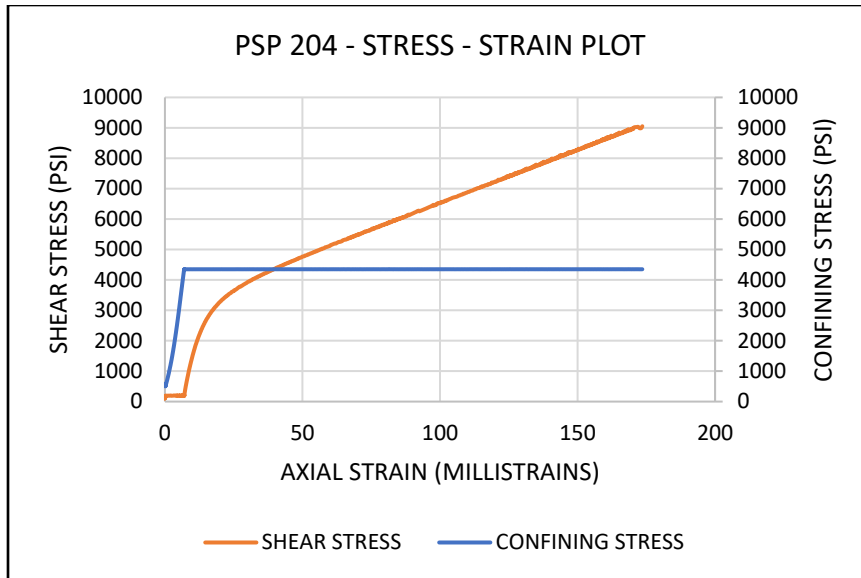


Figure 4-20 Shows the stress-strain plot of the single stage triaxial test. The test was concluded when the axial strain sensor was at limit.

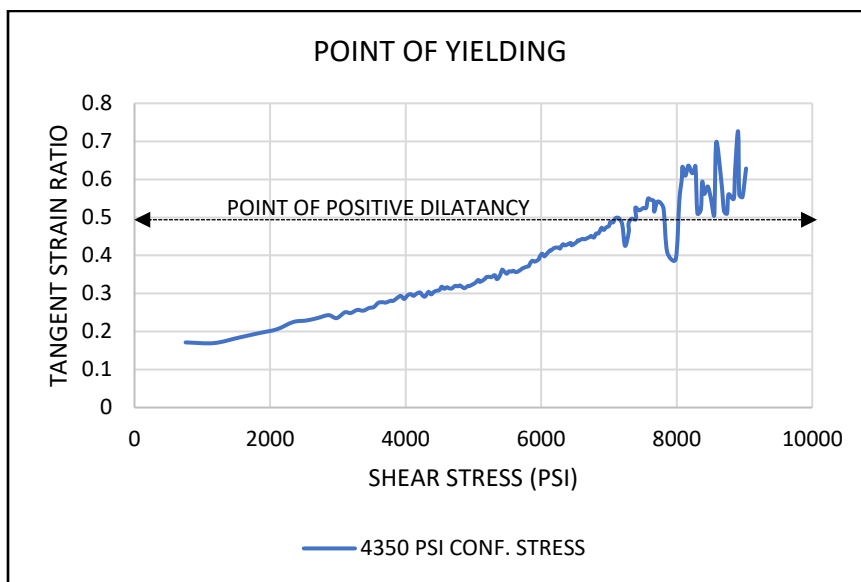


Figure 4-21 Shows a plot of tangent strain ratio vs shear stress for the single stage triaxial test. This plot is used to pick the yield point i.e., the shear stress value when the tangent strain ratio reaches 0.5.

4.2.1.3 Summary of Loading - based Triaxial Tests

In this section, both the triaxial stress tests will be summarized to get the loading-based yield surface. Figure 4-22 shows a combined plot of tangent strain ratio and shear stress for each stage of the multi-stage triaxial test and the single stage triaxial test. The yield stress points are selected from this plot to map the loading-based triaxial yield surface. Figure 4-23 shows the

combined yield points on the mean effective stress – shear stress plane. The yield point of the single stage triaxial test aligns with the data from Multi-stage triaxial test validating the use of multi-stage triaxial test for measuring strength properties of unconsolidated sands.

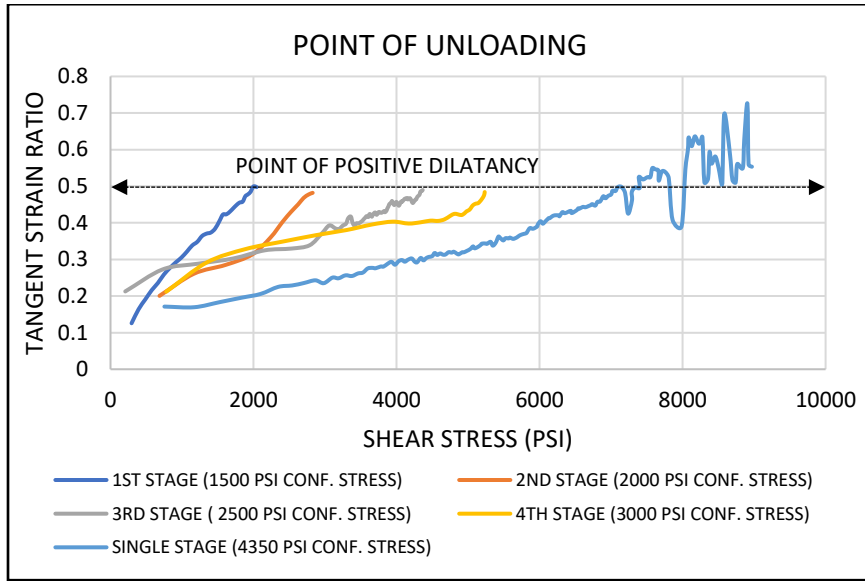


Figure 4-22 Shows a combined plot of tangent strain ratio and shear stress. Yield stress points from each stage of the multi-stage triaxial test and the single stage triaxial test are used to map the yield surface.

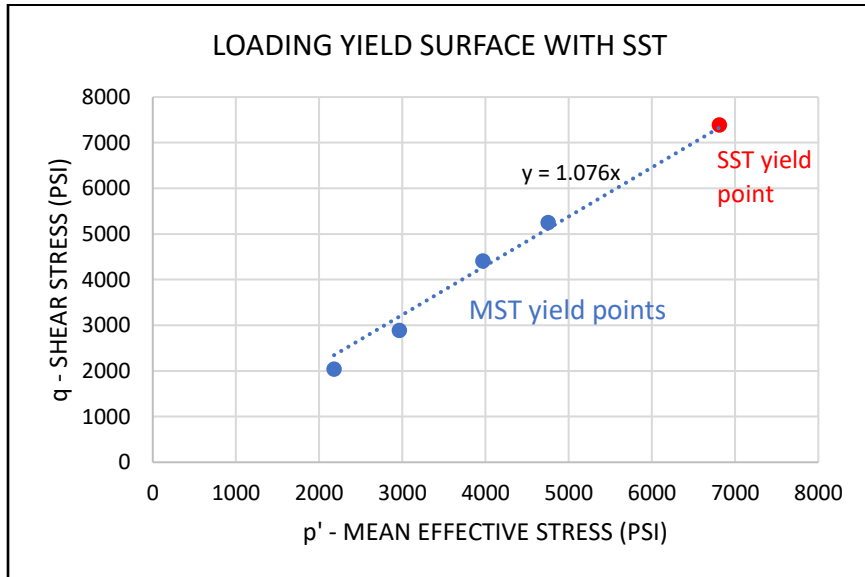


Figure 4-23 The yield point from single stage triaxial test (SST) plotted on the multi-stage triaxial test (MST) yield surface shows perfect match. This observation validates the use of multi-stage triaxial test from determining loading-based yield surface.

4.2.2 Unloading Based Tests

As described in section 4.1.2, a total of seven unloading based tests with two different stress paths directions were performed in this research work – four constant axial stress unloading tests and three constant shear stress unloading tests. For each stress path direction, a yield surface is mapped and then, all the yield surfaces will be compared against each other.

4.2.2.1 Constant Axial Stress Unloading Tests

The constant axial stress unloading tests (CASUT) are performed by decreasing the confining stress while keeping the axial stress constant. Therefore, the shear stress increases as the test progresses. Figure 4-24 shows the combined plot of shear stress vs axial strain for the four CASUT. Each test has different initial stress point which can be seen from the starting value of shear stress for each sample.

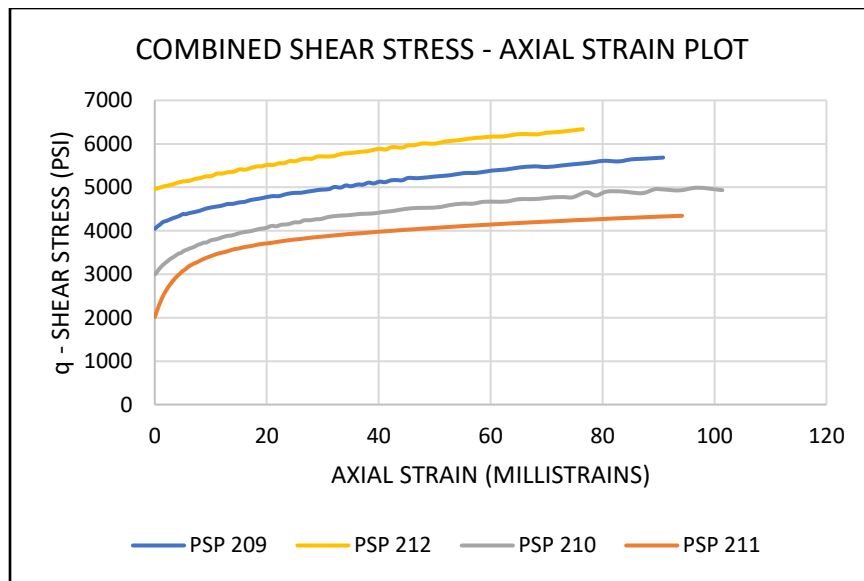


Figure 4-24 The combined plot of four constant axial stress tests showing the evolution of axial strain with increase in shear stress.

Since, the mean effective stress is decreasing with decreasing confining stress, a more appropriate stress strain plot is the mean effective stress vs volume strain plot which captures the volumetric behavior of the sample. Figure 4-25 shows the plot of mean effective stress and

volume strain. Note, negative volume strain represents expansion or increases in volume. In this plot, the volume strain shows a distinct change in slope for each sample.

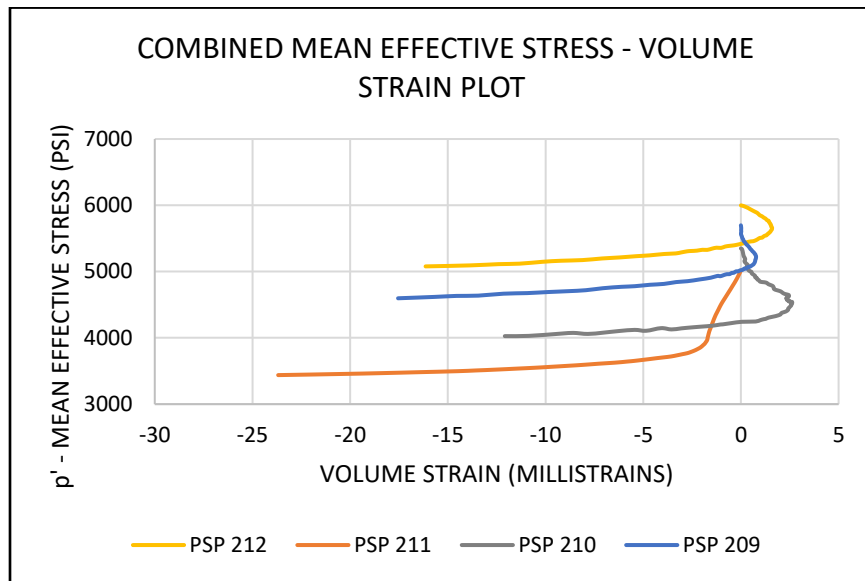


Figure 4-25 Shows the combined plot of four constant axial stress tests showing the evolution of volume strain with decrease in mean effective stress.

The yield criteria used to pick yield points in this set of tests is the point of positive dilatancy which is the same as for the loading triaxial tests. Figure 4-26 shows the combined plot of tangent strain ratio and mean effective stress for all samples in this set. Curves for all samples pass through the point of positive dilatancy except for the test with the lowest initial shear stress (PSP 211). This type of behavior – starting out with high tangent strain ratio and decreasing until it starts to increase again - is seen in all samples except for PSP 212 (highest initial shear stress). An explanation for this observation is as follows–

1. Higher value of mean effective stress makes the sample stronger whereas higher value of shear stress makes the sample weaker.

2. If the initial stress state of the sample is closer to the yield surface, the sample behaves similar to PSP 212 (which has the highest yield stress). It would start with a low value of tangent strain ratio and monotonically increase to point of positive dilatancy and beyond.
3. If the initial stress state of the sample is farther away from the yield surface, the applied mean effective stress is higher than the required mean effective to support the applied shear stress. In such a case, reducing the mean effective stress does not effect a change in the sample response. The sample behaves as if it is unloading in both directions and the tangent strain ratio decreases.
4. At some point during the unload test, the mean effective stress reaches a point similar to step 2. The value of mean effective stress is no longer higher than the required mean effective stress to support the applied shear stress. At this point, the tangent strain ratio changes direction and start to increase.
5. This increase of tangent strain ratio takes place through the rest of the loading cycle where the sample continues to deform to sustain the increasing shear stress applied with a reduction in mean effective stress.

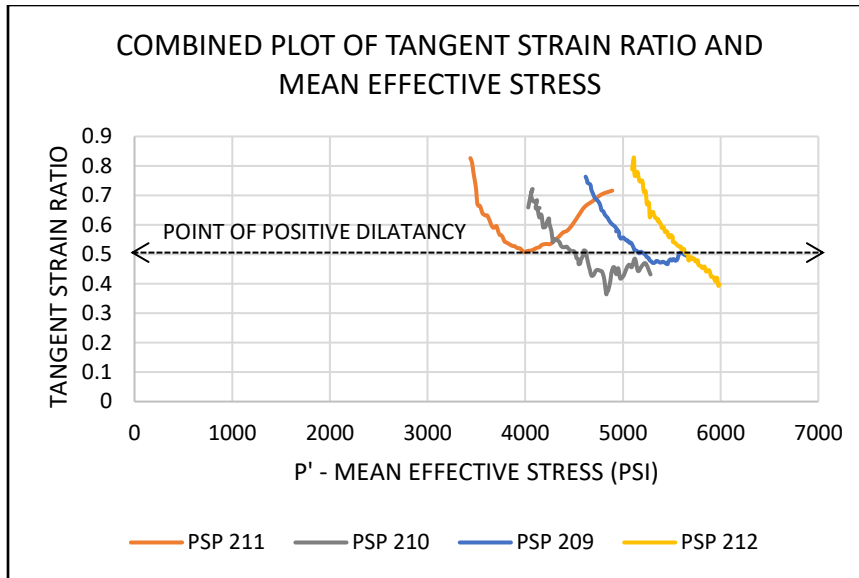


Figure 4-26 Shows the combined plot of tangent strain ratio vs mean effective stress for all tests in the set of constant axial stress tests. As can be seen, all the curves touch the point of positive dilatancy.

The yield points used to map the unloading-based constant axial stress yield surface are inferred from the point of positive dilatancy. This point is also a close match with the point of maximum curvature in the volume strain behavior (Figure 4-256).

In the mean effective stress - shear stress space, the yield points are plotted as shown in Figure 4-27. The slope of the unloading based constant axial stress yield surface is 1.077. The slope is similar to that of the triaxial loading based yield surface of 1.076 in Figure 4-23. However, the yield constant (q intercept at $p'=0$) is not zero as compared to the triaxial loading based yield surface.

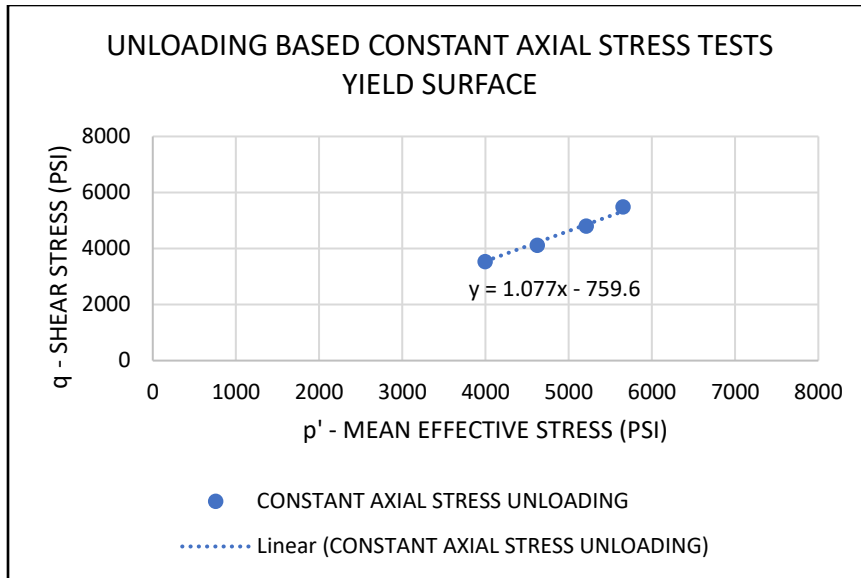


Figure 4-27 Shows the yield points of the constant axial stress unloading tests in the mean effective stress - shear stress plane. The slope of the yield surface is 1.07, similar to the triaxial loading yield surface but the yield constant is different.

The yield surface characteristics obtained from this suite of CASUT can be interpolated with the upper and lower bounds of the test conditions. It is important to emphasize that these unloading tests are for high mean effective stresses in the ranges of 4000 psi to 5400 psi (Figure 4-27). Therefore, extrapolating the yield surface to the lower stress values near the origin must be substantiated with an experimental observation before we can do so with high degree of confidence.

4.2.2.2 Constant Shear Stress Unloading Tests

The constant shear stress unloading tests (CSSUT) are performed by decreasing the confining stress while keeping the shear stress constant. Therefore, the axial stress decreases as the test progresses. Figure 4-28 shows the combined plot of shear stress vs axial strain for the three tests. Each test has different initial stress conditions which can be seen from the starting shear stress value, and the shear stress stays constant as defined.

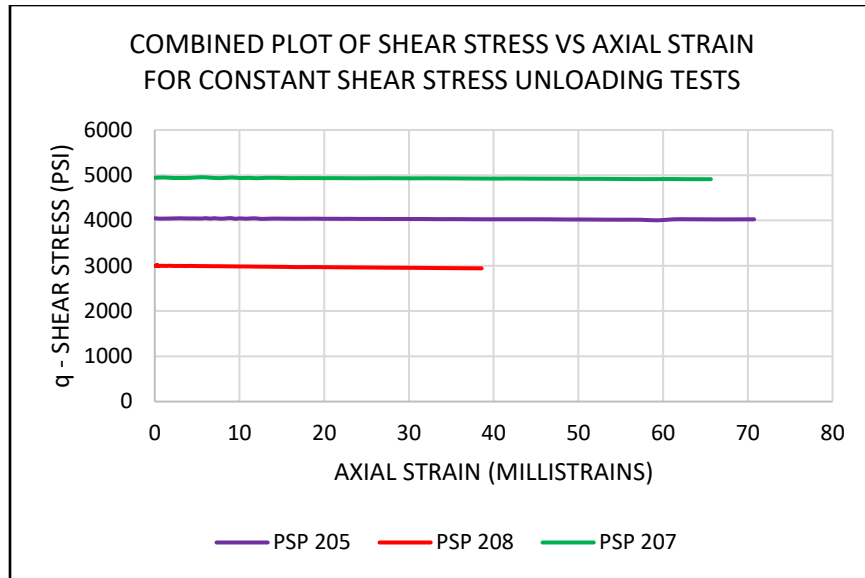


Figure 4-28 The combined plot of three constant shear stress unloading tests showing the evolution of axial strain as we progress through the tests. The shear stress maintains a constant value as it is a boundary condition for this set of tests.

Since, the mean effective stress is decreasing with decreasing confining stress, a more appropriate stress strain plot is the mean effective stress vs volume strain plot which captures the volumetric behavior of the sample. Figure 4-29 shows the plot of mean effective stress and volume strain. These curves show the volume strains are negatives (volume expanding) from the start for all cases tested. These curves show as the mean effective stress reduces the corresponding volume strain expands. However, there is a distinct change in slope for each sample when a slight reduction of mean effective stress results in a large expansion of volume strain. This represents a large increase in the sample's compliance which could represent the onset of yielding.

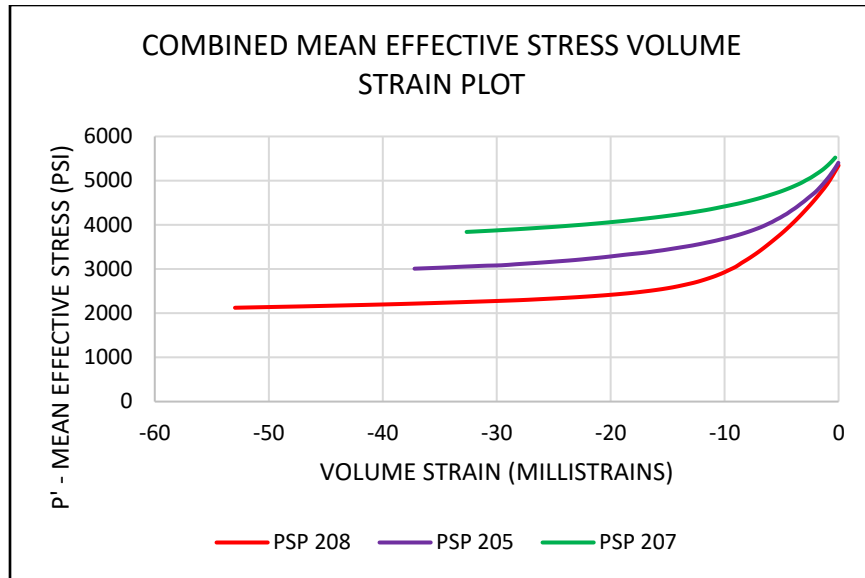


Figure 4-29 Shows the combined plot of three constant shear stress unloading tests showing the evolution of volume strain with decrease in mean effective stress.

The yield criteria used to pick the yield points for this set of tests is different than the other two sets of tests. However, the volume strain behavior after the yield point is consistent in all three sets of tests. In the Figure 4-29, it is observed that volume strain monotonically decreases with decrease in mean stress. However, similar to PSP 211 (Figure 4-25), a change of slope is observed in all three test samples in this set. Therefore, the yield criteria of maximum curvature on volume strain is used to infer yield points to be mapped as yield surface.

In the mean effective stress – shear stress space, the yield points are plotted as shown in Figure 4-30. The slope of the unloading based constant axial stress yield surface is 1.074. The slope is similar to that of the triaxial loading based yield surface. However, the yield constant is non - zero compared to the triaxial loading based yield surface.

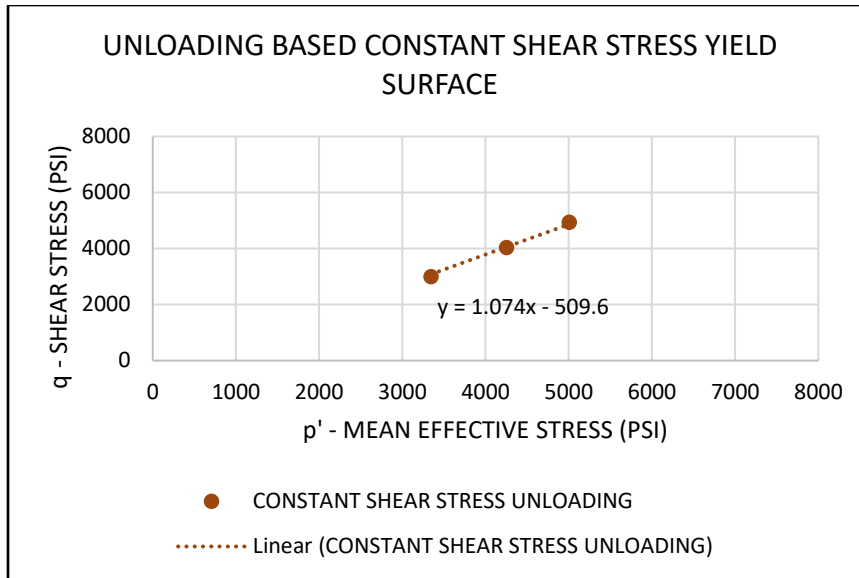


Figure 4-30 Shows the yield points of the constant shear stress unloading tests in the mean effective stress - shear stress plane. The slope of the yield surface is 1.07, similar to the triaxial loading yield surface but the coefficient is different.

The yield surface characteristics obtained from this suite of CSSUT can be interpolated with the upper and lower bounds of the test conditions. Again, it is important to re-emphasize that these unloading stress are for high mean effective stress ranges of 3400 psi to 5000 psi. Therefore, extrapolating the yield surface to the lower stress values near the origin must be substantiated with an experimental observation before we can do so with high degree of confidence.

In this section, we mapped three different yield surfaces for three different stress path directions – one loading and two unloading stress path directions. We discovered that the slopes of the three yield surfaces are equal while the yield constants are different. In the next section we will analyze this behavior to develop a global yield surface function.

4.3 Discussions and Results

In the previous section, we discovered that each of the three yield surfaces, described by a line, obtained from the experiments have similar slope but different yield constants. In this section, we will explore this behavior and develop a theory to explain this behavior.

Figure 4-31 depicts all yield surfaces obtained from our study in the p' - q space. These three loading and unloading yield surfaces have a similar slope but different yield constants for the range of mean effective stresses between 3000 psi and 6000 psi. The yield constants are of high significance. They show the dependence of yield surface on the stress path direction. For example, at a given mean effective stress value of 5000 psi, if the sample is on a triaxial stress path it can support 5400 psi of shear stress. On a constant shear stress path, this value reduces to 5000 psi. On a constant axial stress path, the shear stress reduces even further to 4600 psi. Therefore, the stress path being traversed is an important criterion to predict the yielding behavior of this unconsolidated sand material and in this high range of mean effective stresses.

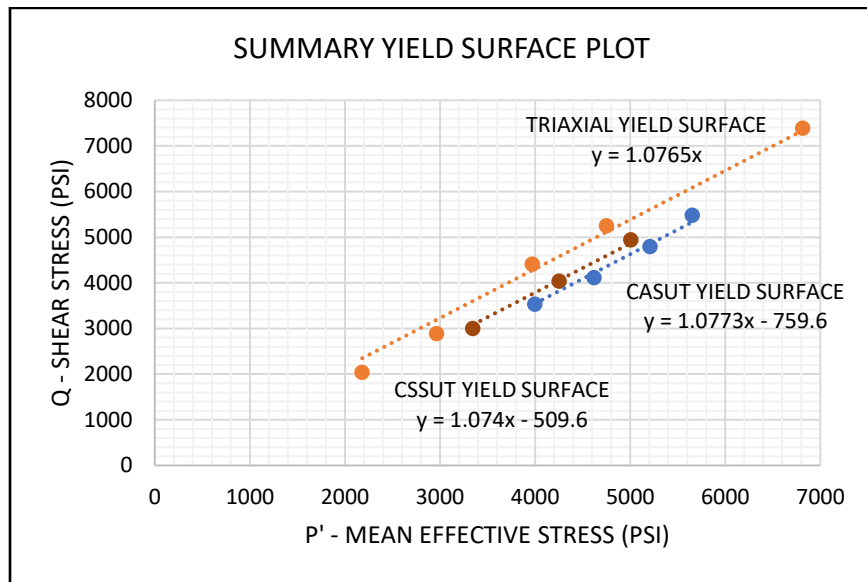


Figure 4-31 Shows the summary plot of the three yield surfaces obtained from experiments. All yield surfaces have similar slope with different yield constants.

Figure 4-32 shows similar slopes of all tested yield surfaces arrived from different stress path directions. Starting with the triaxial loading with stress path angle, θ , of 71.56° ; the constant axial stress unloading with θ of 123.69° and the constant shear stress unloading with θ of 180° ; they bracket a large portion of practical loading and unloading stress paths. Therefore, it is reasonable to assume a minimum global yield surface within this range of stress path angle to

have the same slope. Moreover, all these different surface moves upward or downward depending on the value of yield constant. If one starts from an initial stress point (A), the shortest line to intersect this global minimum yield surface would be in the direction perpendicular to the slope of the yield surface, and the shortest distance would be the minimum yield constant.

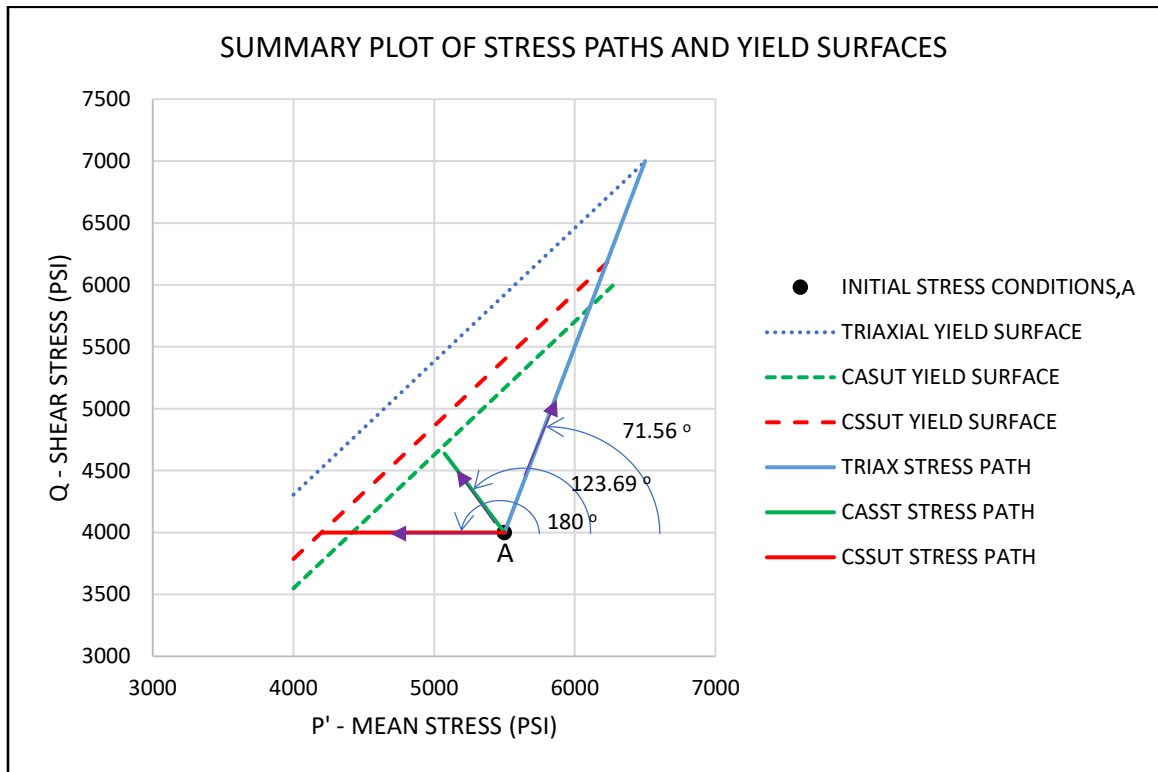


Figure 4-32 Shows the sample yielding behavior on different stress paths. The constant axial stress unloading test has the lowest yield surface while the triaxial loading stress path has the highest yield surface in this data set.

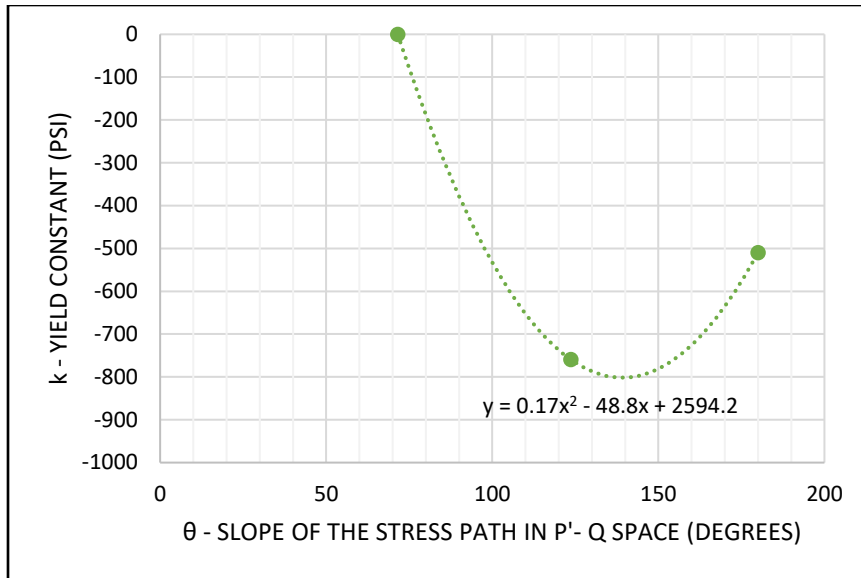


Figure 4-33 Shows the yield constant obtained from the yield surface plotted against the slope of the stress path angle.

Figure 4-33 shows a plot of the stress path angle and the yield constant. Since, the dependence of yield constant on stress path angle is observed to be non-linear, a parabolic curve fit is used. The minimum yield constant for this parabolic fit occurs when the first derivative is set to zero. The value of stress path angle for this point is about 138 deg. This is the same stress path angle obtained by drawing a perpendicular to the yield surface. The yield constant for this stress path angle - \sim (-800 psi) is the yield constant to accurately quantify the global minimum yield surface.

Thus, for a given initial condition, test sample traversing along a stress path with a slope of \sim 139 degrees in the p' - q space will yield at the global minimum yield surface. Therefore, for the material tested in this research work and within the bounds of the stress path slopes of -180 degrees (constant shear stress unloading) to +72 degrees triaxial loading), all yield surfaces are found to be parallel and the global minimum yield surface is found to intersect with a stress path of 140 degrees. The upper and lower bounds for these yield surfaces are the triaxial yield surface (\sim 72 deg) and the global minimum yield surface (\sim 138 deg), respectively.

With the above data defined, we want to predict the yield stress points for any stress paths at any initial stress points. We have represented the yield surface using a slope (m) and a yield constant (k) as:

$$q = mp' + k . \quad (4.4)$$

We now represent the stress path direction and the initial condition using the following equation:

$$(q - q_i) = \tan \theta * (p' - p'_i) , \quad (4.5)$$

where θ is the stress path angle, q_i is the initial shear stress and p_i is the initial mean effective stress. A test sample starting at the initial stress point (p_i, q_i) and traversing along a stress path with angle θ will hit the yield surface at the intersection of equations 4-4 and 4-5. To find the solution to this system of linear equations we express the yield constant as a function of stress path angle θ with experimental data (Figure 4-33):

$$k = f(\theta) = 0.17 * \theta^2 - 48.8 * \theta + 2594.2 . \quad (4.5)$$

The equation 4-5 can be rewritten as:

$$q = mp' + f(\theta) . \quad (4-6)$$

The solution to the equations 4-4 ad 4-6 will be the yield point with:

$$p' = \frac{(p'_i * \tan \theta) - q_i + f(\theta)}{\tan \theta - m} \quad (4.7)$$

and

$$q = \frac{(p'_i * m * \tan \theta) - (m * q_i) + (\tan \theta * f(\theta))}{\tan \theta - m} , \quad (4.8)$$

where p' is the yield mean effective stress, q is the yield shear stress, p'_i is the initial mean effective stress, q_i is the initial shear stress, m is the slope of the yield surface, and θ is stress path angle.

For the constant mean stress path where stress the path angle is 90 deg, the value of $\tan \theta$ is undefined. Therefore, using L'Hopital's rule, equation 4-7 reduces to:

$$p = p_i \quad (4.9)$$

and equation 4-8 reduces to

$$q = p_i * m + f(\theta) . \quad (4.10)$$

The equations 4-7 and 4-8 are the yield function equations. They can be used to calculate a yield point at any initial condition along any stress path angle.

To gauge the impact of differences in yield points for loading and unloading stress paths, eight yield points are calculated with different stress path angles using one initial conditions and the yield function. Table 4-3 shows the difference in calculated yield points from a triaxial loading path and from the yield function, with different stress path angle. Figure 4-34 highlights the differences in prediction of yield points from a conventional loading triaxial yield surface and the yield function. For the unloading phase, there is a stark contrast with loading surface overestimating the yield points by more than 37 %.

Therefore, the yield function generated yield surfaces should be used to calculate yield behavior of reservoir under unloading stress path.

Table 4-3 shows the calculated yield stresses for different stress path angles, the expected yield stress based on triaxial yield surface and difference between the two yield points.

	Stress path angle (Deg)	Actual yield stress (psi)		Expected yield stress (psi)		Difference (psi)	
		p'	q	p'	q	p'	q
Depletion	71.56	6743	7228	6743	7228	0	0
	80	5687	5897	5736	6174	49	276
	85	5295	5371	5326	5734	31	362
	90	5000	4959	5000	5382	0	423
Injection	100	4585	4348	4500	4843	-86	495
	130	3896	3315	3496	3763	-400	448
	150	3500	2865	2955	3181	-546	315
	180	2492	2000	1857	2000	-635	0

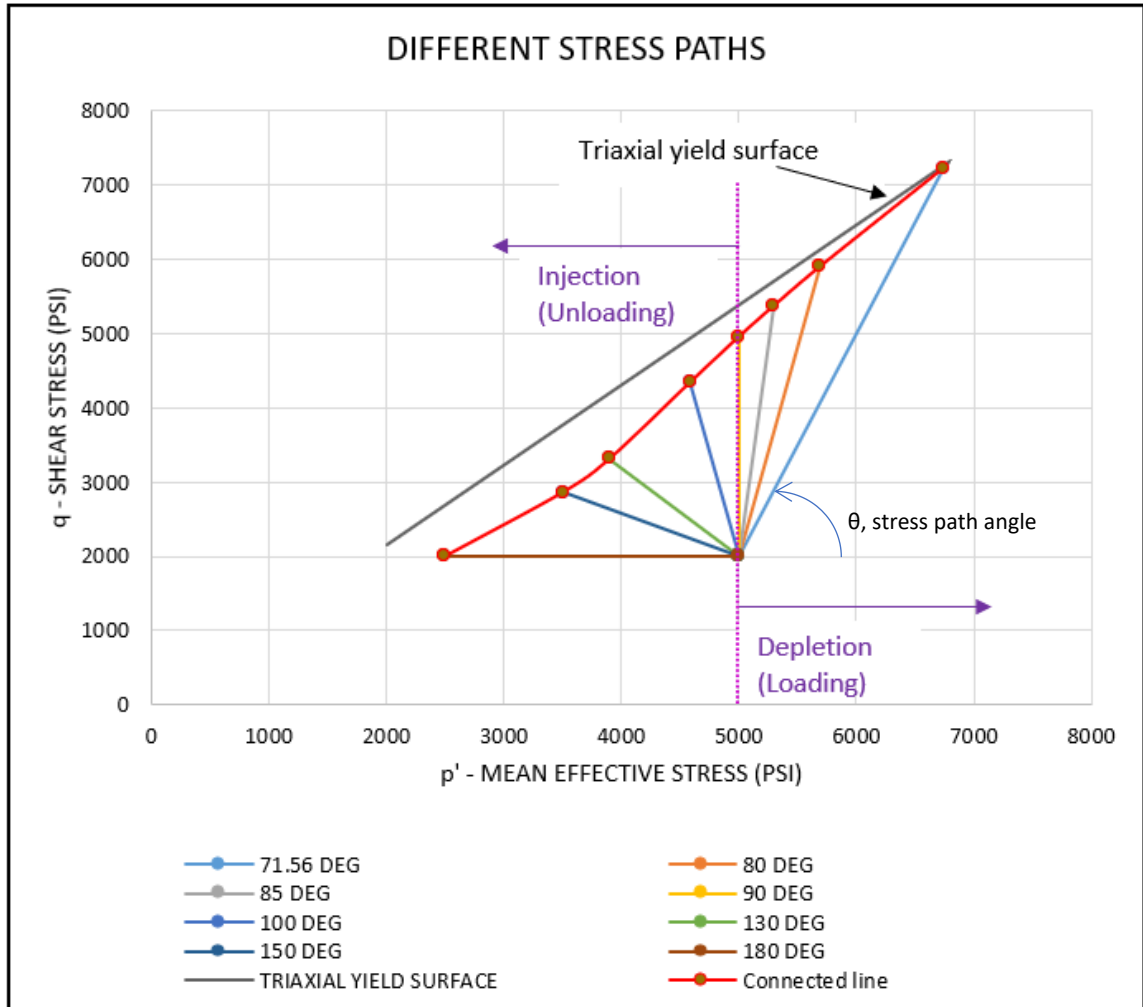


Figure 4-34 Shows the yield points calculated from the yield function along different stress path angles. The triaxial yield surface predicted yield points significantly overestimate those predicted from the yield function in the unloading phase by maximum of 37%.

4.4 Conclusions and Future Work

Stress magnitude and stress path dependence on the yield behavior of unconsolidated sands is presented. A suite of rock strength experiments was conducted to understand the yielding behavior under different stress paths. Yield surfaces were mapped in the effective mean stress – shear stress space for the different stress paths.

Following are the important conclusions –

- Yield surfaces for all three sets of experiments were found to be different, parallel with different values of yield constants.

- A minimum global yield surface model is proposed in this work. The material will yield at the global minimum yield surface if the stress path traversed is perpendicular to the yield surfaces.
- With two tests – one multi-stage triaxial test to determine the loading yield surface and one stress path to determine the minimum yield stress, in this specific order, we can bracket the upper and lower bounds for all yield surfaces.
- With the presented yield function, the yield point of this material at any initial condition (within bounds of p' and q are 2000 psi to 7000 psi) and all stress paths (within bounds - 180 deg to +72 deg) can be predicted.

Future work includes

- Validating the model with more stress paths and expanding the upper and lower bounds.
- Including different materials to study if similar behavior is observed.
- Building a global repository of different materials to quickly predict the yield stress of a material if the stress path is known.

5. COMBINED CONCLUSIONS AND FUTURE WORK

Importance of injection geomechanics on rock properties are of particular significance during any fluid injection process in multiple industries (nuclear waste disposal, secondary and tertiary recovery in oil and gas industry, geothermal energy, waste-water disposal etc.). The effect of injection on changing the minimum in-situ stress with pore pressure and on yielding behavior of unconsolidated sands was investigated using a suite of experiments on unconsolidated sands analogue test samples. A consistent and uniform sample preparation technique has been presented to prepare representative samples for the target sub-surface unconsolidated sands reservoir.

Changes in minimum in-situ stress with depletion and injection was quantified using horizontal stress path coefficients to simulate far field stresses in a laterally extensive reservoir (with no vertical stress arching). The horizontal stress path coefficient was lower on initial depletion stress paths compared to reload depletion and injection stress paths. Amount of hysteresis energy dissipated during the initial depletion – injection cycle to new depletion levels is about six times higher than the repeat depletion – injection cycle. Alteration of material properties and different Poisson's deformation induced horizontal stresses for injection and depletion explain the lower value of depletion coefficient. The alteration of material signified by movement of yield surface was quantified using Modified Cam Clay Material Model.

Effects of stress path direction on yield behavior was studied using three different stress paths - one loading based stress path direction and two unloading based path direction. The observed yield surfaces for three stress paths directions were different and parallel to each other with different yield constants in the mean effective stress – shear stress space. The yield behavior was found to be stress path direction dependent.

A global minimum yield surface model was proposed. Its slope is parallel to all other yield surfaces. The stress path direction that intersects this global minimum yield surface is at an angle perpendicular to the yield surface slope (of ~ 138 deg for our test specimen). The presented yield function in the previous section (equation 4-7 and 4-8) can be used to predict the yield points for any stress path (bounds of -180 deg to $+72$ deg) and at any initial test stress point (bounds of p' and q are 2000 psi to 7000 psi). This model can be interpolated within the bounds of stress paths tested in this work. Further validation with additional tests is required before it can be extrapolated outside the bounds of the tested conditions.

Future work involves performing tests for different boundary conditions to determine the variation in stress path coefficients for different materials. More tests should be performed to validate the bounds of the global minimum yield surface model outside the tested conditions. This methodology can be adopted to characterize more geo-materials of interest.

REFERENCES

1. Aadnoy, B. S., 1990. "Effects of Reservoir Depletion on Borehole Stability." *Journal of Petroleum Science and Engineering*. Vol. 6. PP. 57-61. [https://doi.org/10.1016/0920-4105\(91\)90024-H](https://doi.org/10.1016/0920-4105(91)90024-H)
2. Aadnoy, B. S., Bratli, R. K., and Lindholm, C. D. 1994. "In-situ Stress Modelling of the Snorre Field." *Society of Petroleum Engineers conference*. SPE 28138. <https://doi-org.ezproxy.lib.uh.edu/10.2118/28138-MS>.
3. Aadnoy, B. S., and Hansen, A. K. 2005. "Bounds on In-Situ Stress Magnitudes Improve Wellbore Stability Analyses." *Society of Petroleum Engineers Journal* 10. <https://doi-org.ezproxy.lib.uh.edu/10.2118/87223-MS>
4. Abdallah, K.B, Hamoud, M. and Chalaturnyk, R., 2014. "Experimental Studies of Shear Induced in Single Phase Permeability." *Society of Petroleum Engineers Heavy Oil Conference- Canada*. SPE 170136-MS. <https://doi-org.ezproxy.lib.uh.edu/10.2118/170136-MS>
5. Addis, M. A., 1997. "The Stress Depletion Response of Reservoirs." *Society of Petroleum Engineers conference*. SPE 38720. <https://doi-org.ezproxy.lib.uh.edu/10.2118/38720-MS>
6. Ali, H. S., Al-Marhoun, M. A., Abu-Khamsin, S. A., and Celik, M. S. 1987. "The Effect of Overburden Pressure on Relative Permeability." *Society of Petroleum Engineers Journal*, SPE 15730. <https://doi-org.ezproxy.lib.uh.edu/10.2118/15730-MS>
7. Al-Salman, M. E., Myers, M. T., and Sharf-Aldin, M. H., 2015. "Comparison of Multistage to Single Stage Triaxial Tests." *U.S. Rock Mechanics/Geomechanics Symposium*. ARMA 15-767

8. Arya, A., 2018. "Studying the Effect of Preconsolidation Stress on Stress-Strain Behaviour of Sands." M.Sc. Thesis, University of Houston, Houston. <http://hdl.handle.net/10657/3603> .
9. Barla, M., 2007. "Numerical Simulation of the Swelling Behavior Around Tunnels Based on Special Tri-axial Tests." *Tunneling and Underground Space Technology*. Vol. 23, PP. 508-521. <https://doi.org/10.1016/j.tust.2007.09.002>
10. Bilal, A., Myers, M., and Hathon, L., 2016. "An Investigation of Static and Dynamic Data Using Multistage Triaxial Tests." *Society of Exploration Geophysicists conference*. SEG 16-13969660. <https://doi.org/10.1190/segam2016-13969660.1>
11. Bin, W., Jie-Bing, Z., Ai-Qing, W., and Zan-Ming, X., 2008. "Confining Pressure Unloading with Axial Force Fixed Tests on Marble and Its Time-Effect Property Study." *International Society for Rock Mechanics and Rock Engineering*. ISRM-ARMS5-2008-019
12. Biot, M.A., 1941. "General Theory of Three-Dimensional Consolidation." *Journal of Applied Physics*. Vol. 12, PP. 155-164. <https://doi.org/10.1063/1.1712886>
13. Biot, M.A., 1962. "Mechanics of Deformation and Acoustic Propagation in Porous Media." *Journal of Applied Physics*. Vol. 33, PP. 1482–1498. <https://doi.org/10.1063/1.1728759>
14. Bjorlykke, K. 2010. Petroleum Geoscience – From Sedimentary Environments to Rock Physics. Ch 11. PP. 311-318
15. Borja, R. I., and Lee, S. R., 1990. "Cam-Clay Plasticity, Part 1: Implicit Integration of Elasto-Plastic Constitutive Relations." *Computer Methods in Applied Mechanics and Engineering*, 78(1), 49-72. [https://doi.org/10.1016/0045-7825\(90\)90152-C](https://doi.org/10.1016/0045-7825(90)90152-C)

16. Bouteica, M. J., Sarda, J., and Vincke, O., 2000. "Constitutive Law for Permeability Evolution of Sandstones During Depletion." *Society of Petroleum Engineers conference*. SPE 58717. <https://doi-org.ezproxy.lib.uh.edu/10.2118/58717-MS>
17. Breckels, I. M., and Eekelen, H. A. M., 1982. "Relationship Between Horizontal Stress and Depth in Sedimentary Basins." *Journal of Petroleum Technology*. Vol. 34. PP. 2191-2199. <https://doi.org/10.2118/10336-PA>
18. Bree, P. D., and Walters, J. V., 1989. "Micro/Minifrac Test Procedures and Interpretation for In-Situ Stress Determination." *International Journal of Rock Mechanics and Mining Sciences*. Vol. 26. PP. 515-521. [https://doi.org/10.1016/0148-9062\(89\)91429-0](https://doi.org/10.1016/0148-9062(89)91429-0)
19. Brignoli, M., and Federico, A. D., 2004. "Compaction of Unconsolidated Sands and Stress Path Effects: Laboratory Evidence." *U.S. Rock Mechanics/Geomechanics Symposium*. ARMA 04-615
20. Cai, M., Su, Y., Elsworth, D., Hao, Y., and Gao, X., 2020. "A New Coupled Geomechanical-Chemical Model for CO₂ Foam Flooding and Storage in Tight Reservoir." *Unconventional Resources Technology Conference*. <https://doi-org.ezproxy.lib.uh.edu/10.15530/urtec-2020-3329>
21. Chalaturnyk, R. J., 1996. Geomechanics of the Steam Assisted Gravity Drainage Process in Heavy Oil Reservoirs. PhD Thesis. University of Alberta. <https://doi.org/10.7939/R39W0971Z>
22. Chan, A. W., Hagin, P. N., and Zoback, M. D., 2004. "Viscoplastic deformation, stress and strain paths in unconsolidated reservoir sands (part 2): Field Applications using dynamic DARS analysis." *U.S. Rock Mechanics/Geomechanics Symposium*. ARMA 04-568

23. Chen, W. Z., Liu, D., and Yang, J., 2008. "Power Function Based Mohr Strength Criterion for Marble with Unloading Confining Pressures." *Chinese Journal of Rock Mechanics and Engineering*. Vol 11(27). PP. 2214-2220.
24. Chen, S. L., and Abousleiman, Y. N. 2016. "An Analytical Solution for Wellbore Stability Problem Using Strain Hardening Drucker-Prager Plasticity Model." *U.S. Rock Mechanics/Geomechanics Symposium*. ARMA-2016-643
25. Chin, R. Y., 1997. "Model Prediction of Stress-Strain Behavior on Cohesionless Soil." *International Society of Offshore and Polar Engineering Conference*. ISOPE-I-97-130
26. Crawford, A., & Wylie, D. 1987. "A Modified Multiple Failure Triaxial Testing Method." *Symposium of Rock Mechanics*, 133-140
27. Dai, B., Zhao, G. Y., Yang, C., & Dong, L. J., 2014. "Experimental of Unloading Mechanical Properties of Rock Under Different Stress Paths." *International Society for Rock Mechanics and Rock Engineering*. ISRM-YSS-2014-021
28. Davison, J. M., Foo, I., Ellis, F. and Proughten, A., 2016. "The In-Situ Stress Response of Reservoirs to Pressure Reduction Followed by Pressure Increase: Depletion and Rebound Stress Paths from Two Case Studies." *American Rock Mechanics Association Symposium*. ARMA 16-281.
29. Dessouki, M., Myers, M. T., and Hathon, L. A., 2020. "A New Approach to Calibrate the Modified Cam Clay Model by Using Multi-Stage Triaxial Tests on Resedimented Mudrocks." *U.S. Rock Mechanics/Geomechanics Symposium*. ARMA-2020-1558.
30. Dobrynin, V. M. 1962. "Effect of Overburden Pressure on Some Properties of Sandstone." *Society of Petroleum Engineers Journal*. PP 360-366.
<https://doi.org/10.2118/461-PA>

31. Du, K., Li, X., Li, D., and Weng, L., 2015. "Failure Properties of Rocks in True Triaxial Unloading Compressive Test." *Transactions of Nonferrous Metals Society of China*. Vol. 25(2). PP. 571-581. [https://doi.org/10.1016/S1003-6326\(15\)63639-1](https://doi.org/10.1016/S1003-6326(15)63639-1)
32. Eaton, B. A., 1972. "The Effect of Overburden Stress on Geopressure Prediction from Well Logs." *Journal of Petroleum Technology*, Vol. 24. PP. 929-934. <https://doi-org.ezproxy.lib.uh.edu/10.2118/3719-PA>
33. Fjær, E., Holt, R., Horsrud, P., Raaen, A., and Risnes, R., 2008. Petroleum Related Rock Mechanics. 2nd ed., Elsevier. PP. 1 – 93. ISBN: 978-0-444-50260-5
34. Folkes, D. J., and Crooks, J. H. A., 1985. "Effective Stress Paths and Yielding in Soft Clays Below Embankments." *Canadian Geotechnical Journal*. Vol. 22. PP. 357-374. <https://doi.org/10.1139/t85-048>
35. Fung, Y. C., 1994. A First Course in Continuum Mechanics for Physical and Biological Engineers and Scientists. Prentice Hall Press. PP. 64-111. ISBN: 978-0130615244
36. Gao, F., Zhou, K., Luo, X., and Zhai, J., 2012. "Effect of Induction Unloading on Weakening of Rock Mechanics Properties." *Transactions of Non-ferrous Metals Society of China*. Vol. 22. PP. 419-424
37. Gao, Q., and Ghassemi, A. 2020. "Height Growth in Layered Unconventional Reservoirs: The Impact of Formation Moduli, Interfaces, and In-Situ Stress." *Society of Petroleum Engineers Production and Operations*. Vol 35. PP. 0756-0774. <https://doi.org/10.2118/201104-PA>
38. Gjonnes, M., Cruz, M. G. L., Horsrud, P. and Holt, R. M., 1998. "Leak off Tests for Horizontal Stress Determination." *Journal of Petroleum Science and Engineering*. Vol. 20. PP. 63-71. [https://doi.org/10.1016/S0920-4105\(97\)00053-3](https://doi.org/10.1016/S0920-4105(97)00053-3)

39. Gomes, D. G. O., and Villalobos, J. F. C. 2014. "Automating a Comprehensive Methodology for Evaluation, Selection, and Sizing of Sand Control Methods in Fields with Sand Problems – A Case Study." *Society of Petroleum Engineers* conference. SPE 169380. [https://doi.org/10.1016/S0920-4105\(97\)00053-3](https://doi.org/10.1016/S0920-4105(97)00053-3)
40. Gray, D., Fatt, I., and Bergamini, G. 1963. "The Effect of Stress on Permeability of Sandstone Cores." *Society of Petroleum Engineers Journal*. PP. 95-100. <https://doi.org/10.2118/531-PA>
41. Guerra, J.J., Velez, E.I., and Vasquez., C., 2012. "Hydraulic Fracture Design and Geomechanical Model Validation Using Sonic Scanner and Microseismic Measurements in Baco-1 Well." *Society of Petrophysicists and Well Log Analysts Symposium*. SPWLA-2012-240
42. Guglielmi, Y. G., Henry, P., Nussbaum, C., Dick, P., Gout, C., and Amann, F. 2015. "Underground Research Laboratories for Conducting Fault Activation Experiments in Shales." *U.S. Rock Mechanics/Geomechanics Symposium*. ARMA-2015-480
43. Guo, Y., Yang, C., and Fu, J., 2012. "Experimental Research on Mechanical Characteristics of Salt Rock Under Triaxial Unloading Test." *Yantu Lixue/Rock and Soil Mechanics*. Vol. 3(3). <https://doi.org/10.1155/2018/1670180>
44. Guo, H., Ji, M., Zhang, Y. and Zhang, M. 2018. "Study of Mechanical Property of Rock under Uniaxial Cyclic Loading and Unloading." *Advances in Civil Engineering*. Article 1670180. <https://doi.org/10.1155/2018/1670180>
45. Hamoud, M. 2012. "Influence of Geomechanical Processes on Relative Permeability." MSc. Thesis, University of Alberta, Edmonton, Alberta. <https://doi.org/10.7939/R3ZQ62>

46. Han, H. X., and Yin, S., 2018. "Determination of In-situ Stress and Geomechanical Properties from Borehole Deformation." *Energies*. Vol. 11. PP. 131-143.
<https://doi.org/10.3390/en11010131>
47. He, M. C., Miao, J. L. and Feng, J. L., 2010. "Rock Burst Process of Limestone and its Acoustic Emission Characteristics Under True Triaxial Unloading Conditions." *International Journal of Rock Mechanics and Mining Sciences*. Vol. 47(2). PP. 286-298.
<https://doi.org/10.1016/j.ijrmms.2009.09.003>
48. Hettema, M. H. H., Schutjens, P. M. T. M., Verboom, B. J. M., and Gussinklo, H. J., 2000. "Production Induced Compaction of Sandstone Reservoir: The Strong Influence of Stress Path." *Society of Petroleum Engineers Reservoir Evaluation Eng.* 3. PP. 342-347.
<https://doi-org.ezproxy.lib.uh.edu/10.2118/65410-PA>
49. Holt, A. M., and Fjaer, E. 1991. "Validity of Multiple Failure State Triaxial Tests in Sandstones." 7th ISRM Congress. ISRM-7CONGRESS-1991-102
50. Holt, R. M., Gheibi, S., and Lavrov, A., 2016. "Where Does the Stress Path Lead? Irreversibility and Hysteresis in Reservoir Geomechanics." *U.S. Rock Mechanics/Geomechanics Symposium*. ARMA 16-496.
51. Huang, D., and Li, Y., 2014. "Conversion of Strain Energy in Triaxial Unloading Tests on Marble." *International Journal of Rock Mechanics and Mining Sciences*. Vol 66. PP. 160 - 168. <https://doi.org/10.1016/j.ijrmms.2013.12.001>
52. Huang, R., Wang, X. and Chan, L., 2001. "Triaxial unloading test of rocks and its implication for rock burst." *Bulletin of Engineering Geology and Environment*. Vol. 60. PP. 37-41. <https://doi.org/10.1007/s100640000082>
53. Huang, W., Wen, K., Liu, D., Dong, Q., Li, J., Li, Y., and Li, L., 2020. "Experimental Study on Influence of Excess Pore Water Pressure and Unloading Ratio on Unloading Mechanical

- Properties of Marine Sedimentary Soft Soils.” *Ocean Engineering* 195. 106680.
<https://doi.org/10.1016/j.oceaneng.2019.106680>
54. Hughson, D. R. and Crawford, A. M. 1987. Kaiser Effect Gauging: “The Influence of Confining Stress On its Response.” *ISRM congress*. ISRM-6CONGRESS-1987-181
55. Ivory, J., W.D. Gunter, P. Mikkelsen, K.N. Chhom, J. Hruschak, and B. Tilley, 1987. “Development and Testing of a Synthetic Cold Lake Oil Sand.” *Journal of Canadian Petroleum Technology*, Vol.26(3): PP. 48-53. <https://doi-org.ezproxy.lib.uh.edu/10.2118/87-03-05>
56. Jambunathan, V., 2008. “Study of Mechanical Properties of Carbonates.” M.Sc. Thesis, University of Oklahoma.
57. Jimenez, B. L., Yu, G., Aguilera, R., and Settari, A., 2015. “Calibration of Well Logs with Mini-Frac Data for Estimating the Minimum Horizontal Stress in the Tight Gas Monteith Formation of the Western Canada Sedimentary Basin : A Case Study.” *Society of Petroleum Engineers Production and Operations*. Vol. 30. PP. 110-120. <https://doi-org.ezproxy.lib.uh.edu/10.2118/168594-PA>
58. Kaiser, H. 1953. “Erkenntnisse und folgerungen aus der messing von gerauschen bie zugbeanspruchung von metallischen werstoffen.” *Archiv fur das Eisenhüttenwesen*. Vol. 24. PP. 43-45.
59. Kim, M. M., & Ko, H. Y., 1979. “Multistage Triaxial Testing of Rocks.” *Geotechnical testing journal*, Vol. 2 (2), 98-105. <https://doi.org/10.1520/GTJ10435J>
60. Kovari, K., and Tisa, A., 1975. “Multiple Failure State and Strain Controlled Triaxial Tests.” *Rock Mechanics and Rock Engineering*, Vol.7, Issue 1, Springer, 17-33.
<https://doi.org/10.1007/BF01239232>

61. Kry, P. R., and Gronseth., J. M. 1983. "In-situ Stresses and Hydraulics Fracturing in the Deep Basin." *Journal of Canadian Petroleum Technology*. Vol 22. <https://doi-org.ezproxy.lib.uh.edu/10.2118/83-06-02>
62. Kuerbis, R., and Vaid, Y.P., 1988. "Sand sample preparation – The Slurry Deposition Method." *Soils and Foundations*, Vol. 28, No. 4, PP.107-118. https://doi.org/10.3208/sandf1972.28.4_107
63. Lade, P. V., and Duncan, J. M., 1976. "Stress-Path Dependent Behavior of Cohesionless Soil." *Journal of the Geotechnical Engineering Division*. <https://doi.org/10.1061/AJGEB6.0000235>
64. Lambe, T.W., 1967. "Stress Path Method." *Journal of Soil Mechanics and Foundation Division*. ASCE. Vol. 93. PP. 309-331. <https://doi.org/10.1061/JSFEAQ.0001058>
65. Landau, L. D., and Lifshitz, E. M., 1986. Theory of Elasticity. 3rd ed. Pergamon Press.
66. Lavrov, A., 2016. Lost Circulation: Mechanisms and Solutions. Oxford. Elsevier. Ed. 1
67. Li, D., Sun, Z., Xie, T., Li, X., and Ranjith, P. G., 2017. "Energy Evolution Characteristics of Hard Rock During Triaxial Failure with Different Loading and Unloading Paths." *Engineering Geology*. Vol. 228. PP. 270-281. <https://doi.org/10.1016/j.enggeo.2017.08.006>
68. Liu, Q., Cheng, Y., Jin, K., Tu, Q., Zhao, W., and Zhang, R., 2017. "Effect of Confining Pressure Unloading on Strength Reduction of Soft Coal in Borehole Stability Analysis." *Environmental Earth Sciences*. Vol.76, A. 173. <https://doi.org/10.1007/s12665-017-6509-9>
69. Liu, Y., Liu, L., Leung, J. Y., Wu, K., and Moridis, G., 2021. "Coupled Flow/Geomechanics Modeling of Interfracture Water Injection to Enhance Oil Recovery in Tight Reservoirs."

- Society of Petroleum Engineers Journal*. Vol. 26. PP. 1-21. <https://doi-org.ezproxy.lib.uh.edu/10.2118/199983-PA>
70. Louis, L., Henck, S., Honarpour, M., Araujo, E., and Bryant, D., 2018. "Experimental Study on the Hydromechanical Behavior of a Gulf of Mexico Reservoir Sand analogue at In-situ Conditions of Pressure and Temperature." *U.S. Rock Mechanics/Geomechanics Symposium*. ARMA 18-1339
71. Mavko, G., Mukherji, T., and Dvorkin, J., 1998. The Rock Physics Handbook. Cambridge University Press. PP. 17 – 48. <https://doi.org/10.1017/CBO9780511626753>
72. Mostafavi, V., Cramer, D. D., and Hossini, A. H., 2020. "Improved In-Situ Stress Characterization Through Analysis of Diagnostic Fracture Injection Tests DFITs Using the Changing Compliance Method and Its Impact on Caprock Integrity Analysis." *Society of Petroleum Engineers Canada Heavy Oil Conference*. <https://doi-org.ezproxy.lib.uh.edu/10.2118/199924-MS>
73. Nian, T., Wang, G., Xiao, C., Zhou, L., Deng, L., and Li., R., 2016. "The In-Situ Stress Determination from Borehole Image Logs in the Kuqa Depression." *Journal of Natural Gas Science and Engineering*. Vol. 34. PP. 1037-1084. <https://doi.org/10.1016/j.jngse.2016.08.005>
74. Nolen-Hoeksema, R.C., Avasthi, J. M., Pape, W. C., and El-Rabaa, A. W. M. 1994. "Waterflood Improvement in the Permian Basin: Impact of In-Situ Stress Evaluations." *Society of Petroleum Engineers Reservoir Engineering*. Vol 9. PP. 254-260. <https://doi-org.ezproxy.lib.uh.edu/10.2118/24873-PA>.
75. Oldakowski, K., 1994. "Stress Induced Permeability Changes in Athabasca Oil Sands." M.Sc. Thesis, University of Alberta. <https://doi.org/10.7939/R33R0Q21F>

76. Pagoulatos, A., 2004. "Evaluation of Multistage Triaxial Testing on Berea Sandstone." M. S. Thesis. University of Oklahoma. <https://hdl.handle.net/11244/323808>
77. Perkins, T. K., and Gonzalez, J. A., 1984. "Changes in Earth Stresses Around a Wellbore Caused by Radially Symmetrical Pressure and Temperature Gradients." *Society of Petroleum Engineering Journal*. Vol. 24. PP. 129-140. <https://doi-org.ezproxy.lib.uh.edu/10.2118/10080-PA>
78. Polikar, M., V.R. Puttagunta, F. Ferracuti, and S.M. Farouq Ali, 1988. "Preparation of synthetic oil sand cores." *Journal of Petroleum Science and Technology*, 1(1988) 263-270. [https://doi.org/10.1016/0920-4105\(88\)90001-0](https://doi.org/10.1016/0920-4105(88)90001-0)
79. Prakash, S., Myers, M. T., and Hathon, L. A., 2018. "Analysis of Damage Induced During a Multi-Stage Triaxial Test Using Acoustic Emissions." *U.S. Rock Mechanics/Geomechanics Symposium*. ARMA 18-1223
80. Predein, A., and Klykov, P., 2015. "Geomechanical Model and Borehole Stability Prediction for One of the Fields of Perm Region." *Society of Petroleum Engineers Russian Petroleum Technology Conference*. <https://doi-org.ezproxy.lib.uh.edu/10.2118/176736-MS>
81. Rafieepour, S., MIska., S. Z., Ozbayoglu, E., Yu, M., Takach, N. E., Zhang, J., and Majidi, R., 2017. "Experimental Study of Reservoir Stress Path and Hysteresis During Depletion and Injection Under Different Deformational Conditions." *U.S. Rock Mechanics/Geomechanics Symposium* ARMA 17-416
82. Rhett, D. W., and Teufel, L. W., 1992. "Effect of Reservoir Stress Path on Compressibility and Permeability of Sandstones." *Society of Petroleum Engineers conference*. SPE 24756. <https://doi.org/10.2118/24756-MS>

83. Riazi, M. R. 2016. ASTM International Manual – Exploration and Production of Petroleum and Natural Gas. Ch. 4. PP. 83-107
84. Roscoe, K. H., and Burland, J. B., 1968. “On the Generalized Stress-Strain Behavior of Wet Clay.” Engineering Plasticity. Cambridge University press. PP. 535-609. <https://doi.org/10.1016/0022-4898%2870%2990160-6>
85. Santarelli, F. J., Tronvoll, J. T., Svennekjaer, M., Skeie, H., Henriksen, R., and Bratli, R. K., 1998. “Reservoir Stress Path: Depletion and Rebound.” *SPE/ISRM 47350 EUrock Symposium*. Vol 2. PP. 203-209. <https://doi.org/10.2118/47350-MS>
86. Schutjens, P., HIndriks, K., and Myers, M., 2008. “Depletion-Induced Reservoir Compaction: Two Geomechanical Models and Their Application in the Planning of Subsidence Monitoring.” *U.S. Rock Mechanics/Geomechanics Symposium*. ARMA 08-247
87. Scott, J. D., Proskin, S. A., and Adhikary, D. P. 1994. “Volume and Permeability Changes Associated with Steam Stimulation in an Oil Sands Reservoir.” *Journal of Canadian Petroleum Technology*. JCPT 94-07-06. <https://doi.org/10.2118/94-07-06>
88. Shlyapobersky, J., Walhaug, W. W., Sheffield, R. E., and Huckabee, P. T. 1988. “Field Determination of Fracturing Parameters for Overpressure Calibrated Design of Hydraulic Fracturing.” *Society of Petroleum Engineers Conference*. SPE 18195. <https://doi.org/10.2118/18195-MS>
89. Sinha, B. and Wendt, A. S., 2015. “Estimation of Horizontal Stress Magnitudes Using Sonic Data from Vertical and Deviated Wellbores in a Depleted Reservoir.” *Geological Society London Special Publications*. Vol. 409. PP. 67-91. <http://dx.doi.org/10.1144/SP409.9>
90. Skomedal, E., Jostad, H. P., Hettema, M. H., 2002. “Effect of Pore Pressure and Stress Path on Rock Mechanical Properties for HPHT Application.” *U.S. Rock Mechanics/Geomechanics Symposium*. ISRM 78152. <https://doi.org/10.2118/78152-MS>

91. Soriede, O. K., Hansen, S., and Stenebraten, J., 2014. "Estimation of Reservoir Stress Effects Due to Injection of Cold Fluids: An Example From NCS." *U.S. Rock Mechanics/Geomechanics Symposium*. ARMA 14-7394

92. Taheri, A., and Tani, K., 2008. "Proposal of A New Multiple Step Loading Triaxial Compression Testing Method." *5th Asian Rock Mechanics Symposium*. ISRM-ARMS5-2008-058.

93. Thombare, A., Gokaraju, D. V., Mitra, A., Govindarajan, S., Guedez, A., and Aldin, M. 2020. "Mitigation of Sand Production and Estimation of In-Situ Stress Orientation – An Experimental Investigation." *ARMA International Geomechanics Symposium*. ARMA-IGS-20-076.

94. Touhidi, B., A., 1998. "Absolute Permeability of McMurray Formation Oil Sands at Low Confining Stresses." PhD Thesis, University of Alberta. <https://doi.org/10.7939/R3Z31P07M>.

95. Wang, H., Chen, W., Tan, X., Tian, H., and Cao, J., 2012. "Development of a New Type of Foam Concrete and its Application on Stability Analysis of Large-Span Soft Rock Tunnel." *Journal of Central South University*. Vol. 19, PP. 3305–3310.

96. Wang, S., Xu, W., Yan, L., Feng, X., Xie, W., and Chen, H., 2020. "Experimental Investigation and Failure Mechanism Analysis for Dacite Under True Triaxial Unloading Conditions." *Engineering Geology*. Vol. 264. A. 105407. <https://doi.org/10.1016/j.enggeo.2019.105407>

97. Wang, X., Chalaturnyk, R., Huang, H., and Leung, J., 2015. "Permeability Variations Associated with Various Stress States During Pore Pressure Injection." *U.S. Rock Mechanics/Geomechanics Symposium*. ARMA 15-0768

98. Wood D. M., 1990. Soil Behavior and Critical State Soil Mechanics. Cambridge University Press. PP. 112-125. <https://doi.org/10.1017/CBO9781139878272>
99. Xie, H. Q., and He, C. H., 2004. "Study of the Unloading Characteristics of a Rock mass Using the Triaxial Test and Damage Mechanics." *International Journal of Rock Mechanics and Mining Sciences*. Vol. 41. Paper 1A 13. <https://doi.org/10.1016/j.ijrmms.2004.03.022>
100. Yale, D. P., and Ryan, T. C. 1994. "In-Situ Stress and Hydraulic Fracture Orientation in the Mid-Continent Area." *U.S. North American Rock Mechanics Symposium*. ARMA-1994-0393
101. Yale, D. P., Mayer, T., and Wang, J., 2010. "Geomechanics of Oil Sands Under Injection." *U.S. Rock Mechanics/Geomechanics Symposium*. ARMA 10-257.
102. Yin, Z., Li, X., Jin, J., He, X., and Du, K., 2012. "Failure Characteristics of High Stress Rock Induced by Impact Disturbance Under Confining Pressure Unloading." *Transactions of Nonferrous Metals Society of China*. Vol. 22. PP. 175-184. [https://doi.org/10.1016/S1003-6326\(11\)61158-8](https://doi.org/10.1016/S1003-6326(11)61158-8)
103. Younessi, A., Gui, F., Guises, R., Ngan, A., Nadzri, S., and Zhou, C., 2018. "Evaluation of Reservoir Compaction and Geomechanical Related Risks Associated with Reservoir Production Using a Two-Way Coupled 3D Geomechanical Model for a Deep-Water Field in South East Asia." *Offshore Technology Conference Asia*. <https://doi-org.ezproxy.lib.uh.edu/10.4043/28227-MS>
104. Zhang, J. 2020. Applied Petroleum Geomechanics. Gulf Professional Publishing. PP. 2-8. ISBN: 978-0128148150

105. Zhang, X., Zhang, D., and Leo, C., 2017. "Damage Evolution and Post-peak Gas Permeability of Raw Coal Under Loading and Unloading Conditions." *Transport in Porous Media*. Vol. 117(99). PP. 1-16. <https://doi.org/10.1007/s11242-017-0842-z>
106. Zhou, Q., 2013. "Tests and Test Methods of Unloading Strength of Soft soil." *Journal of Yangtze River Science Research Institute*. Vol. 30(3). PP. 35-39. <https://doi.org/10.1016/j.ijrmms.2019.01.003>
107. Zhu, T., and Huang, D., 2019. "Experimental Investigation of the Shear Mechanical Behavior of Sandstone Under Unloading Normal Stress." *International Journal of Rock Mechanics and Mining Sciences* 114. PP. 186-194
108. Zillur, R., Al-Qahtani, M. Y., Bartko, K. M., Goodman, H., Hilarides, W.K., and Norman, W. D., 2003. "The Role of Geomechanical Earth Modeling in the Unconsolidated Pre-Khuff Field Completion Design for Saudi Arabian Gas Wells." *Society of Petroleum Engineers Conference*. <https://doi-org.ezproxy.lib.uh.edu/10.2118/84258-MS>
109. Zoback, M. D., and Zinke, J. C., 2002. "Production-Induced Normal Faulting in the Valhall and Ekofisk Oil Fields." *Pure and Applied Geophysics*. 159. PP. 403-420. <https://doi.org/10.1007/PL00001258>
110. Zoback, M. D. 2007. Reservoir Geomechanics. Cambridge University Press.

6. APPENDIX 1 – MODIFIED CAM CLAY (MCC) MODEL

The ability of a material to deform permanently under applied stress is called plasticity. The irrecoverable physical deformation that remains after load is removed is called plastic deformation. A material is yielding when the stress-strain behavior can no longer be expressed by Hooke's Law. To describe the deformational response of the material under load up to and beyond yielding, an elasto-plastic model is used. This model captures the elastic response up to the yield point and then perfectly plastic response beyond it. (Wood, 1990). Following ingredients are required to build an elasto-plastic constitutive model:

- Description of elastic behavior – elastic properties,
- Initiation of plastic deformational behavior – yield surface criterion,
- Mechanism of plastic deformation – plastic potential,
- Magnitude of plastic deformation – hardening rule.

The Modified Cam Clay model or MCC model is an example of an elasto-plastic model (Roscoe et al., 1968). The model predicts values of both - incremental elastic strain and incremental plastic strain, with changes in stress invariant values.

The model is expressed in terms of an effective mean stress- shear stress plot (Figure 6-1). Effective mean stress is expressed as a function of the first invariant of the principal stress tensor. The first invariant of the principal stress tensor is

$$I_1 = \sigma_1 + \sigma_2 + \sigma_3 . \quad (6.1)$$

The mean effective stress is expressed as a function of the first invariant:

$$p' = \left(\frac{I_1}{3} \right) . \quad (6.2)$$

Shear stress is expressed as a function of the second invariant of the stress deviation tensor as:

$$q = \sqrt{3J_2}. \quad (6.3)$$

The second invariant of the stress deviation tensor (Fung, 1994) is

$$J_2 = \frac{1}{2} \left[\left(\sigma_1 - \frac{I_1}{3} \right)^2 + \left(\sigma_2 - \frac{I_1}{3} \right)^2 + \left(\sigma_3 - \frac{I_1}{3} \right)^2 \right]. \quad (6.4)$$

The yield surface is defined by two parameters, namely – critical state line with slope M and maximum isotropic consolidation stress P_0 . For triaxial conditions,

$$q = (\sigma_1 - \sigma_3) \quad (6.5)$$

and

$$p' = \left(\frac{\sigma_1 + 2\sigma_3}{3} \right). \quad (6.6)$$

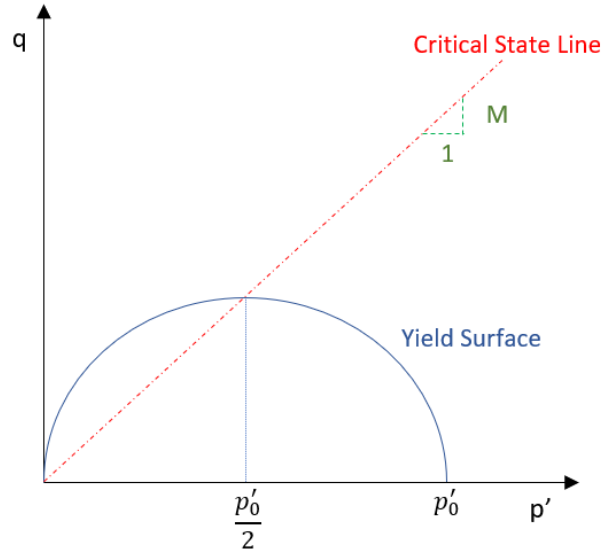


Figure 6-1 A graphical representation of MCC model with its yield surface, critical state line and maximum consolidation stress in a mean stress - shear stress plot.

The slope of the critical state line is M . The critical state line is expressed as:

$$q = Mp' . \quad (6.7)$$

p_0 is the maximum value of consolidation stress experienced by the specimen. The yield surface equation is in the form of an ellipse. The critical state line intersects the yield surface with an effective mean stress value of 50% of the maximum isotropic consolidation stress.

The yield surface is expressed in terms of shear stress - q , mean effective stress - p' , and consolidation stress - p_0 . (Borja, 1990) as:

$$f[q, p', p_0] = q^2 - M^2 p' (p'_0 - p') = 0 . \quad (6.8)$$

The total strain can be linearly separated into its component elastic and plastic strain.

Total volume strain is expressed as (Chin, 1997):

$$\partial \varepsilon_v = \partial \varepsilon_v^e + \partial \varepsilon_v^p \quad (6.9)$$

and the total shear strain is expressed as:

$$\partial \varepsilon_s = \partial \varepsilon_s^e + \partial \varepsilon_s^p . \quad (6.10)$$

The model assumes that strain is purely elastic inside the yield surface and plastic strain start accumulating at the yield surface.

When soft soil undergoes isotropic compression, the specific volume is related to the consolidation stress (Figure 6-2). Specific volume is defined as

$$v = 1 + e \quad (6.11)$$

or

$$v = \frac{1}{1-\phi}, \quad (6.12)$$

where e is void ratio and ϕ is porosity.

The relationship between specific volume and consolidation stress (Figure 6-2) on the compaction curve is as follows:

$$v = \frac{1}{1-\phi} = v_c - \lambda \ln p_0 \quad (6.13)$$

and on the swelling curve is

$$v = \frac{1}{1-\phi} = v_s - \kappa \ln p_0 . \quad (6.14)$$

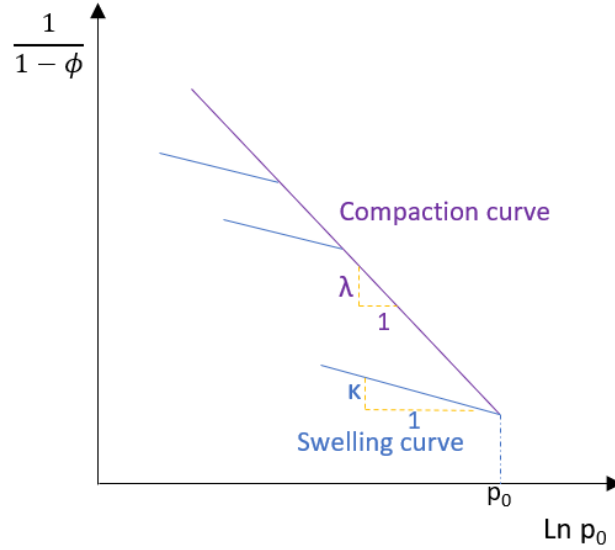


Figure 6-2 A graphical representation of compaction and swelling curve. The slopes λ and κ are calculated from these curves.

The material behavior is predicted through volume strain and shear strain. The elastic part of these strains is derived from the swelling curve. In the elastic region, the amount of volume strain is assumed to be equal to the amount of change in porosity. The elastic volume strain and shear strain are:

$$\begin{bmatrix} \delta \varepsilon_v^e \\ \delta \varepsilon_s^e \end{bmatrix} = \begin{bmatrix} \frac{\kappa(1-\phi)}{p'} & 0 \\ 0 & \frac{1}{3G} \end{bmatrix} \begin{bmatrix} \partial p' \\ \partial q \end{bmatrix}. \quad (6.15)$$

For calculating plastic strains, we define a plastic potential. The plastic potential χ relates plastic strain matrix to the stress matrix. The parameter g is scalar function which, when differentiated with respect to individual components of stress matrix, gives plastic strains. The plastic strain is expressed as:

$$\delta \varepsilon_{ij}^p = \partial \chi \cdot \frac{\partial g}{\partial \sigma_{ij}}. \quad (6.16)$$

A flow rule is introduced to relate the plastic strain direction to the yield surface. The plastic potential equation above is a form of non-associated flow rule. If the plastic potential

calculation uses the yield surface function f instead of g , the flow rule will be called associated flow rule. The equation 6.16 can be rewritten as:

$$\delta\varepsilon_{ij}^p = \partial\chi \cdot \frac{\partial f}{\partial \sigma_{ij}} \quad (6.17)$$

The scalar function is the yield surface function if the plastic strain increment vector is normal to the yield surface. The scalar function is any other function that describes the direction of plastic strain increment vector if they are not perpendicular to yield surface.

The ratio of the shear stress q to mean stress p is denoted as η . Using the plastic potential function and the associated flow rule the following matrix describes the plastic strain calculation. (Wood, 1990). Total plastic strains are:

$$\begin{bmatrix} \delta\varepsilon_v^p \\ \delta\varepsilon_s^p \end{bmatrix} = \frac{(\lambda-\kappa)(1-\phi)}{p'(M^2+\eta^2)} \begin{bmatrix} M^2 - \eta^2 & 2\eta \\ 2\eta & \frac{4\eta^2}{M^2-\eta^2} \end{bmatrix} \begin{bmatrix} \partial p' \\ \partial q \end{bmatrix} \quad (6.18)$$

7. APPENDIX II – MCC MODEL FITS

In this section we will provide the MCC model fits for Test 2 – PSP 214.

Table 7-1 shows the MCC Model parameter fits for PSP 214 on initial conditions, 1st injection, 1st depletion and last depletion ramps.

MCC Model Parameters						
Stress path	Lambda	Kappa	M	Pre-consolidation Stress (psi)	Porosity	Poisson's Ratio
Triaxial	0.017	0.016	0.77	4200	0.27	0.21
1 st Injection	0.017	0.010	1.0	4400	0.25	0.18
1 st Depletion	0.017	0.010	1.0	4500	0.26	0.18
Last Depletion	0.027	0.019	1.0	5200	0.23	0.18

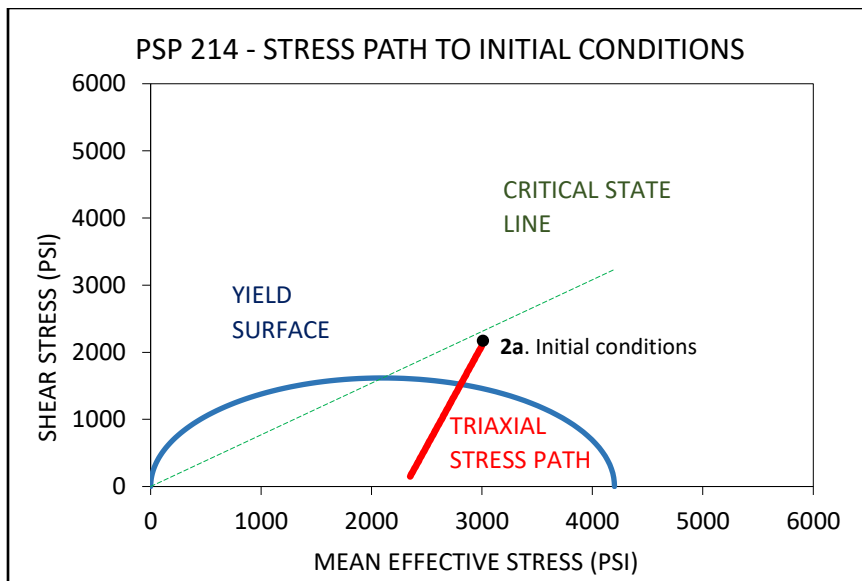


Figure 7-1 Shows the calibrated MCC model for triaxial stress path ramp of PSP 214. The yield surface is shown in blue; the critical state line is shown in green and the triaxial stress path is shown in red.

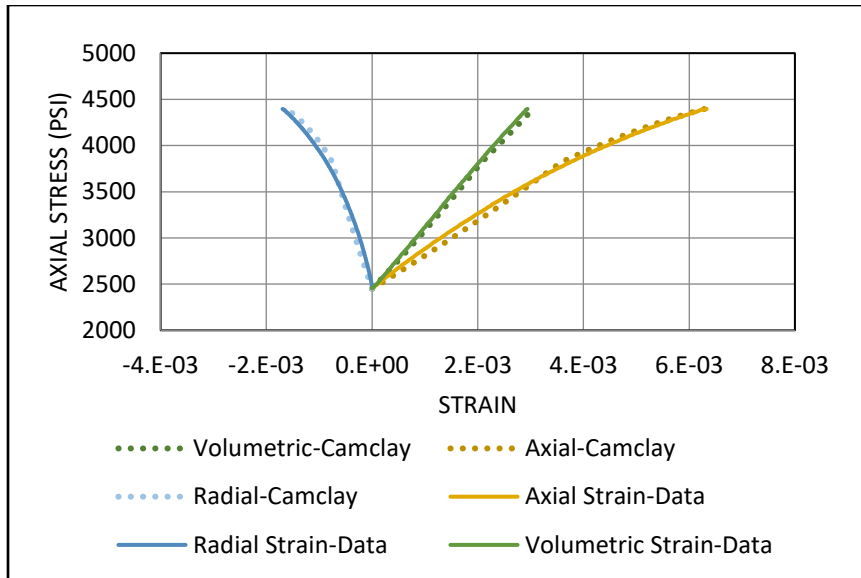
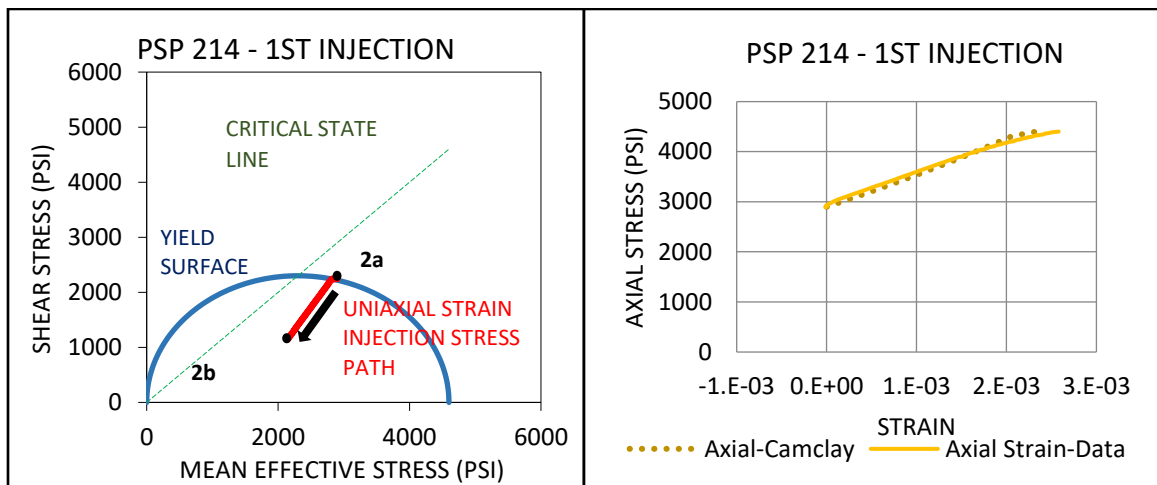
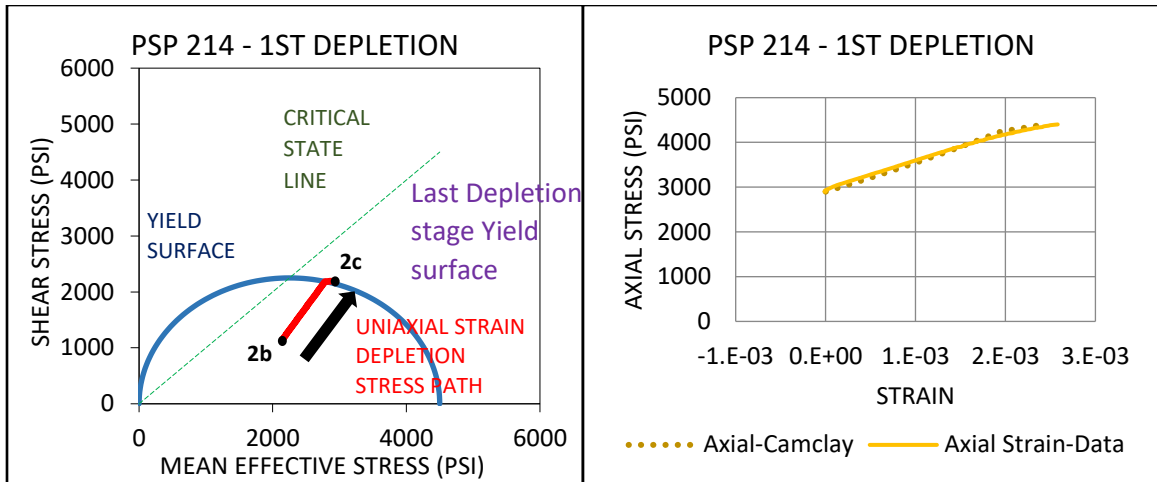


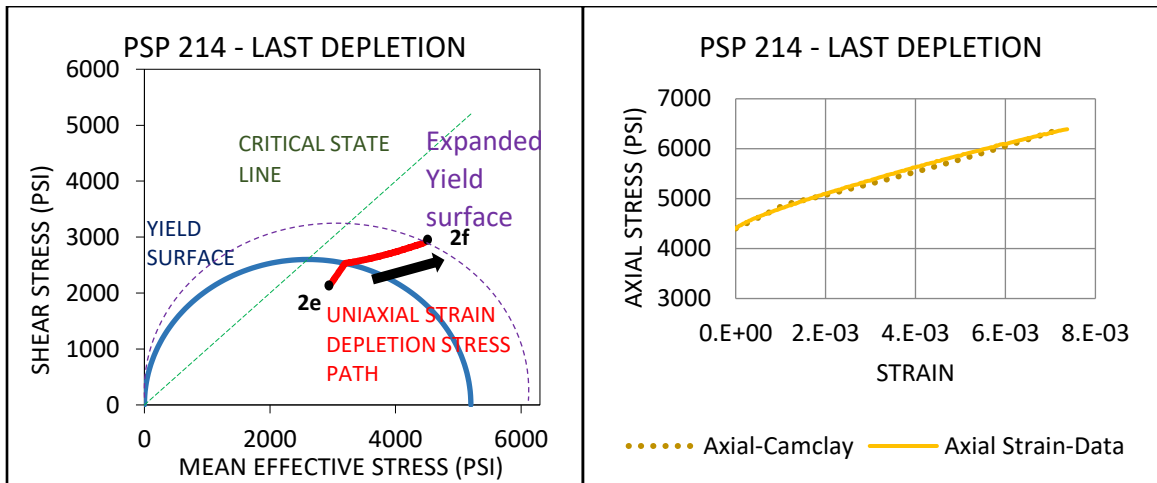
Figure 7-2 Shows the simulated strain data and experimental strain data plotted together. There is a good match between the two data sets indicating a good model fit.



(A)



(B)



(C)

Figure 7-3 Shows the MCC model fits for the 1st injection (A), 1st depletion (B) and last depletion stress path for PSP 214. A simulated yield surface with its critical state line and the stress path taken by the sample and with experimental axial strain data recorded from the lab measurements are plotted.